学位論文 （要約）

Carrier dynamics at surfaces of WSe$_2$
studied by time-resolved photoemission
spectroscopy

（時間分解光電子分光による WSe$_2$ 表面
のキャリアダイナミクス研究）

平成 29 年 7 月博士（理学）申請

東京大学大学院理学系研究科

物理学専攻

劉 若亞

Department of Physics

The University of Tokyo

Carrier dynamics at surfaces of WSe$_2$ studied by time-resolved photoemission spectroscopy

Thesis

Ro-Ya Liu

July 2017

Abstract

Two-dimensional transition metal dichalcogenides (TMDC) have nowadays attracted attention in research on valley-, spin-, and opto-electronics. Performance of these novel technologies depends on carrier dynamics in the materials, however, understanding of the non-equilibrium electronic structure has remained uncertain. Photoemission spectroscopy has been the most powerful experimental technique to probe electronic states in materials directly and recently developed time-resolved measurements allow us to trace them in real time.

In the present work, ultrafast carrier dynamics at surfaces of WSe_2 crystals, and monolayer WSe_2 crystals are investigated by time-resolved photoemission spectroscopy. Using two types of light sources, high-harmonic generation laser and highly-brilliant synchrotron radiation, the time-evolution was chronologically traced from femotosecond to nanosecond after the pumping optical trigger. Dynamical data are systematically discussed in terms of the electronic structure.

In the femtosecond-time scale, various types of non-equilibrium states were observed in the semiconducting WSe_2 crystals, depending on the photon energy of the pumping optical pulse. The light-induced electronic state is generated as Floquet replica bands when pumping photon energy is lower than the bulk direct band gap. When the pumping photon energy is larger than the bulk band gap, photo-excitation to the bulk conduction band is valley-dependent, showing the polarization dependence. Occupations of the conduction band at the K point of the hexagonal Brillouin zone become maximum or minimum by the right-handed or left-handed circular polarized light, respectively, and the optical response reverses at the K' point. At the monolayer WSe_2 surface, a significant band shift is observed in the fs range after intense excitation by above-band-gap pump pulses. This band shift can be attributed to the band gap renormalization due to the population inversion and strong electronic interaction. The band shift decay within a ps due to the carrier recombination.

In the following picosecond-time scale, photoemission intensity of the bulk valence band shows an oscillation that is found to have a frequency of 6.7 THz by the Fourier-transformation analysis and to be related to a coherent phonon. Since it corresponds to twice the frequency of 3.2 THz of the maximum single acoustic phonon density in WSe_2, the observation indicates formation of the two-phonon squeezed state.

In the nanosecond-time scale, relaxation of the surface photovoltage (SPV) effect, induced simultaneously by the photo-excitation, is apparently observed. The dynamical phenomena are associated with carrier transfer between the surface and the bulk region. By formation of the heterojunction on a WSe_2 surface with the donor (K)- or acceptor(C_{60})-adlayer, the generation and the relaxation of SPV are modified, showing possible opto-electronic regulation.

The present work has revealed temporal variations of the non-equilibrium electronic structure of WSe_2 after the optical pulse by time-resolved photoemission spectroscopy. The various dynamical phenomena happen on different time scales, which are consistently described by the light-matter interaction and carrier dynamics in the material. The concepts, developed in this work, are expected to be a landmark in developing photo-science and opto-electronic devices.

Acknowledgements

It is my honor to show my sincere gratitude to the people who contributed in different ways to this study. Foremost I appreciate all the participants of this research for their efforts to help me with this dissertation, I sincerely acknowledge their contributions.

First of all, I would like to express my deepest gratitude to my supervisor Professor Iwao Matsuda (Institute for Solid State Physics, The University of Tokyo) for his supervision. I would like to thank him for his patient guidance, valuable advice, constructive comments and continuous encouragement throughout my doctoral course and also for his critical reading of this manuscript.

My sincere thanks also go to Professor Tai-Chang Chiang (Department of Physics, University of Illinois Urbana-Champaign), who always supports me behind and spurs me on when I was inefficient and frustrated. I am really thankful for his endless patience and encouragement. It is my honor to work with such an erudite scholar. I also want to show my sincere gratitude to Dr. Kenich Ozawa (Department of Chemistry, Tokyo Institute of Technology), who taught me the basic knowledge of XPS and TRXPS from zero. Dr. Ozawa gave me many supports and knowledge in the first and second year of my phD, which supported me pass through a hard time. I have learnt a lot from his careful and strict research style.

In regards to the TRARPES experiments, I thank Porfessor Shik Shin, Professor Kozo Okazaki and the related members in their labs: Dr. Yukiaki Ishida, Dr. Takeshi Suzuki, Mr. Yu Ogawa, Mr. Masasu Okada, and Ms. Mari Watanabe. The yonngouki team taught me many basic knowledge of TRARPES and helped me a lot during the experiment period. I really thank their generous supports, patience, and kindly helps even in holidays.

In my later work of TRARPES experiments, I am particularly indebted to Dr. Emma Springate, Dr. Cephise Cacho, all the staff in Artemis beamline, and the secretaries in the User Office of Central Laser Facility, Rutherford Appeleton Laboratory, UK. I especially thank Dr. Cephise Cacho's help and endless patience for a plenty of Skype meetings. The experiment system, the working style, and many trivial but brilliant ideas in the TRARPES experiment really widen my perspective on pump and probe PES technology, and lab safety issues. Special thanks to Dr. Timur Kim(I05 beamline, Diamond Light Source), Dr. Richard Champman, Dr. Adam Wyatt, Mr. Phil Rice, and Mr. Alfred Jonesfor many technical supports during the experiment period. I also

Contents

Abbreviations

1D, 2D, 3D	**One- Two- Three-**dimensional
ARPES	**A**ngle-**r**esolved **p**hotoemission **s**pectroscopy
ARTOF	**A**ngle-**r**esolved **t**ime-**of-f**light spectroscopy
BLG	**B**i-**l**ayer **g**raphene
BZ	**B**rillouin **z**one
CBM	**C**ond**c**tion **b**and **m**inimum
CVT	**C**hemical **v**aper **T**ransport
DC	**D**irac **c**one
EDC	**E**nergy **d**istribution **c**urve
EUV	**E**treme **u**ltraviolet
FWHM	**F**ull **w**idth at **h**alf-**m**aximum
HHG	**H**igh-**h**armonic **g**eneration
IGS	**I**nner-**g**ap **s**tate
LAPE	**L**aser-**a**ssited **p**hotoemission **e**ffect
LCP	**L**eft-**h**anded **c**ircular **p**olarization
LEED	**L**ow-**e**nergy **e**lectron **d**iffraction
ML	**M**onolayer
OAS	**O**ptical **a**dsorption **s**pectroscopy
PES	**P**hotoemission **s**pectroscopy
QWS	**Q**uantum **w**ell **s**tate
RCP	**R**ight-**h**anded **c**ircular **p**olarization
SBZ	**S**urface **b**rillouin **z**one
SCL	**S**pace **c**harge **l**ayer
SOC	**S**pin-**o**rbit **c**oupling

SPV	**S**urface **p**hoto**v**oltage
TMDC	**T**ransition **m**etal **di**chalcogenide
TRARPES	**T**ime-**r**esolved and **a**ngle-**r**esolved **p**hoto**e**mission **spectroscopy**
TROAS	**T**ime-**r**esovled **o**ptical **a**dsorption **s**pectroscopy
TRXPS	**T**ime-**r**esolved **X**-ray **P**hotoemission **Spectroscopy**
UHV	**U**ltra-**h**igh **v**acuum
VBM	**V**alence **b**and **m**aximum
XPS	**X**-ray **p**hotoelectron **s**pectroscopy

Physical Constants

Speed of Light in vacuum	c	$=$	$2.99792458 \times 10^{8} \ \mathrm{m \cdot s^{-1}}$
Planck's constant	h	$=$	$6.62606957 \times 10^{-34} \ \mathrm{J \cdot s}$
reduced Planck's constant	$\hbar = \frac{h}{2\pi}$	$=$	$1.054571726 \times 10^{-34} \ \mathrm{J \cdot s}$
Boltzmann constant	k_{B}	$=$	$1.3806488 \times 10^{-23} \ \mathrm{J \cdot K^{-1}}$
electron mass	m_{e}	$=$	$9.10938188 \times 10^{-31} \ \mathrm{kg}$
elementary charge	e	$=$	$1.602176462 \times 10^{-19} \ \mathrm{C}$
Bohr radius	a_{0}	$=$	$5.291772083 \times 10^{-11} \ \mathrm{m}$
Hartree energy	E_{h}	$=$	$4.35974381 \times 10^{-18} \ \mathrm{J}$
Vacuum permeability	$\mu_{0} = 4\pi \times 10^{-7}$	$=$	$1.2566370614 \times 10^{-6} \ \mathrm{N \cdot A^{-2}}$
Vacuum permittivity	$\epsilon_{0} = \frac{1}{\mu_{0}c^{2}}$	$=$	$8.854187817620 \times 10^{-12} \ \mathrm{F \cdot m^{-1}}$

The International System of Units (Le Système International d'Unités: SI units) is mainly used in this thesis. Some of the useful conversion formulae are listed in this page.

1 eV = $1.60217657 \times 10^{-19}$ J

$h\nu$ [eV] $= \frac{hc}{e}\frac{1}{\lambda[nm]} \simeq \frac{1240}{\lambda[nm]}$

1 Å $= 10^{-10}$ m

0.1 Å^{-1} = 1 nm^{-1}

$k_{\parallel}$[nm^{-1}] $= 5.12\sqrt{E_k[\text{eV}]}\sin\theta$

$k_{\parallel}$[Å^{-1}] $= 0.512\sqrt{E_k[\text{eV}]}\sin\theta$

1 in (inch) = 25.4 mm

1 mi (mile) = 1609.344 m

1 Pa = 1 N/m^2 = 1×10^{-2} mbar = 7.5×10^{-3} Torr

1 atm = 101325 Pa = 1013.25 mbar = 760 Torr

1 T = 10^4 G (Gauss)

Earth's magnetic field = $24- 66 \times 10^{-6}$ T = 0.24−0.66 G

0 K (Kelvin) = -273.15 °C (Celsius) = 459.67 °F (Fahrenheit)

x K = $x - 273.15$ °C = $\frac{9}{5}(x - 273.15) + 32$ °F

273.15 K = 0 °C = 32.0 °F

Symbols

$\boldsymbol{A}$	Vector potential of the electromagnetic field
E	Energy
E_{F}	Fermi energy
E_k	Kinetic energy of a photoelectron in the vacuum
$E_{k,\mathrm{F}}$	Kinetic energy of a photoelectron emitted from the Fermi edge in the vacuum at an electron analyzer
E_{pass}	Pass energy
f_{FD}	Fermi-Dirac distribution function
$h\nu$	Photon energy
k	Electron wavenumber
k_{F}	Fermi wavenumber
V_0	Inner potential
V_{s}	Surface potential
V_{SPV}	Surface photovoltage shift
N_{A}	Bulk accepter density
n_{2D}	Density of 2D electrons
N_{D}	Bulk donner density
N_{ss}	Surface carrier density
N_{V}	Valence band density of states
L_{D}	Depth of the depletion layer
T	Temperature
w_{if}	Transition probability from initial to final states

η	Ideality factor
μ	Carrier mobility
Σ	Self-energy of an electron
σ_{th}	Thermal cross section of capturing an electron
τ_{rise}	Rising time of excited carriers
Φ	Work function of a solid

Chapter 1

Introduction

1.1 History

Transition-metal dichalcogenides (TMDC) is a general class for a herd of chemical compounds (See Figure 1.1). One group in the class, two-dimensional layered compound semiconductor is MoS_2, $MoSe_2$, WSe_2, and WS_2. Molybdenum disulfide, a nature mineral called as molybdenite, is a usual lubricant in industry. The band structure and optical properties of this family had been figured out decades ago. R. A. Bromley *et al* in 1972 [1], studied the electronic structure of MX_2 (M:Mo, W; X:S, Se) by tight binding calculation. Frindt *et al.* [2] measured the optical absorption spectra of MX_2. TMDC semiconductors have indirect band gaps within visible range, which make them as the potential candidates for solar cells, such as photoelectrochemical cell (PEC). Also, a large surface photovoltage (SPV) has been observed on TMDCs surfaces while illuminating visible light. The metal-semiconductor interface has been studied a lot by photoemission spectroscopy in 1990s [3–5]. J. Buck *et al.* [6] carefully calculated the surface band bending amount and SPV effect via transport equations on Rb/WSe_2. The maximum band bending of WSe_2 is about 1 eV, which is almost an order of magnitude larger than other semiconductors.

With the progress of ultra high vacuum technology and of optical microscopy, thin atomic layer of TMDCs can be produced and measured under ultra-high vacuum (UHV) condition. People move attention to the surface of semiconductor and two-dimensional materials. In 2007, Xiao *et al.* [9, 10], predicted a new degree of freedom for electronics in monolayer (ML) TMDC – valley. In haxagonal lattice, upward parabolic conduction band (CB) and downward valence band (VB) behave like massive dirac cones locate

FIGURE 1.1: TMDC family (a) Categories of graphene family, TMDC family, and 2D oxides family [7]. (b) Transition metal elements and chalcogen elements in the periodic table [8].

at the K points. These cones located at the 6 apex of hexagonal Brillouin zone can be separated into two sets, which is induced by the inversion symmetry breaking in ML TMDCs. The Berry curvatures and orbital magnetic moments possess opposite sign at K and K' valleys. This prediction caused a tremendous attention in condensed matter physics. TMDC reached its renaissance since 2008. Since the Van der Waals interaction along the c axis is very weak, each trilayer preserve its own spin textures and nondegenerate valleys. Although the spin textures of each trilayers add up to zero in bulk, the spin-polarized band on bulk WSe_2 is observed by spin-resolved and angle-resolved photoemission spectroscopy (SARPES) [11]. In bulk WSe_2, circular dichroism at different K valleys pumped by circular polarized light has been found by time-resolved and angle-resolved phoemission spectroscopy (TRARPES) [12] because TRARPES is very surface sensitive and most signals contributed from the first trilayer. The above studies imply the surface of bulk inherit some of the electronic and optical properties from ML TMDC, and the application of bulk sample is also promising.

For the non-equilibrium electronic response, the conduction band carrier life time of bulk WSe_2 is quite long and last more than 1 ps. Further more, the optical excitation efficiency is very high by left(right)-handed circular polarized pump at K(K′) valleys [12]. In ML WSe_2, the excitation signals attenuate fast due to the substrate effect such as the screening effect on gold [13], or the scattering with defect state, inner gap states from the substrate such as bilayer graphene/SiC(0001) [14].

For the below band gap pumping, J. Sie *et al.* [15] observed the optical Stark shift on ML WS_2 by circular polarized light. The spontaneous shift of the absorption peak was attributed to the formation of hybridization of Floquet states (photon dressed states). Martin Claassen *et al.* [16] mentioned the existence of chiral edge state and photon-induced band inversion at different K valleys by tight-binding model. The light-matter interaction actually changes the topology of TMDC ML, which generates an edge state at the surface.

1.2   Thesis Motivation

The main purpose of this thesis is to clarify carrier dynamics and electronic structures at TMDC surfaces related to their band bending structures, valleytronics, and heterojunctions. The time-resolved X-ray photoemission spectroscopy (TRXPS), and time-resolved and angle-resolved photoemission spectroscopy (TRARPES) are the main tools to study the carrier dynamics of TMDC surfaces. The following problems were explored:

(1) Femto- to pico-second phenomena of bulk WSe_2 under below and above band gap pumping conditions: The first objective is to study the femto- to pico-second phenomena of bulk WSe_2 under below- and above-band gap pumping conditions. By below (above) band gap pumping, the two-dimensional valence and conduction bands may interact with circular polarized light and generate Floquet-Bloch (photon dressed) states. In ps range, coherent lattice vibration has been found by time-resolved optical absorption spectroscopy. A direct observation of electronic structure under non-equilibrium condition is appealing.

(2) Circular polarization dependence of carrier dynamics in bulk WSe_2 and ML WSe_2: The second objective is to study the polarization dependence of the ultrafast response on TMDCs under red-detuned or blue-detuned pumping condition. The polarization dependence is a key issue in valleytronics of TMDCs. Though the study of TMDC

monolayers by the circular polarized time-resolved optical spectroscopy has been studied, the straightforward evidence of the electronic structure is still lacking. The correspondence of TRARPES and time-resolved optical absorption spectroscopy (TROAS) is very essential work for confirming the theory of valleytronics.

(3) Surface photovoltage (SPV) on modified WSe_2 surfaces: The third objective is to study the SPV effect on clean WSe_2 and then compare it with modified surfaces. To apply TMDCs to solar cell device, further surface treatment to enhance the surface photovoltage and suppress the surface recombination rate of carriers are important. In this study, two common dopants, K and C_{60}, were used to increase the SPV effect on WSe_2.

1.3   Thesis Structure

This thesis is organized as follows: Chapter 2 introduces the fundamental electronic structures of bulk TMDCs, ML TMDCs, and basic knowledge of carrier recombination in SPV relaxation. Chapter 3 describes principles of photoemission spectroscopy, experimental systems, important equations, and fitting functions. The experimental set-up at three time-resolved photoemission stations are introduced: (1) TRXPS station at beamline 07LSU, SPring-8 (2) TRARPES station at ISSP, University of Tokyo and (3) TRARPES station at Artemis, Central Laser Facility, Rutherford Appleton Laboratory, UK. Chapter 4 reports the experimental results of Floquet-Bloch state of bulk WSe_2 under below band gap pumping. Chapter 5 describes experimental realization of the carrier dynamics at ML WSe_2 surface and circular polarization dependence of bulk WSe_2 under above band gap pumping. Chapter 6 presents the results of SPV relaxation on three surfaces: WSe_2, C_{60}/WSe_2, and K/WSe_2. Chapter 7 summarizes all the experimental results in this thesis.

Chapter 2

Backgrounds

2.1 Electronic structure of WSe$_2$

TMDC semiconductors are generally composed of MX$_2$, where M is a transition metal (Mo, W) and X is a chalcogen atom (S, Se). MX$_2$ tends to form two-dimensional layer compounds with different stacking order such as 2H, 3R, and 1T phases. The most frequent synthesis method is chemical vapor transport (CVT) technique [17]. Some halogons were used as the transport agents in the synthesis and last in the crystal permanently, thus the crystal is p-doped by the residue of iodine, or n-doped by the residue of bromine [18]. In each sandwich layer, the transition metal M is the centered atom surrounded by chalcogen atoms from top and bottom layer. Each M atom is bonded to 6 chalcogen atoms in the trigonal prismatic coordination. Each X atom is bonded to three M atoms in a pyramidal geometry. All the chemical bonds are saturated in the sandwich layer in parallel direction, such that the coupling along vertical axis is simply governed by Van der Waals force. The atomic structure of the 2H phase is drawn in Fig. 2.1(a). This crystal shows anisotropy along the parallel or vertical directoin, for example, dielectric constant, carrier mobilities. In 2H phase, two sandwich layers are piled up with a 60° rotation between each other. Figure 2.2 shows the ARPES map and calculated band structure by DFT. The conduction band minimum locates at T, which is around the middle of $\overline{\Gamma K}$, and the valence band minimum locates at Γ. All the TMDC semiconductors have indirect bandgaps. The direct band gap locates at K point (labeled as E'_{gap} in Fig. 2.2(b)). Two valence downward parabolic bands at K point are generated by Dresshalues SOC splitting [19] (labeled as Δ_{SO} in Fig. 2.2(b)).
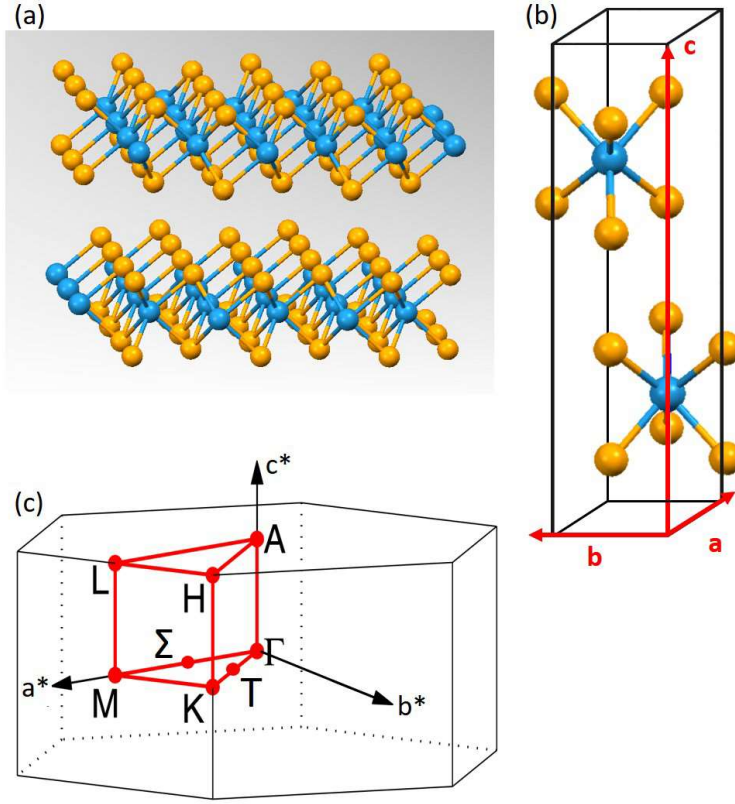
FIGURE 2.1: (a) Crystal structure of 2H-WSe$_2$. (b) First Brillouin zone. (c) Unit cell of 2H-WSe$_2$.

In each sandwich layer, valence bands around K possess opposite spin (out of plane) from each other. In previous work, the calculated spin-polarized band structure at valence bands at K are almost 100% spin polarized at the top layer [11]. Although the total spin polarization should be zero in bulk sample, each layer still conserve its spin polarization and magnetic moment [20]. J. M. Riley *et al.* [11], observed the spin-polarized band in bulk WSe$_2$. This result was explained by the surface sensitivity of ARPES and the decoupling of K and K$'$ in the top layer.

The electronic properties of bulk TMDCs are quite two-dimensinal like, the electronic properties along c axis is totally different from the one in in-plane. The mobility is an impoartant parameter for the electronic device. It has been reported that the anisotropy of electron mobility($\mu_{e,\parallel}/\mu_{e,\perp}$) varies from 40 to $\sim 10^3$ [21]. The dielectric constant is has been predicted to be very different between in plane and out of plane. However, the length of bulk WSe$_2$ sample is hard to exceed 100 μm, such that the precise measurement is difficult. Table 2.1 notes the basic properties of bulk WSe$_2$.
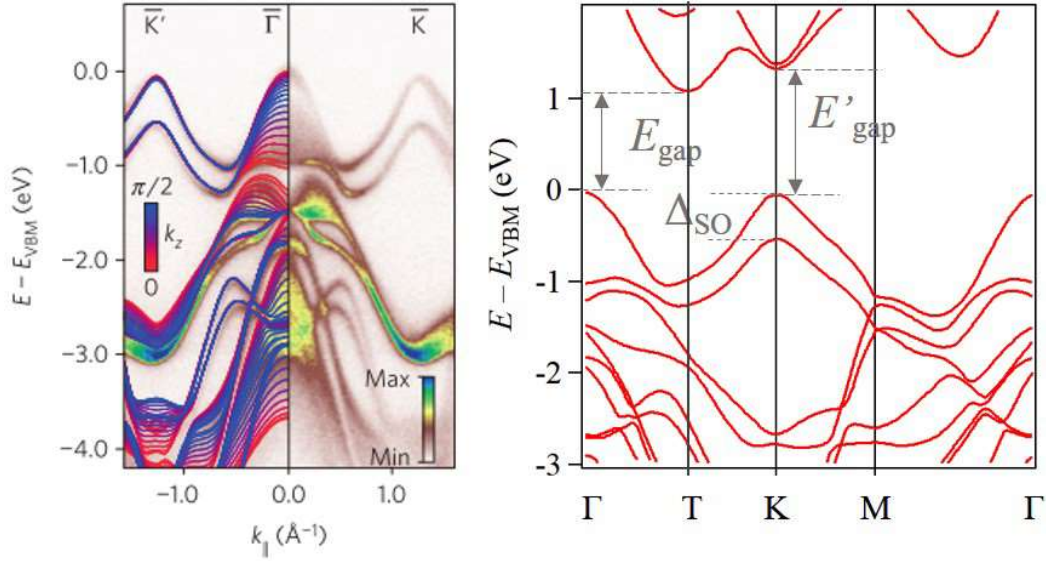
FIGURE 2.2: (a) ARPES map of WSe$_2$ along $\overline{\Gamma}$ to $\overline{K}$ (b) Band structure by DFT calculation [11].

2.2 Electronic structure of monolayer transition metal dichalcogenides semiconductors

In monolayer TMDCs, the band gap is changed into a direct band gap at K. Figure 2.3 shows the crystal structure and the Brillouin zone. Due to the reduction of half unit cell, there is no global inversion symmetry, K and K′ were decoupled and posses opposite spin-polarized VBs. Figure 2.4 shows the band structure of different ML TMDCs by DFT calculation and tight binding model. The VBM and CBM locate at K, which implies that the VBs and CBs near K will play a key role for many optical properties near resonant scale. ML TMDCs can be treated as the semiconductor version of graphene.

At K valley, the two valence bands are generally composed of $d_{xy} + d_{x^2-y^2}$ from M element and p_x, p_y, p_z from X element. In the conduction band, the orbital component at $\overline{K}$ is mainly contributed from d_{z^2}. Simplified models such as three-band tight-binding model [24, 25], $k \cdot p$ approach [26] can explain the underlining physics at K valleys very well. Xiao *et al.*[26], predicted coupled spin and valley physics generated by the inversion symmetry breaking and strong spin-orbit coupling. A new field "valleytronics" has been named and developed rapidly. In the three-band tight-binding model, the basis

TABLE 2.1: List of many parameters for bulk WSe$_2$ band structure, lattice parameters.

Real Space			
	a $(= b)$	3.29 Å	[1]
	c	12.96 Å	[1]
Reciprocal Space			
	$\overline{\Gamma A}$	0.24 Å^{-1}	[1]
	$\overline{\Gamma M}$	1.10 Å^{-1}	[1]
	$\overline{\Gamma K}$	1.27 Å^{-1}	[1]
Parameters for electronic structure			
Band gap	E_{gap}	1.3 eV	[22]
Direct Band gap	E'_{gap}	1.63 eV	[12]
SOC splitting	Δ_{SO}	530 meV at K	[1, 11]
Bulk hole density	p_{b}	10^{16} cm^{-3}	
Hole mobility	$\mu_{\mathrm{h},\parallel}$	236	[23]
Electron mobility	$\mu_{\mathrm{e},\parallel}$	105	[23]
Relative dielectric constnat	ϵ_{s}	24	[23]
Optical absorption coefficient	α	1.5×10^5 (730 nm)	[2]
		5.7×10^4 (800 nm)	

functions are defined as:

$$|\phi_1^1\rangle = d_{z^2}, |\phi_1^2\rangle = d_{xy}, |\phi_2^2\rangle = d_{x^2-y^2}, \tag{2.1}$$

The three-band tight-binding Hamiltonian can be written as:

$$H^{NN}(k) = \begin{bmatrix} V_0 & V_1 & V_2 \\ V_1^* & V_{11} & V_{12} \\ V_2^* & V_{12}^* & V_{22} \end{bmatrix} \tag{2.2}$$

Each matrix element in this Hamiltonian is listed in Table 2.2. Figure 2.4 shows the band structure obtained from this model and DFT calculation. To get SOC splitting, the SOC term is included via the equation below:

$$H_{\mathrm{SOC}}(k) = I_2 \otimes H_0(k) + H'$$
$$= \begin{bmatrix} H_0(k) + \frac{\lambda}{2} L_z & 0 \\ 0 & H_0(k) - \frac{\lambda}{2} L_z \end{bmatrix}$$

Figure 2.5 shows the band structure of free standing WSe$_2$ by DFT calculation and
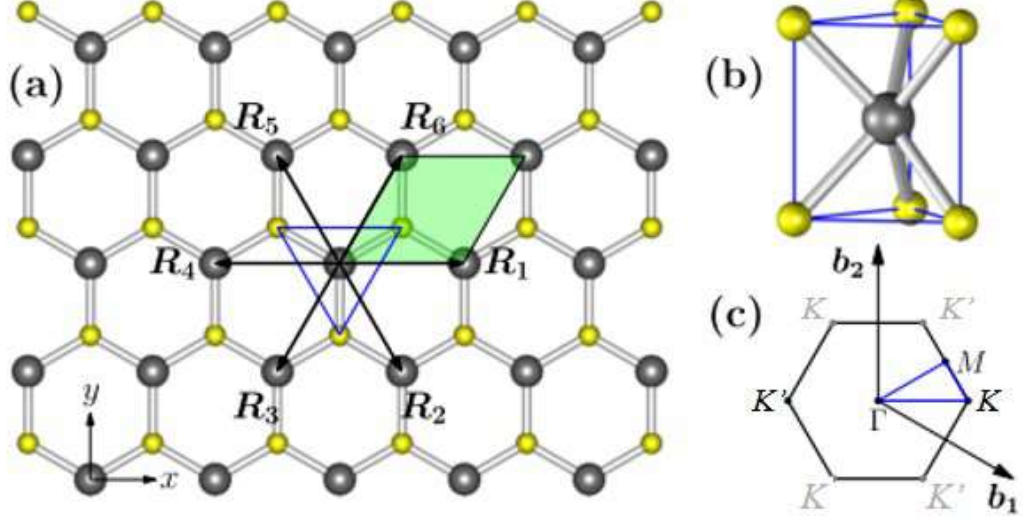
FIGURE 2.3: (a) Atomic structure viewed from (001) direction. Gray atoms
and yellow atoms are W and Se, respectively. $\boldsymbol{R_1}$-$\boldsymbol{R_6}$ are distance from nearest
neighbors of Se. (b) 2D unit cell of ML TMDC. (c) First Brillouin zone [24].

tight-binding calculation. Considering the on-site spin-orbit interaction, the large spin
splitting of valence bands at K can be described well. Figure 2.5 (a) and (b) show
the comparison between the DFT and tight-binding calculation. The three-band third
nearest neighbor tight-binding model can give a good evaluation of two VBs and lowest
CB.

Interband optical transition and circular dichroism

Conventionally, light couples to the electronic bands through a gauge filed A, which
replace $\mathbf{P} \to \mathbf{P} + e\mathbf{A}$. The interband optical transition rate approximated by Fermi's
golden rule can be written as:

$$I(\omega) \sim \omega^{-2} \sum_{\mathbf{k},c,v} |\langle \psi_{c,\mathbf{k}} | \mathbf{A} \cdot \mathbf{P} | \psi_{v,\mathbf{k}} \rangle|^2 \, \delta(\epsilon_c(\mathbf{k}) - \epsilon_v(\mathbf{k}) - \hbar\omega). \tag{2.3}$$

Here, $\psi_{v,\mathbf{k}}(\psi_{c,\mathbf{k}})$ is the wave functions of valence (conduction) band at the $\mathbf{k}$ point.
$\epsilon_c(\mathbf{k})$ and $\epsilon_v(\mathbf{k})$ are the eigenenergies of conduction band and valence band at $\mathbf{k}$.

The degree of circular dichroism is defined as:

$$\eta(\mathbf{k}) = \frac{|\langle \psi_{c,\mathbf{k}} | \mathbf{A}_+ \cdot \mathbf{P} | \psi_{v,\mathbf{k}} \rangle|^2 - |\langle \psi_{c,\mathbf{k}} | \mathbf{A}_- \cdot \mathbf{P} | \psi_{v,\mathbf{k}} \rangle|^2}{|\langle \psi_{c,\mathbf{k}} | \mathbf{A}_+ \cdot \mathbf{P} | \psi_{v,\mathbf{k}} \rangle|^2 + |\langle \psi_{c,\mathbf{k}} | \mathbf{A}_- \cdot \mathbf{P} | \psi_{v,\mathbf{k}} \rangle|^2}, \tag{2.4}$$
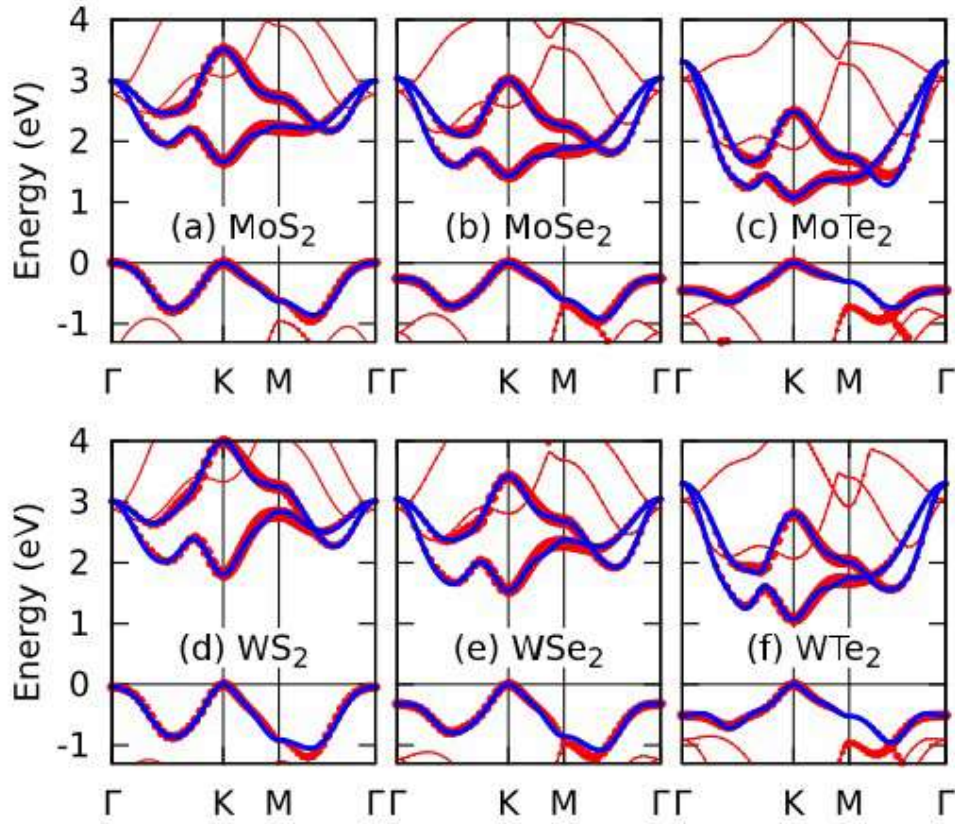
FIGURE 2.4: Band structure of (a) MoS_2 (b) $MoSe_2$ (c) $MoTe_2$ (d) WS_2 (e) WSe_2 (f) WTe_2 by DFT-GGA calculations (red curves) and three band third-nearest-neighbor (TNN-TB) (blue curves). The size of dots represent the contribution from d_{z^2}, d_{xy}, and $d_{x^2-y^2}$ orbitals [24].
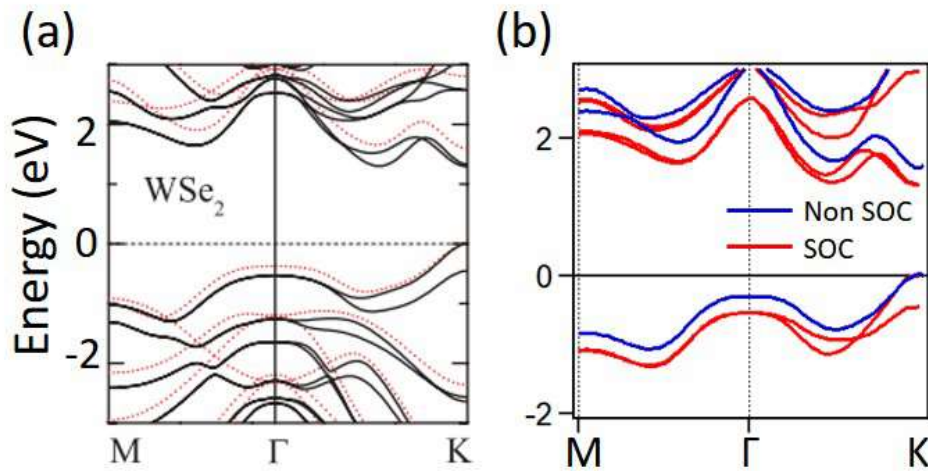
FIGURE 2.5: Band structure of (a) WSe_2 by GGA (red dashed lines) and GGA+SOC (black lines) calculation [27]. (b) WSe_2 by TNN-TB calculation with or without SOC.

$\textsc{Table}$ 2.2: Some parameters for three band third-nearest-neighbor tight-binding (TNN-TB) hamiltonian [24].

V_0	$t_1 + 2t_0(2\cos\alpha\cos\beta + \cos 2\alpha) + 2r_0(2\cos 3\alpha\cos\beta + \cos 2\beta)$
	$+2u_0(2\cos 2\alpha\cos 2\beta + \cos 4\alpha)$
$\mathrm{Re}[V_1]$	$-2\sqrt{3}t_2\sin\alpha\sin\beta + 2(r_1 + r_2)\sin 3\alpha\sin\beta$
	$-2\sqrt{3}u_2\sin 2\alpha\sin 2\beta$
$\mathrm{Im}[V_1]$	$2t_1\sin\alpha(2\cos\alpha + \cos\beta) + 2(r_1 - r_2)\sin 3\alpha\cos\beta$
	$+2u_1\sin 2\alpha(2\cos 2\alpha + \cos 2\beta)$
$\mathrm{Re}[V_2]$	$+2t_2(\cos 2\alpha - \cos\alpha\cos\beta) - \frac{2}{\sqrt{3}}(r_1 + r_2)(\cos 3\alpha\cos\beta - \cos 2\beta)$
	$+2u_2(\cos 4\alpha - \cos 2\alpha\cos 2\beta)$
$\mathrm{Im}[V_2]$	$2\sqrt{3}t_1\cos\alpha\sin\beta + \frac{2}{\sqrt{3}}\sin\beta(r_1 - r_2)(\cos 3\alpha + 2\cos\beta)$
	$+2\sqrt{3}u_1\cos 2\alpha\sin 2\beta$
V_{11}	$\epsilon_2 + (t_{11} + 3t_{22})cos\alpha cos\beta + 2t_{11}cos2\alpha + 4r_{11}cos3\alpha cos\beta$
	$+2(r_{11} + \sqrt{3}r_{12})cos2\beta + (u_{11} + 3u_{22})cos2\alpha cos2\beta + 2u_{11}cos4\alpha$
$\mathrm{Re}[V_{12}]$	$\sqrt{3}(t_{22} - t_{11})\sin\alpha\sin\beta + 4r_{12}\sin 3\alpha\sin\beta + \sqrt{3}(u_{22} - u_{11})\sin 2\alpha\sin 2\beta$
$\mathrm{Im}[V_{12}]$	$4t_{12}\sin\alpha(\cos\alpha - \cos\beta) + 4u_{12}\sin 2\alpha(\cos 2\alpha - \cos 2\beta)$
V_{22}	$\epsilon_2 + (3t_{11} + t_{22})\cos\alpha\cos\beta + 2t_{22}\cos 2\alpha + 2r_{11}(2\cos 3\alpha\cos\beta + \cos 2\beta)$
	$+2\sqrt{3}r_{12}(4\cos 3\alpha\cos\beta - \cos 2\beta) + (3u_{11} + u_{22})\cos 2\alpha\cos 2\beta + 2u_{22}\cos 4\alpha$
(α, β)	$\left(\frac{1}{2}k_x a, \frac{\sqrt{3}}{2}k_y a\right)$
(a, z_{X-X})	3.325, 3.363
(ϵ_1, ϵ_2)	0.943, 2.179

ϵ_1	ϵ_2	t_0	t_1	t_2	t_{11}	t_{12}	t_{22}	r_0	r_1
r_2	r_{11}	r_{12}	u_0	u_1	u_2	u_{11}	u_{12}	u_{22}	
0.728	1.655	-0.146	-0.124	0.507	0.117	0.127	0.015	0.036	-0.234
0.107	0.044	0.075	-0.061	0.032	0.007	0.329	-0.202	-0.164	

where $\mathbf{A}_+(\mathbf{A}_-)$ is the vector potential for right(left) handed circular polarized light. The photon energy was chosen to be the difference between the two bands at each $\mathbf{k}$ point. At K or K', $\eta(\mathbf{k})$ is $+1$ or -1 due to the optical chiral selection rule. $\eta(\mathbf{k})$ is draw in k domain in Fig. 2.6(b), a large region near K and K' was governed by the selection rule.

2.3   Floquet-Bloch State and Volkov State

Due to the rapid development of high power pulsed laser and ultrafast time duration in femtosecond regime, many exotic non-equilibrium phenomena that occurred in the condensed matter under strong light field are traceable recently. Floquet theory [28, 29], a fundamental theorem for optics is applied to condensed matter and generalized
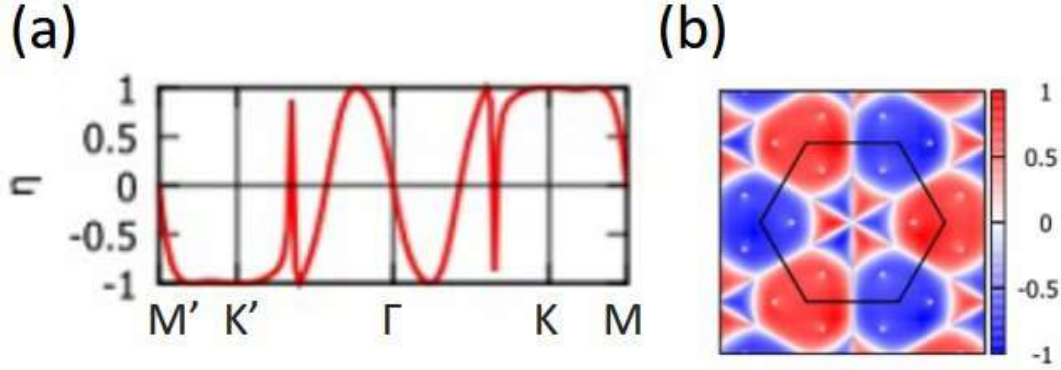
FIGURE 2.6: (a) Degree of circular polarization along the k path of M′, K′, Γ, K, M. (b) Map of $\eta(\mathbf{k})$ in the first Brillouin zone (black line) [24].

as Floquet-Bloch theory. Floquet-Bloch state is an analog of photon dressed state in gas molecules, which has been intensively studied in 1970s [30]. When applying a light-matter interaction term in the Hamiltonian, it will make the Hamiltonian periodic in time domain and the solution of a time-dependent Schrodinger equation becomes a periodic pseudoeigenfunction in both energy and momentum space. Floquet-Bloch state reproduces the band dispersion of the ground state bands with an energy spacing of $\hbar\omega$, which is the photon energy. The first direct observation of Floquet-Bloch state in solid materials is the replica bands of surface state of Bi_2Se_3 [31]. Figure 2.7 shows raw data for TRARPES map of the surface state of Bi_2Se_3 by using p-polarized pump. At Fig. 2.7(d), when pump pulse reaches its max amplitude, a herd of replica bands for original X-shpae surface state had been observed above E_F. By using different polarized pump pulses such as circular polarization, these replica bands may be enhanced and even generate a gap at some special crossing points in the replica bands. Figure 2.8 shows the detailed data in Fig. 2.7(d) along different k paths and differet (circular polarized) pump. The replica bands had been nominated by $n = 0, \pm1, \pm2$, etc. Figure 2.8(c)-(d) are the differential data which are generated by subtracting the data at -500 fs out of the raw data. Differential spectra is a standard treatment to demonstrate the increase or decrease of the spectrum from the equilibrium condition. The size of gap, defined as 2κ, is predicted to be $\sqrt{4V^2 + (\hbar\omega)^2} - \hbar\omega$, where V is the coupling potential that related to the electronic momentum and the fluence of pump pulses, and ω is pump angular frequency [32].

In addition to the direct observation of the electronic structure by TRARPES, some optical measurements also imply the existence of Floquet-Bloch state. An extra effect caused by the Floquet-Bloch bands is the optical stark effect. Figure 2.9 shows the
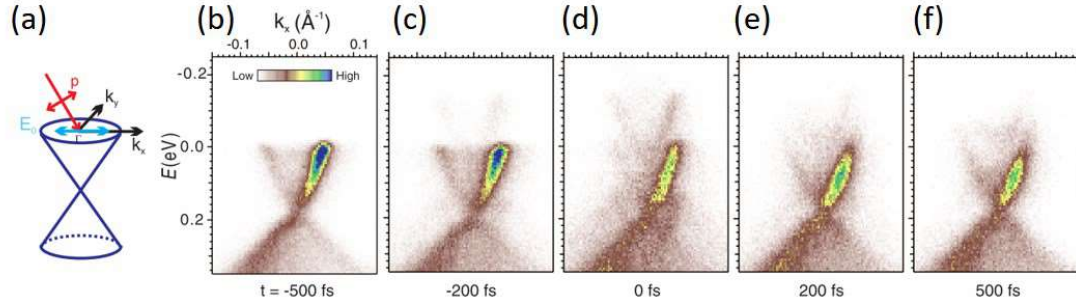
FIGURE 2.7: TRARPES data of Bi_2Se_3 under p-polarized mid-infrared excitation. (a) A sketch of the Dirac-cone-like surface state with the experimental geometry. (b)-(f) show the ARPES map for several different pump-probe time delays from -500 fs to 500 fs [31].
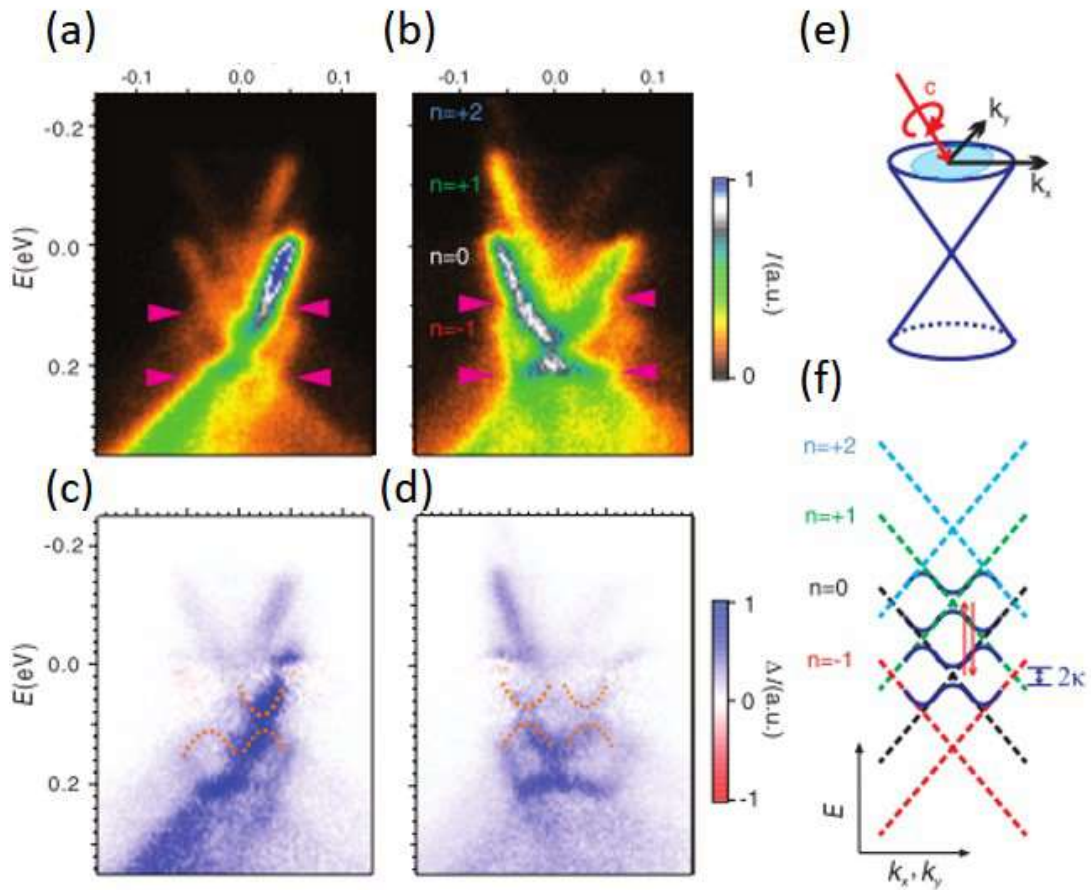
FIGURE 2.8: TRARPES data of Bi_2Se_3 by using circular polarized pump pulses. (a)-(b) show the ARPES map at 0 fs time delay along k_x or k_y. (c)-(d) show the differential data of (a)-(b). (d) The corresponding planes, surface state, k_x and k_y were drawn. (f) Band diagram of Floquet-Bloch states from $n = -1$ to $+2$. The gap opening is defined as 2κ at band crossing points [31].
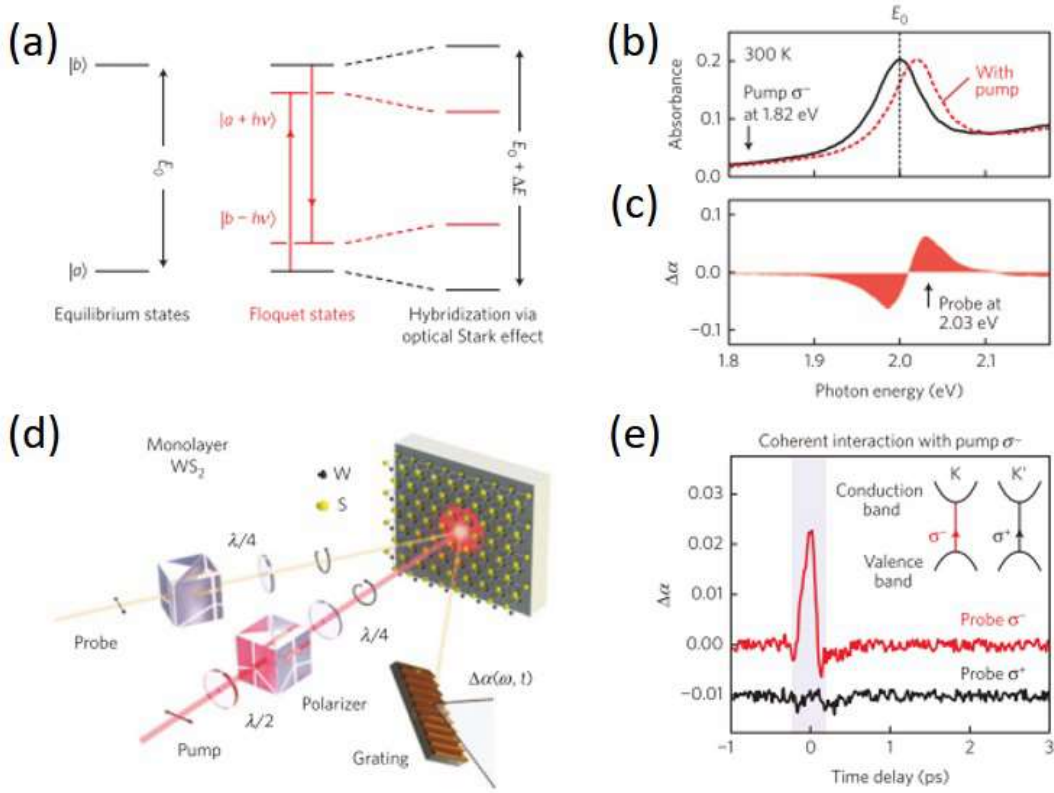
FIGURE 2.9: (a) Energy level diagram of two-level system. $|a\rangle$ and $|b\rangle$ are the original atomic levels, which may hybridize with Floquet states $|a + h\nu\rangle$ and $|b - h\nu\rangle$, and then shift their energy levels. (b) The adsorbance of ML WS$_2$ (solid black line) and the simulated change of adsorbance spectra (red dashed line). The related difference between static (black dashed line) and excited spectra (red dashed line) is shown in (c). (d) The experimental geometry, which shows how to measure the absorption spectra via the transient signal. (e) Time traces of $\Delta\alpha$ by using different polarized light. The sudden change of $\Delta\alpha$, only happend at time zero, and the helicities of pump and probe are the same [15].

optical stark effect in ML WS$_2$ by using circular polarized light. The Floquet states hybridize with original bands such that the band gap shift during the period that pump introduced to the sample (as the sharp peak in Fig. 2.9(e)). Such a band gap change will result in the change in absorption spectrum for the probe light.

Volkov State

Similar to Floquet-Bloch state, the two photon absorption will produce similar replica band in the PES spectra too. When a photonelectron migrates to the surface, it may

be largely affected by the electric field of pump pulses and acquire additional photon energies. This effect has been called as laser-assisted photoemission effect (LAPE) [33]. It is an effect only happens in photoemission. The pump pulses interact with final state of photoelectrons rather then the initial state in the photoemission process. Figure 2.10 shows the energy level diagram and the side peaks of LAPE from the original peak. The wave function of LAPE state can be written as [33]

$$\psi_V(\mathbf{r}, t) = \frac{1}{(2\pi)^{3/2}} \exp(i\mathbf{p} \cdot \mathbf{r}) \sum_{n=-\infty}^{\infty} J_n \left(\frac{\mathbf{p} \cdot \mathbf{E_0}}{\omega_{\mathrm{ir}}^2}, \frac{U_{\mathrm{p}}}{2\omega_{\mathrm{ir}}} \right) \times \exp[-i(\mathbf{p}^2/2 + U_{\mathrm{p}} + n\omega_{\mathrm{ir}})t],$$
(2.5)

where $\mathbf{p}$ is the electron momentum for the field-free case, n is the number of exchanges photons, ω_{ir} is the pump frequency which is usually in infrared, U_{p} is the pondermotive potential, and E_0 is equal to $\omega_{\mathrm{ir}}A_0$. A_0 is the amplitude of vector potential field. $J_n(a, b)$ is the generalized Bessel Function. If the ponderomotive energy is negligible, $J_n(a, 0)$ can be reduced to the ordinary Bessel functions $J_n(a)$.

The intensity of the nth LAPE side band can be approximated as follows [33]:

$$A_n \approx J_n^2 \left(\frac{\mathbf{p} \cdot \mathbf{E_0}}{\omega_{\mathrm{ir}}^2} \right).$$
(2.6)

The inner product $\mathbf{p} \cdot \mathbf{E_0}$ can be reduced to zero by changing the polarization of pump pulses. For the final state, most of the electron's momentum is out of plane. Thus the maximum of LAPE effect will be p-polarization. Figure 2.10 (c) shows the intensity of the first side band, the intensity change as a function of the angle between the surface normal and the electric field of pump light. The intensity of the first side band decreases as a squared cosine function of the angle.

2.4   Surface photovoltage relaxation

This section briefly introduces the basic properties of semiconductor surfaces in equilibrium, and the formation of surface photovoltage and its dynamics after an optical excitation.

Semiconductor Surfaces

Surface always makes a variation from the bulk. In semiconductors, a sudden truncation of the crystal structure may cause a surface reconstruction, or generate a surface
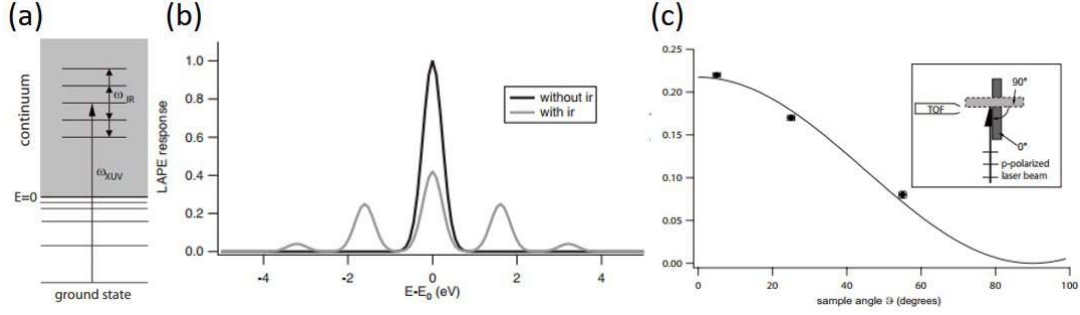
FIGURE 2.10: (a) The principle of LAPE. After the electrons are excited from a ground state to the continuum by the EUV pulses, the free electrons evolves in a ir field provided by pump pulses. The consequence of the interaction between free electrons and ir field is the redistribution of electron state by adsorption or stimulated emission of ir photons. (b) The simulated redistribution of a core level spectrum with or without ir field. (c) The intensity of the first-order LAPE peak as a function of the angle between the polarization of ir field and surface normal [33].

state in the band gap. The extra surface states and/or trapped states vary the surface potential from the bulk. Fig. 2.11 shows eight types of semiconductor surface band bending. There are mainly four surfaces at *p*- or *n*-type semiconductors: inversion, depletion, flat bands, and accumulation. To balance the extra charge and reach the charge neutrality, electrons and holes will be rearranged in space to screen out the surface charge. From bulk to the surface, a charged region is called as the space charge layer (SCL). Electrons and holes are governed by Poisson's equation and the charge neutrality condition:

$$\frac{\mathrm{d}}{\mathrm{d}x}\left(\epsilon_{\mathrm{s}}(x)\frac{\mathrm{d}V}{\mathrm{d}x}\right) = -\rho(x) = -\mathrm{e}(N_{\mathrm{d}} - N_{\mathrm{a}} + p(x) - n(x)),$$

$$Q_{\mathrm{ss}} = -Q_{\mathrm{sc}},$$

(2.7)

where N_{d} and N_{a} are the donor and acceptor densities respectively, which are assumed to be constant in the whole region. p and n are the hole density and the electron density. ϵ is the dielectric constant. Q_{ss} and Q_{sc} are charge at the surface and the total charge in the SCL. In thermal equilibrium, the electron and hole densities in a non-degenerate semiconductor may follow the Boltzmann distribution:

$$n(x) = n_{\mathrm{b}}\exp\left(\frac{\mathrm{e}V(x)}{kT}\right), \ p(x) = p_{\mathrm{b}}\exp\left(\frac{-\mathrm{e}V(x)}{kT}\right),$$

(2.8)

where $V(x)$ is the potential function in space, which is equal to the band bending. $V(x \to \infty)$ is the bulk termination and it is set to be zero. n_{b} and p_{b} are the electron

and hole densities in bulk. In the bulk, the charge should be balanced to zero, thus:

$$N_{\mathrm{d}} - N_{\mathrm{a}} = p_{\mathrm{b}} - n_{\mathrm{b}}. \tag{2.9}$$

Taking Eq. (2.9) and Eq. (2.8) into Eq. (2.7), the Poisson's equation can be rewritten as

$$\frac{\mathrm{d}^2 V}{\mathrm{d}x^2} = -\frac{\mathrm{e}}{\epsilon} \left[p_{\mathrm{b}} \left(e^{-\mathrm{e}V/kT} - 1 \right) - n_{\mathrm{b}} \left(e^{\mathrm{e}V/kT} - 1 \right) \right]. \tag{2.10}$$

From the above equation, the net charge ($Q_{\mathrm{sc}} = -\epsilon_{\mathrm{s}} E_{\mathrm{s}}$) as a function of V can be defined as:

$$Q_{\mathrm{sc}} = \mp \frac{\epsilon_{\mathrm{s}} \sqrt{2} kT}{\mathrm{e} L_{\mathrm{D}}} F \left(\frac{\mathrm{e}V}{kT}, \frac{n_{\mathrm{b}}}{p_{\mathrm{b}}} \right), \tag{2.11}$$

where $L_{\mathrm{D}} \equiv \sqrt{\frac{kT\epsilon_{\mathrm{s}}}{(e^2 p_{\mathrm{b}})}}$ is the Debye screening length. The positive(negative) sign corresponds to $V_s > 0$ ($V_s < 0$). $F\left(\frac{\mathrm{e}V}{kT}, \frac{n_{\mathrm{b}}}{p_{\mathrm{b}}}\right)$ is the so-called space charge function (space charge factor), which is defined as:

$$F\left(\frac{\mathrm{e}V}{kT}, \frac{n_{\mathrm{b}}}{p_{\mathrm{b}}} \right) = \left[\left(e^{-\mathrm{e}V/kT} + \frac{\mathrm{e}V}{kT} - 1 \right) + \frac{n_{\mathrm{b}}}{p_{\mathrm{b}}} \left(e^{\mathrm{e}V/kT} - \frac{\mathrm{e}V}{kT} - 1 \right) \right]^{1/2}. \tag{2.12}$$

The surface band bending is determined by above equation.

Space Charge layer

Space charge layer (SCL) is the region where the carrier density deviates from the bulk due to extra charges in surface states. The depletion approximation is often used to estimate the width of the SCL:

$$|Q_{sc}| \simeq \mathrm{e} \, |N_{\mathrm{a}} - N_{\mathrm{d}}| \, w \tag{2.13}$$

The amount of the net charge can be derived from the space charge function described in Eq. (2.10). By the depletion approximation, the width of the SCL is estimated as $w = \sqrt{\frac{2\epsilon_{\mathrm{s}} V_s}{\mathrm{e}|N_{\mathrm{a}} - N_{\mathrm{d}}|}}$.
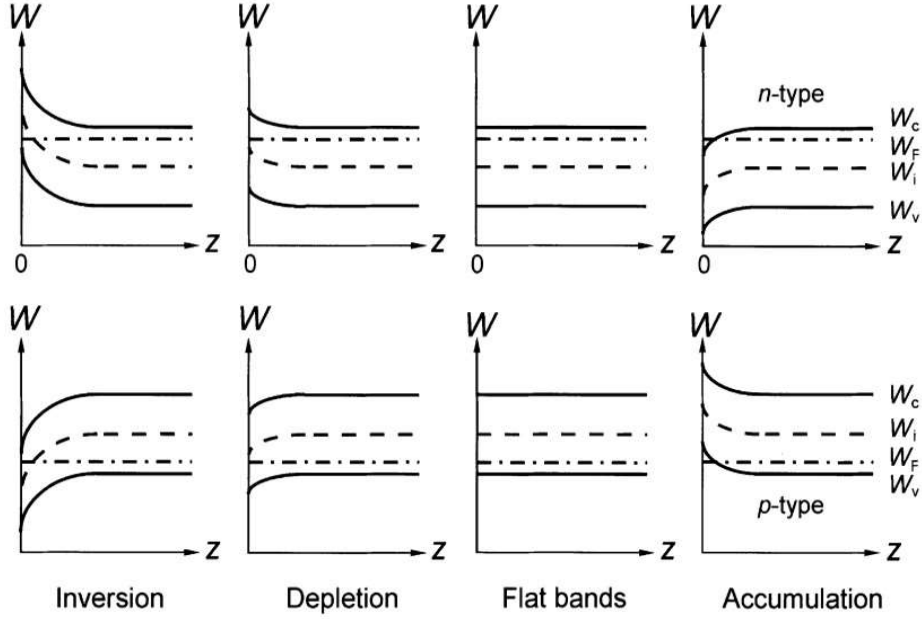
FIGURE 2.11: Band diagrams of different types of semiconductor surface [34].

Carrier transportation equations

The electron and hole currents are governed by the continuity equations:

$$\frac{\partial n}{\partial t} = \frac{1}{e}\frac{\mathrm{d}J_n}{\mathrm{d}x} + G_n - R_n \tag{2.14a}$$

$$\frac{\partial p}{\partial t} = -\frac{1}{e}\frac{\mathrm{d}J_p}{\mathrm{d}x} + G_p - R_p. \tag{2.14b}$$

Where J_n (J_p) is the electron(hole) current density. G_n (G_R) is the electron (hole) generation rate per unit volume. In pump-probe measurement, G_n (G_R) can be assumed to be a Gaussian pulse at t_0. R_n (R_p) is the net electron (hole) recombination rate per volume. The origin of R_n (R_p) will be discussed in the next section.

Also, the electron and hole current follow the drift-diffusion equation:

$$J_n = -e\mu_n n\frac{\mathrm{d}V}{\mathrm{d}z} + eD_n\frac{\mathrm{d}n}{\mathrm{d}z}, \tag{2.15a}$$

$$J_p = -e\mu_p p\frac{\mathrm{d}V}{\mathrm{d}z} - eD_p\frac{\mathrm{d}n}{\mathrm{d}z}, \tag{2.15b}$$

where μ_n, μ_p, D_n, and D_p are electron mobility, hole mobility, electron diffusion coefficient, and hole diffusion coefficient, respectively. The relationship represents the influence of diffusion and drift that also contribute some practical decrease of the electron density.

Recombination process

There are mainly three recombination mechanisms: (1) Shockley-Read-Hall (SRH) surface recombination, (2) Auger recombination, and (3) radiative (bulk) recombination. All of the recombination mechanisms are drawn in Fig. 2.12.

SRH recombination

In SRH recombination, electron and hole carriers recombine through an electron level at E_T, with the density of N_T. The formation of E_T may be resulted from trap state, defect state, etc at the surface. The SRH lifetime is given by

$$\tau_{\text{SRH}} = \frac{\tau_p \left(n_0 + n_1 + \Delta n \right) + \tau_n \left(p_0 + p_1 + \Delta p \right)}{p_0 + n_0 + \Delta n} \tag{2.16}$$

n_0 and p_0 are the equilibrium carrier densities. Δn and Δp are the excess carrier densities. n_1, p_1, τ_n, and τ_p are defined as

$$
\begin{aligned}
n_1 &= n_i \exp \left(\frac{E_T - E_i}{kT} \right) ; \; p_1 = n_i \exp \left(\frac{E_i - E_T}{kT} \right), \tag{2.17a} \\
\tau_n &= \frac{1}{\sigma_n v_{\text{th}} N_{\text{th}}} ; \tau_p = \frac{1}{\sigma_p v_{\text{th}} N_T}, \tag{2.17b}
\end{aligned}
$$

where the σ_p and σ_n are capture cross-sections for electrons and holes to the trapped state, respectively.

Radiative (Bulk) recombination

In radiative recombination process, electron and hole directly recombine from band to band and release the energy by photons. The radiative lifetime is

$$\tau_{\text{rad}} = r_{\text{CV}} \cdot \left(p_{\text{b}} + n_{\text{b}} \right)^{-1}. \tag{2.18}$$

Here, r_{CV} is the radiative recombination coefficient. For p-type WSe_2, $r_{\text{CV}} \sim 2 \times 10^{-6}$ cm^3/s [6]. Thus the bulk recombination time is in the fs range (depending on the bulk hole density).

Auger recombination

In Auger recombination process, the excited electron comes back to the ground state and the recombination energy is adsorbed by the excitation of a third electron. The Auger lifetime is inversely proportional to the square of carrier density, and it can be written as:

$$\tau_{\text{Auger}} = \frac{1}{C_p(p_0 + \Delta n)^2 + C_n(n_0 + \Delta n)^2} \approx \frac{1}{C_p(p_0 + \Delta n)^2}, \tag{2.19}$$

where C_p is the Auger recombination coefficient for hols and C_n for electrons. The approximation in Eq. (2.18) is valid for p-type semiconductor. Generally, C_n or C_p in usual semiconductors is around $10^{-29} \sim 10^{-32}$ cm^6/s.

From above, the total recombination lifetime can be written as

$$\tau_{\text{tot}} = \frac{1}{\tau_{\text{SRH}}^{-1} + \tau_{\text{rad}}^{-1} + \tau_{\text{Auger}}^{-1}}. \tag{2.20}$$

SPV relaxation curve

To extract the carrier lifetime from the SPV effect, the explicit expression of SPV derived from the excess carrier density by optical injection is necessary. Garrett and Brattain [35] did the first approximation and considered a simplest condition, where both the quasi-equlibrium condition in SCL and low-level injection are valid. Johnson [36] derived a delicate model under the large-signal frame. Frankl and Ulmer [37] redefined the SPV under quasi-equilibrium condition and small-signal condition.

The following derivation is based on the small-siganl condition, when the quasi-equilibrium condition will be valid in the SCL. From previous work [36], the excess electron (hole) density(ΔP) generated by injection, can be expressed by:

$$\Delta_p = \frac{(e^{-v_0} + v_0 - e^{-v} - v) + n_0/p_0(e^{v_0} - e^v - v_0 + v)}{e^v - e^{-v} - 2}, \tag{2.21}$$

where $v = V/kT$, and $v_0 = V_s/kT$ in dark. Δ_p is equal to $\Delta P/p_{\text{b}}$. In the quasi-equilibrium condition, the SPV introduced by the excess carriers is approximated as [36]:

$$\frac{V_{\text{SPV}}}{kT} e^{V_{\text{SPV}}/kT} = \Delta_p e^{V_0/kT}. \tag{2.22}$$
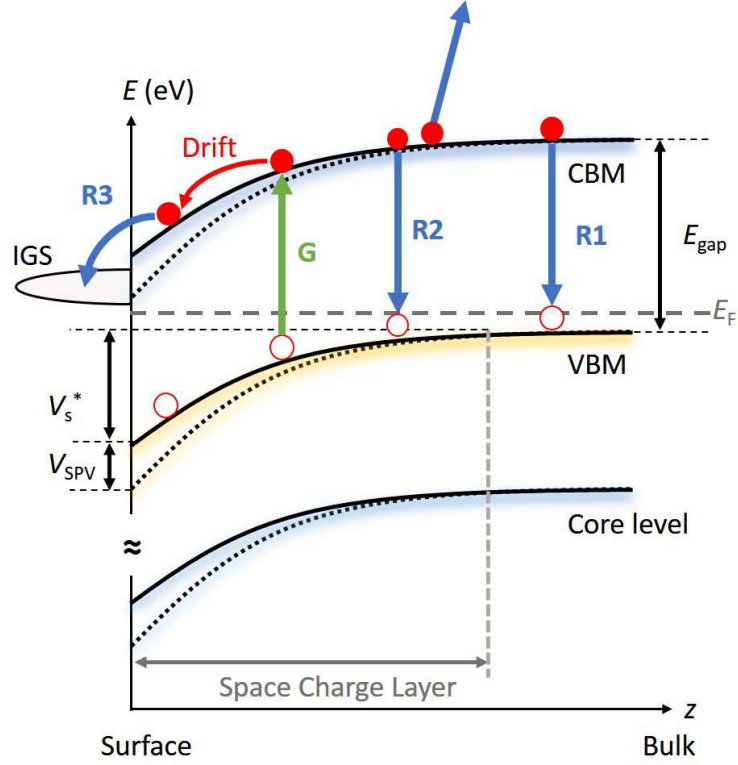
FIGURE 2.12: Band diagrams of p-type WSe$_2$ with different recombination processes. G1: optical excitation, R1:Bulk recombination, R2: Auger recombination, R3: Surface recombination.

In an ideal semiconductor surface, if there is no extra carrier recombination mechanism such as SRH recombination at trapped states, surface states, etc, only tunneling or thermoionic emission can make the electron-hole pair recombination. Tunneling model are described elsewhere [38, 39]. Thermoionic model was proposed by Hecht [40] and confirmed by many experimental results [41, 42], which predicted the relaxation time between surface charge and SPV by

$$\tau(\mathrm{SPV}) = \tau_\infty e^{-V_{\mathrm{SPV}}/\eta kT},\tag{2.23}$$

where τ_∞ is the dark carrier lifetime, an intrinsic property from the carriers. From the above equations, the SPV relaxation after light pulses can be derived as

$$\frac{\mathrm{d}\Delta_p}{\mathrm{d}t} = -\frac{\Delta_p}{\tau_\infty} e^{V_{\mathrm{SPV}}/kT}.\tag{2.24}$$

Thus, the SPV can be written as a function of t:

$$V_{\mathrm{SPV}}(t) = -\eta k_B T \ln \left[1 - \left\{ 1 - \exp \left(-\frac{V_{\mathrm{SPV}}(0)}{\eta k_B T} \right) \right\} e^{-t/\tau_\infty} \right], \qquad (2.25)$$

where η is the ideality factor in the diode theory. $V_{\mathrm{SPV}}(0)$ is the induced SPV at $t \sim 0$ after the optical injection and SPV generation.

2.5   Adsorbates on TMDC semiconductor surfaces

Metal adsorbates on TMDC semiconductor surfaces

Metal-Semiconductor and Organic molecules-Semiconductor interfaces have been intensively studied for a long time since 1990s. In the old times, the focusing issue is how the metal contact to the surface and the band bending at the very surface and its Schottky-barrier. As shown in Fig. 2.13, the band bending as a function of metal adsorbates coverage is carefully examined by the energy shift in eletronic core levels in XPS spectra. Many alkali metals and noble metals on TMDC surfaces have been done: Rb/WSe$_2$ [6], Cu/WSe$_2$ [43], Ag/WSe$_2$ [43] , In/WSe$_2$ [3], and Na/WSe$_2$ [44], etc. With the usage of 3rd generation synchrotron light sources, the synchrotron light induced SPV shift has been found. Figure 2.13 shows the energy shift in W $4f$, Se $3d$, and In $3d$. The energy shift of W $4f$ and Se $3d$ reach to their maximum, around 0.5 eV, at the very small coverage of In. Mostly the band bending of semiconductor surface saturate below the coverage of 1 ML metal adsorbates.

Organic adsorbates on TMDC semiconductor surfaces

In solar cell technology, one of the typical models is the type-II solar cell [45], which is formed by a donor-acceptor interface. This interface can separate electron and hole pairs well in space and improve the total photoconversion. Since TMDC semiconductors are inert in (001) surfaces, they can be the good grounds to produce the donor-acceptor interface. Among all the organic molecules, C$_{60}$ is a very inert and heavy molecule. With these advantages, C$_{60}$ can form an inert and stable top layer at the interface, which is the ideal photovoltaic heterojunction device [46]. Figure 2.14 shows the simple model to describe how the electron-hole pairs generate and relax at the organic-semiconductor surfaces.
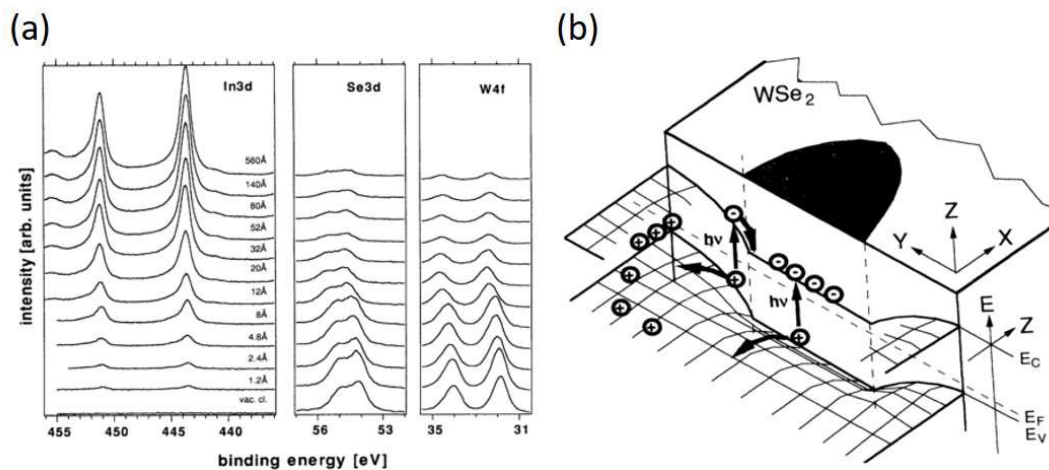
FIGURE 2.13: (a) Core level spectra of In/We$_2$ interface with increasing In deposition. (b) Schematic drawing of the energy level condition of the In clusters/ WSe$_2$ interface. Band bending and charge-carrier transport are expected to be spread both in normal and in parallel directions from In clusters to the WSe$_2$ surface [3].
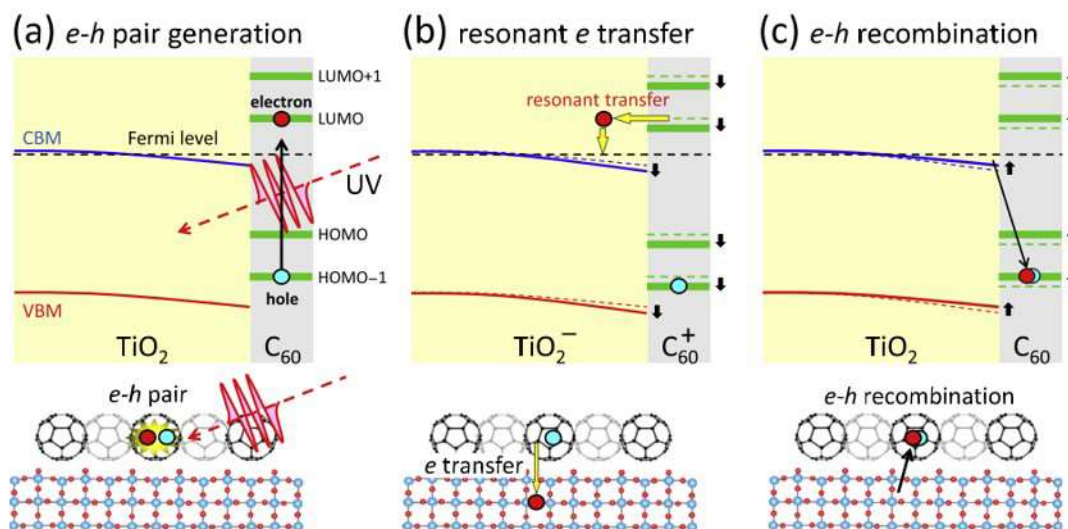
FIGURE 2.14: The elemental steps for the SPV relaxation on C$_{60}$/TiO$_2$ surface. (a) The electron-hole pair generation in C$_{60}$ layer. (b) The resonant electrons transfter from C$_{60}$ layer to TiO$_2$ surface. The excess electron density at TiO$_2$ surface drives a band bending in TiO$_2$. (c) The electron-hole pairs recombine at HOMO−1 energy level, all the energy levels back to equilibrium conditions [47].

Chapter 3

Experimental methods

This chapter gives a brief overview of the principle of photoemission spectroscopy, and the introduction of pump-probe time-resolved photoemission spectroscopy. After the principles and introduction, the experimental setup of TRARPES at ISSP (University of Tokyo), TRARPES at Artemis (CLF, RAL, UK), and TRXPS at BL07LSU (SPring-8) will be described.

3.1 Principles of photoemission spectroscopy

Photoemission spectroscopy (PES) has been established as one of the most powerful tool to study the electronic structure of molecules, solids and surfaces. Since PES can offer straightforward information of electronic structure of materials without any damage, it has been widely used in many fields such as surface chemistry, material science, surface science. In this section we would like to give an overview of photoemission process, ARPES, and XPS.

3.1.1 Photoemission spectroscopy

The origin of Photoemission spectroscopy is the observation of photoelectric effect done by Heinrich Hertz (Karlsruhe) and Wilhelm Hallwachs (Dresden) in 1887. In their experiment, negative charges burned out from a metal surface while illuminating the surface with a violet light. Later, Einstein proposed the concept of photon and the fundamental equation to describe the relation between photon energy and maximum
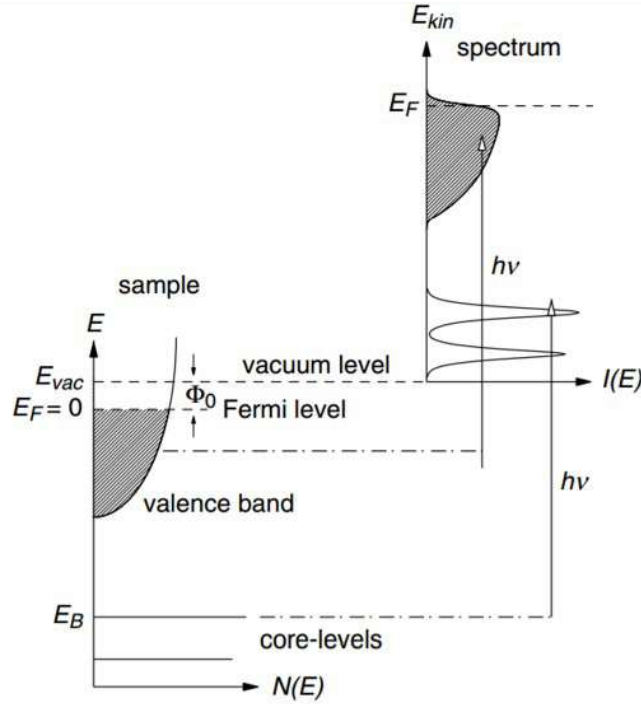
FIGURE 3.1: Schematic picture of photoemission process [48].

kinetic energy of electron, which is:

$$E_{\mathrm{kin}} = h\nu - \Phi. \tag{3.1}$$

E_{kin} is the maximum kinetic energy of electron, Φ is the work function of the measured material. $h\nu$ is the photon energy. Φ is the difference between Fermi energy (E_{F}) and the vacuum level (E_{vac}). A schematic diagram of the principle of photoemission spectroscopy is illustrated in Fig. 3.1. Considering a general photoemission process, the kinetic energy can be expressed as:

$$E_{\mathrm{kin}} = h\nu - \Phi - E_{\mathrm{B}}. \tag{3.2}$$

Here, the E_{kin} is given by $E_{\mathrm{F}} - E_{\mathrm{vac}}$, as shown in Fig. 3.1. In convention, it is more straightforward to see the physics of the PES spectra when the E_{kin} has been rewritten as:

$$E_{\mathrm{kin}} = h\nu - E_{\mathrm{B}}, \tag{3.3}$$

where E_{B} is the binding energy, which can be expressed by $E_{\mathrm{F}} - \epsilon_k$ according to Koopmans' theorem. ϵ_k is the Hartree-Fock orbital energy. The photoemission spectrum $I(E_{\mathrm{B}})$ satisfy above condition, and the intensity is proportional to the density of

states, can be simply described as:

$$I(E_{\mathrm{B}}) \propto \sum_k \delta(E_{\mathrm{B}} - E_{\mathrm{F}} + \epsilon_k) \propto N(E_{\mathrm{F}} - E_{\mathrm{B}}). \tag{3.4}$$

Photoemission process is a very complicated many-body problem. Over the decades, people generally use the Fermi's golden rule as a result of perturbation theory to the first order:

$$J_k(h\nu) = \frac{2\pi}{\hbar} \sum_s |\langle \psi_{k,s}|H'|\psi_i\rangle|^2 \delta(\epsilon_k - \epsilon_s - h\nu). \tag{3.5}$$

The index s represents a set of quantum numbers of all possible excitation of the final state, such as phonons, plasmons, electron-hole pairs and multiple excitation. The perturbation term H' describes the interaction between an electron and the electromagnetic field $\mathbf{A}$:

$$H' = \frac{\mathrm{e}}{2mc}(\mathbf{A} \cdot \mathbf{P} + \mathbf{P} \cdot \mathbf{A}) + \frac{\mathrm{e}^2}{2mc^2}\mathbf{A}^2 + eV(r) \tag{3.6}$$

However, it is difficult to calculate the spectrum without any approximation. A very common approximation called as "sudden approximation" is often used. In sudden approximation, the final state $|\psi_f\rangle = |\psi_{k',s}\rangle$ is decoupled from the (N-1)-electron system. Thus the final state can be replaced by

$$|\psi_{k,s}\rangle = |k; N - 1, s\rangle \rightarrow c_{k,s}^{\dagger}|N - 1, s\rangle. \tag{3.7}$$

From above approximation, the photocurrent can be represented by

$$J_k(h\nu) = \frac{2\pi}{\hbar} \left\langle \psi_k \left| H' \right| \psi_{k'} \right\rangle^2 \sum_s \left\langle \psi_{k,s} \left| c_{k,s} \right| \psi_{k',s'} \right\rangle^2 \delta(\epsilon_k - \epsilon_s - h\nu)$$

$$= \frac{2\pi}{\hbar} \sum_{k'} |\Delta_{kk'}|^2 A_K^{<}(\epsilon_k - h\nu), \tag{3.8}$$

where $\Delta_{kk'} = \langle \psi_k|H'|\psi_{k'}\rangle$, is the transition probability from a single electron at state ψ_k to the final state $\psi_{k'}$. The rest term is the so-called spectral function $A(\omega, k)$ is

$$A_K^{<\omega} = -\frac{1}{\pi}\Im\left\{G_K(\omega - i0^+) \cdot f_{\mathrm{FD}}(\omega, T)\right\}, \tag{3.9}$$

where $f_{\mathrm{FD}}(\omega, T)$ is the Fermi-Dirac distribution, and the Green's function is

$$G_K(\omega) = \frac{1}{\omega - \epsilon_K - \sum_K(\omega)}, \tag{3.10}$$
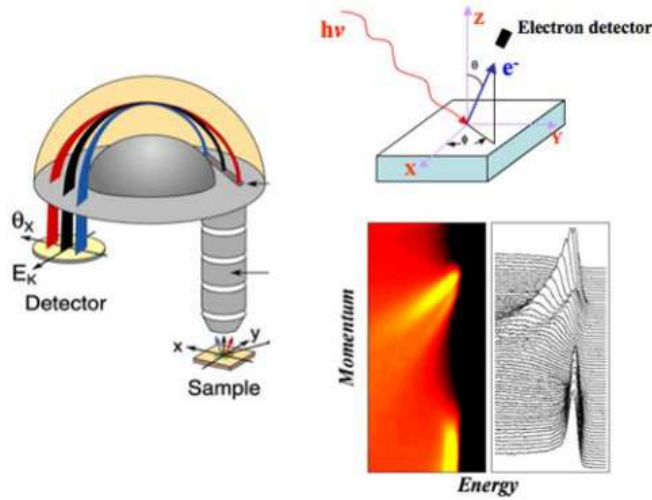
FIGURE 3.2: Schematic picture of angle-resolved photoemission spectroscopy [48].

where $\sum_K(\omega)$ is the self-energy which contains all the contributions from many-body processes, such as electron-electron interaction, electron-phonon interaction that play a key role to the line width or line shape in photoemission spectrum. For example, the famous Mahan-Doniach-Sunjic (MDS) line shape is an asymmetric quasi-particle line shape generated by the low-energy electron-hole excitation in the conduction bands. It has been found in core-levels of metals.

From above, sudden approximation gives an appropriate prediction to the main feature of the photoemission spectrum such as the primary core level peak position and its line width. However, this approximation is suited to describe the electron at higher kinetic energy, or electrons in atoms or molecules. In solids, some extrinsic energy losses need to be considered. In three step model, the energy loss has been treated by a convolution of the spectral function with a loss function. In general, Touggard or Shirley background are used to get rid of the signal from inelastic scattering.

3.1.2   Angle-resolved photoemission spectroscopy (ARPES)

ARPES is the only tool to determine the electronic band structures of solid materials in all the experimental techniques. The electronic band structures from Fermi level to several tens eV of binding energy is the most important valence band region. In this range, electrons are governed by the crystal periodicity and Bloch theorem such that the electron posses not only eigen energy but also eigen momentum. For the Bloch electron,

the momentum change should follow the momentum conservation law as below:

$$k_{\mathrm{f}} = k_{\mathrm{i}} + k_{\mathrm{ph}} + G, \tag{3.11}$$

where k_{i} and k_{f} are the wave vector of the electron at initial and final state, k_{ph} is the wave vector of the incident photon, and G is an arbitrary reciprocal lattice vector. k_{ph} is usually negligible since the wave vector of a photon in EUV to soft x-ray range is about hundred time smaller than G or k_{i}. While the electrons at final states travel to the surface, the perpendicular component of electron's wave vector is decreased due to the potential barrier of the inner potential. The parallel component still conserved and the momentum is dependent with the emission angle, as below:

$$k_{\mathrm{f}\parallel}^{\mathrm{v}} = k_{\mathrm{f}\parallel}, \tag{3.12}$$

$$k_{\mathrm{f}\perp}^{\mathrm{v}} = \frac{\sqrt{2m_e(E + \hbar\omega - \Phi)\cos^2\theta + V_0}}{\hbar}, \tag{3.13}$$

where V_0 is the inner potential.

Up to now, there are two types of detectors, hemispherical analyzer and time of flight analyzer. Figure 3.2 indicates a conventional hemispherical type analyzer. The photoelectrons in vacuum travel along the hemispherical track with a central electric field and then multiplied by a Multi-channel plate to be detected by a camera. The intensity distribution in energy axes is defined as energy distribution curve (EDC), while the distribution along angle axes is called as momentum distribution curve (MDC).

The hemispherical analyzer can be used with any kind of light sources such as He discharge lamp, Laser source, and synchrotron source while the time of flight analyzer can be only used with ultrafast light pulses generated by ultrafast laser pulse, synchrotron pulse generated in bunch mode.

3.1.3 Inelastic electron mean free path

In all the photoemission spectroscopy process, the probing depth is decided by the escaping length of photoelectrons. This also decide the surface sensitivity from different light sources. Figure 3.3 shows the universal curve of inelastic electron mean free path (IMFP) of different elements. Most materials share the similar IMFP at the same kinetic energy. The phenomenological function for the universal curve is [49]

$$\lambda(E) = \frac{143}{E^2} + 0.054\sqrt{E}, \tag{3.14}$$
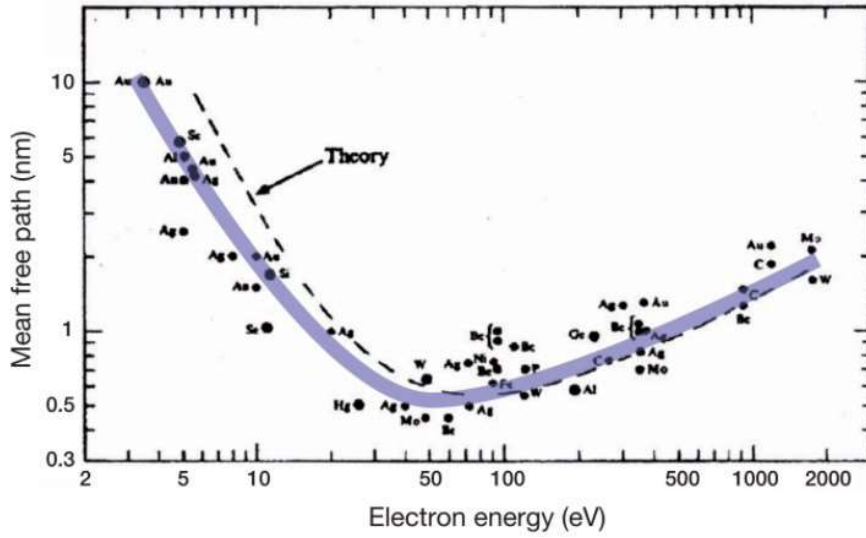
FIGURE 3.3: Universal curve of inelastic mean free path of electron [49].

where a is the thickness a monolayer in nm. The most surface sensitive range locate around 50 eV, which can usually be excited by an EUV light source. At the kinetic energy about 100~1000 eV, the IMFP is about 1 nm, which is the probing depth for usual soft-xray XPS.

In XPS measurement,the IMFP is often used to decide the thickness of an adsorbate on a surface. The intensity of an element peak from the pristine surface will be decrease by:

$$I' = I \times e^{\left(-\frac{d_{\mathrm{ads}}}{\lambda_{\mathrm{ads}} \cos\theta}\right)} \tag{3.15}$$

Where I is the primary peak intensity from a specified element of the surface. I' is the peak intensity after the deposition of the adsorbate. λ_{ads} is the IMFP of the adsorbate at a certain kinetic energy. θ is the incidence angle, which is about 0 to 30°. $\lambda_{\mathrm{ads}}(E)$(IMFP) can be estimated by TPP-2M IMFP equation [50]

$$\lambda = \frac{E}{E_p^2[\beta \ln(\gamma E) - (C/E) + (D/E^2)]}. \tag{3.16a}$$

$$\beta = -0.10 + 0.944(E_{\mathrm{p}}^2 + E_{\mathrm{g}}^2)^{-1/2} + 0.069\rho^{0.1} \tag{3.16b}$$

$$\gamma = 0.191\rho^{-1/2} \tag{3.16c}$$

$$C = 1.97 - 0.91U \tag{3.16d}$$

$$D = 53.4 - 20.8U \tag{3.16e}$$

$$U = N_{\mathrm{v}}\rho/M = E_{\mathrm{p}}^2/829.4 \tag{3.16f}$$
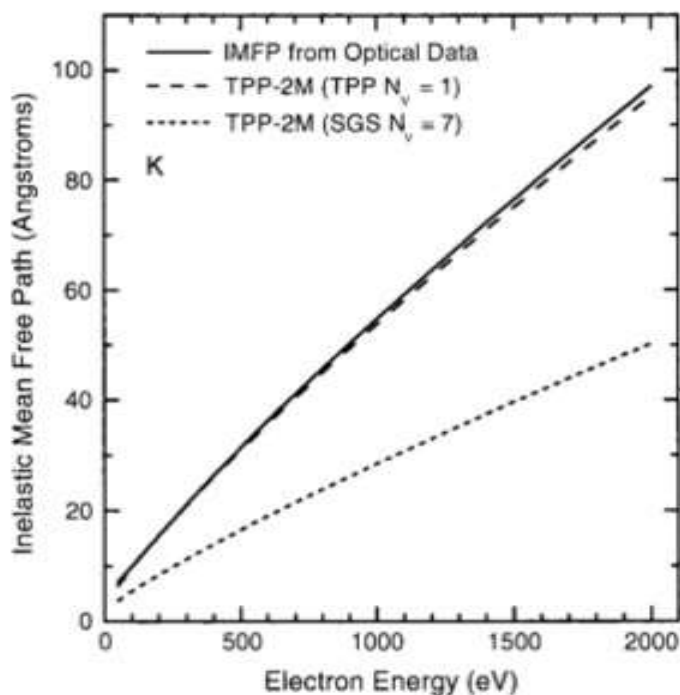
FIGURE 3.4: Inelastic mean free path (IMFP) of K. Optical data (Solid line), calculated curves by TPP-2M equations with different parameters (dashed curves) [50].

where E is the kinetic energy, E_g is the band gap of material, ρ is the density of material, M is the molecular weight, N_v is the number of valence electrons.

3.1.4   High-harmonic generation

High-harmonic generation (HHG) is a nonlinear optical process which can be generated by an intense ultrafast pulsed laser in a noble gas environment. The frequency of the fundamental laser (usually near-infrared to Visible) is converted into its integer multiples. The intensity of HHG in frequency domain can generally separated into two parts, plateau region and cutoff region. The cutoff photon energy is

$$E_c = I_p + 3.17U_p, \tag{3.17}$$

where I_p is the ionization potential of noble gas molecule, and U_p [eV] is the ponderomotive energy, which is often written as $E_0^2/4\omega_0^2$ or $9.337 \times 10^{-14}I$ [W/cm^2]($\lambda[\mu$ m])^2 For the theoretical explanation, there are three prevailing models: Three Step Model (TSM), Lewenstein model, and Gaussian Model. TSM is the most well known

model and the easiest one to explain under semicalssical physics rather than quantum mechanics. Surprisingly, most predictions of TSM are as precise as the more delicate solution of the time-dependent Schrodinger equation.

In TSM, electron's motion is separated into 3 parts as in Fig. 3.5: 1. An electron is ionized to the continuum at the nuclear position, and is accelerated by the oscillating electric field and propagate away from the nuclear core. 2. The electron is decelerated by the oscillating electric field and back to the core of the atomic center. 3. The electron recombines to the nuclear with an emitted photon, whose photon energy is equal to the loss of the kinetic energy of electron.

Considering the motion of an electron that ejected under a laser in which the electric field is written as $E(t) = E_0 \cos \omega_0 t$, the equation of motion is

$$m_e \frac{\mathrm{d}^2 x}{\mathrm{d}t^2} = \mathrm{e}E \cos(\omega t) \tag{3.18}$$

by solving the equation of motion with the initial condition at $t = t_i$, when the electron is ejected with the conditions that $x(t_i) = 0$ and $\dot{x}(t_i) = 0$, the solution of electron's motion is

$$x(t) = \frac{E_0}{\omega_0^2} \left[(\cos \omega_0 t - \cos \omega_0 t_i) + (\omega_0 t - \omega_0 t_i) \sin \omega_0 t_i \right]. \tag{3.19}$$

And the kinetic energy E_{kin} is:

$$E_{\mathrm{kin}}(t) = 2U_{\mathrm{p}}(\sin(\omega_0 t) - \sin(\omega_i t_i))^2. \tag{3.20}$$

When the electron recombines, $t = t_r$ and $x(t_r) = 0$, the energy of emitted photon is given by $E_{\mathrm{kin}}(\omega t_r) + I_{\mathrm{p}}$. The whole condition can be classified into 4 conditions: long trajectory ($0 < \omega t_i < 0.09\pi$), cutoff trajectory($\omega t_i \approx \pi$), short trajectory ($0.09\pi < \omega t_i < \pi/2$), and Non-return trajectory ($\pi/2 < \omega t_i < \pi$). The cutoff trajectory gives the maximum of photon energy, which is $3.17U_{\mathrm{p}} + I_{\mathrm{p}}$.

While replacing the phase $\omega_0 t$ into $\omega_0 t + m\pi$, the sign of $x(t)$ changes for each half cycle. This means the harmonics are generated in each half cycle with opposite phase which may add destructive contribution. Therefore only odd number of high harmonics generation can be generated by gas media.
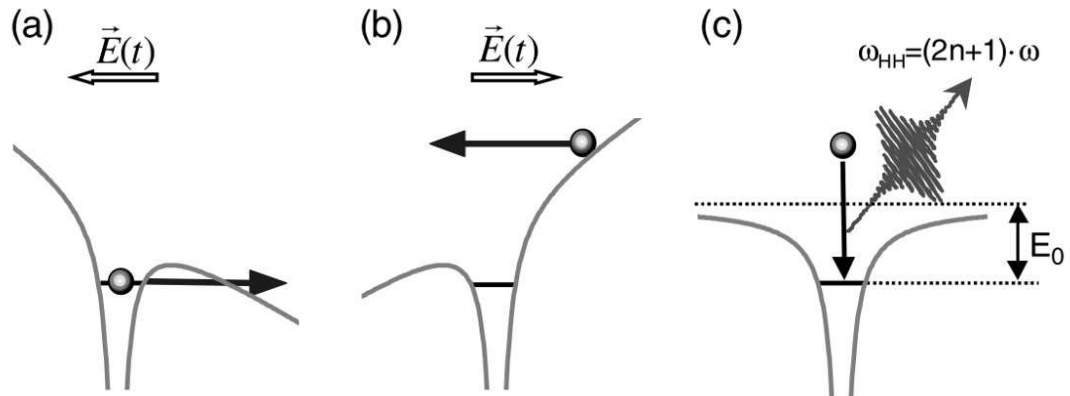
FIGURE 3.5: Schematic diagram of Three step model [51]. (a) An electron tunnel through the atomic potential barrier that has been distorted by the tense laser field, and then is accelerated away from the atomic core. (b) When the laser field reverses, the electron was decelerated and back to the core of atom. (c) The electron recombines with the atom and release a photon at an odd harmonics of the laser photon energy.

3.2 Experimental setup

3.2.1 Time-resolved ARPES at ISSP, University of Tokyo

This system was commissioned in 2011 [52]. This TRARPES station is composed of a chirped pulse amplifier (CPA) system of the Ti:Sapphire laser, high harmonic generation chamber and a hemispherical photoemission analyzer (VG Scienta R4000). The HHG beam was generated by using the second harmonics (400 nm) of a fundamental Ti:Sapphire laser and a gas cell filled with Ar gas. 9th (27.3 eV) HHG has been selected by the double multilayer mirror (MLM, SiC/Mg) monochromator [53]. The pump beam is the fundamental laser with the wavelength of 800 nm. The time duration of pump beam is 35 fs. The cross correlation between pump and probe is about 83 fs, which is extracted from the temporal response of a reference sample, HOPG. Figure 3.7 shows the schematic diagram of the TRARPES system. HHG beams are generated in the HHG chamber with a gas cell filled with Ar gas. The HHG beams can be examined by a spectrometer after a grating. A pair of multi-layer mirror [53] used as the monochromator is mounted in a MLM chamber. Multi-layer mirrors were mounted near normal incidence to suppress the temporal broadening effect. Moreover, the total reflectivity of double multi-layer mirrors is about 0.3, which is the highest among all the monochromators for ultrafast EUV beams.
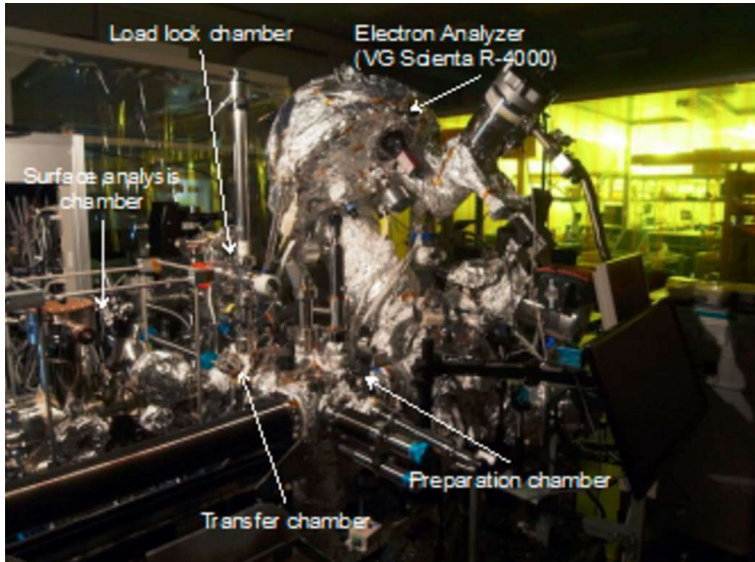
FIGURE 3.6: Photo of TRARPES system [54].
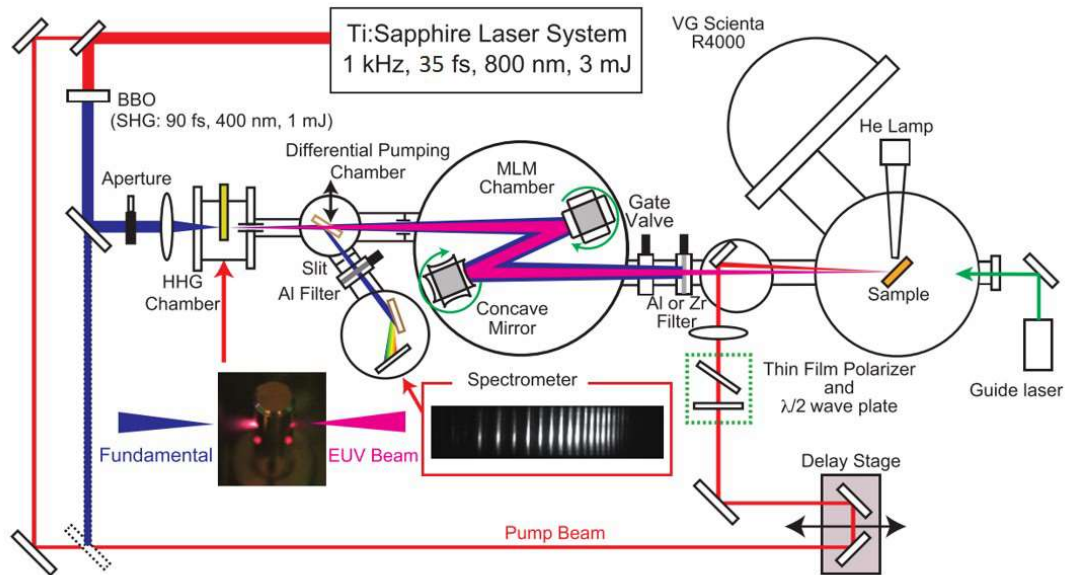
FIGURE 3.7: Schematic diagram of TRARPES system [54].

3.2.2   Time-resolved ARPES at Artemis, Central Laser Facility, Rutherford Appleton Laboratory

This section gives a brief overview of the Artemis beamline of Central Laser Facility, Rutherford Appleton Laboratory in United Kingdom. Artemis beamline provides versatile ultrafast, synchronized laser sources. The laser sources are:

1. High power Ti:sapphire laser system (12 mJ at 1 kHz in 30 fs pulse)

2. Few-cycle laser pulses: 8 fs pulses centered at 800 nm with 0.5 mJ/pulse or 12 pulses at 1800 nm with 0.4 mJ/pulse.

3. Tuneable pump pulses from 235 nm to 15 micron (Fig. 3.11)

4. Tuneable EUV beamline with a monochromator, providing isolated, short pulse (10-50 fs) harmonics in the energy region 12-80 eV

5. EUV imaging beamline with flat-field spectrometer, filters and multilayer mirrors, for experiments requiring higher EUV flux.

There are 4 end stations aimed at different fields such as condensed matter physics or atomic and molecular physics:

1. Time- and angle-resolved photoemission (ARPES) chamber.

2. EUV time-of-flight chamber for studies of ultrafast demagnetization.

3. AMO chamber with velocity-map imaging or electron time-of-flight detector and gas sources.

4. Chamber for liquid-phase studies, equipped with a liquid microjet.

Figure 3.8 shows the schematic diagram of the EUV beamline. EUV beams were generated in a gas cell located at HHG chamber. The monochromator is a time-preserving monochromator (TPM) using a single-grating type in the off-plane mount (OPM) [55]. Figure 3.10 shows the optical path of EUV beam under the blaze angle condition. The advantage for TPM type grating is the quick selection of HHG beam in a wide range while keeping the pulse duration and the acceptable transmission efficiency. With the off-plane mount, EUV beams will be expanded onto a plane which is vertical to the groove of the grating. By rotating the grating, EUV beams at different energies can be easily selected. To make perfect diffraction, a pair of toroidal mirrors are necessary, one for collimating the mixed EUV beams coming from the entrance slit and the other one mounted in front of the end slit to focus the selected EUV beam after the grating. Table 3.1 shows the basic parameters for 4 gratings equipped in Artemis monochromator chamber. In the recombination chamber in Fig. 3.8, a toroidal mirror was used to collimate the HHG beam and a D shape mirror is mounted in the chamber to reflect pump beam to the center of analyzer chamber. Figure 3.9 shows the schematic

diagram of the end station. The station provides many standard equipment for surface science such as LEED, He lamp, e-beam heating system, MBE chamber, etc. The ARPES analyzer is SPECs Phoibos analyzer.

TABLE 3.1: Parameters of the ARTEMIS monochromator [55].

Spectral region	12-120 eV	
Toroidal mirrors	Incidence angle	3°
	Input/output arms	300 mm
	Radii	11470 mm(tangential)×
		31.4 mm(sagittal)
Gratings	Altitude	
G1	Energy region	12-40 eV
	Groove density	60 gr/mm
	Blaze angle	1.25°
	Peak efficiency	28 eV
	Bandwidth (50-μm slit)	$\Delta\lambda$ =2.8 nm, ΔE =1.7 eV @28 eV
	Shortest EUV pulse duration	10 fs
G2	Energy region	30-120 eV
	Groove density	120 gr/mm
	Blaze angle	1.1°
	Peak efficiency	62 eV
	Bandwidth (50-μm slit)	$\Delta\lambda$ =1.4 nm, ΔE =4.3 eV @62 eV
	Shortest EUV pulse duration	10 fs
G3	Energy region	12-40 eV
	Groove density	300 gr/mm
	Blaze angle	1.25°
	Peak efficiency	28 eV
	Bandwidth (50-μm slit)	$\Delta\lambda$ =0.6 nm, ΔE =0.3 eV @28 eV
	Shortest EUV pulse duration	56 fs
G4	Energy region	30-120 eV
	Groove density	500 gr/mm
	Blaze angle	4.7°
	Peak efficiency	62 eV
	Bandwidth (50-μm slit)	$\Delta\lambda$ =0.3 nm, ΔE =1.0 eV @62 eV
	Shortest EUV pulse duration	40 fs

3.2.3   Time-resolved XPS at BL07 LSU, SPring-8

TRXPS station at BL07LSU, SPring-8 was commissioned in 2012 [57]. This experimental station combined the synchrotron radiation (SR) pulses, fs laser system, and a state-of-art time-of-flight (TOF) analyzer. The advantage of TOF analyzer is the high electron transmission efficiency, which is 100 times larger than a conventional hemispherical analyzer and is very helpful for reducing the data acquisition time.
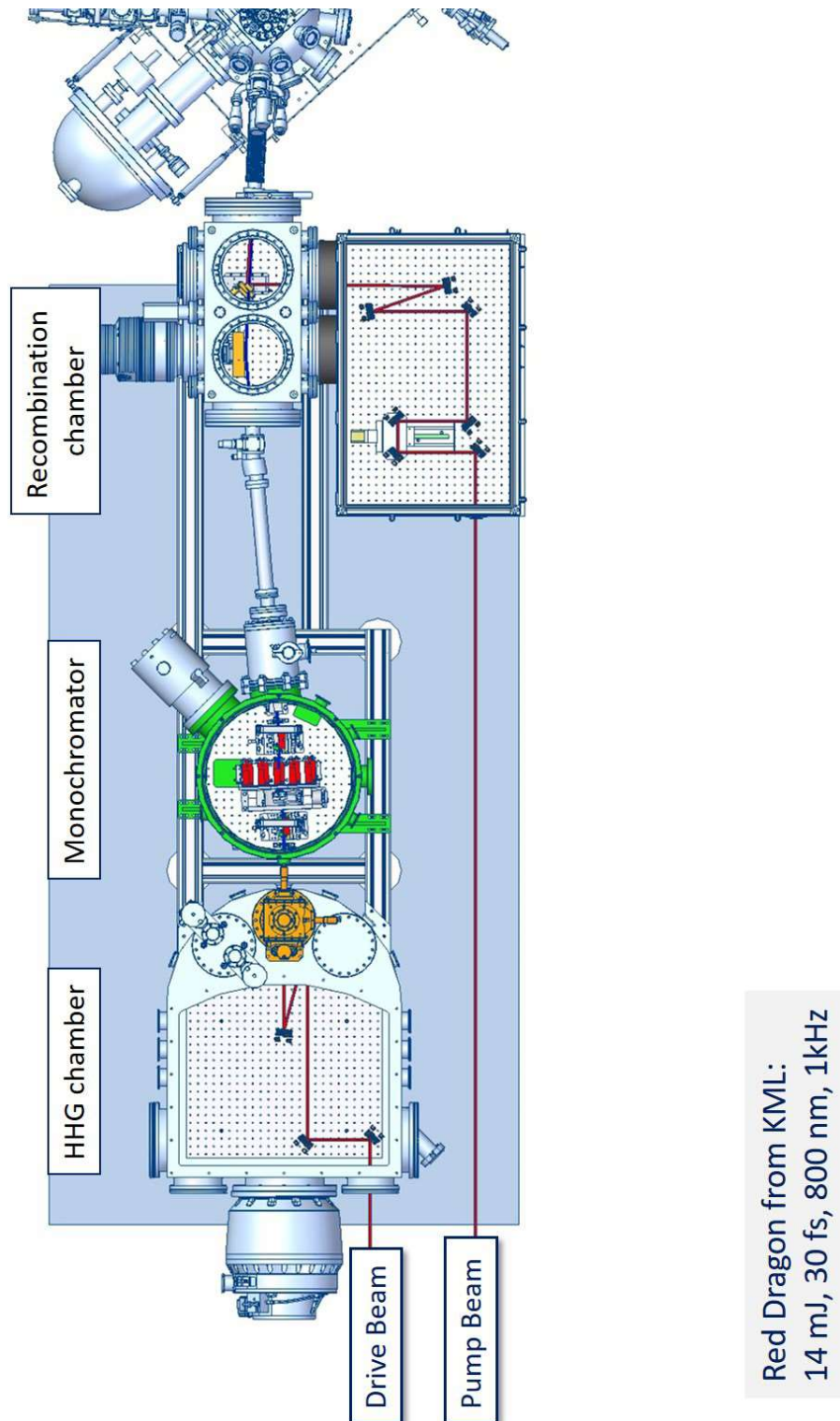
FIGURE 3.8: Drawing of the EUV beamline at Artemis Beamline, Central laser facility, Rutherford Appleton Laboratory. The drive beam was introduced to HHG chamber quipped with a gas cell. In the monochromator chamber, EUV beams are collimated by a toroidal mirror, diffracted by a grating, and finally focused by a toroidal mirror. In the recombination chamber, EUV beam was collimated by a toroidal mirror and the pump beam from outside is guided by a D shape mirror.

User's evaporator

LoadLock

5-axis manipulator

He lamp

Prep Manipulator

Laser Beams

User's evaporator

Electron analyser

LEED

User's UHV suitcase

ARTEMIS
- Phoibos 100 analyser
- resolution of 400 meV, 0.3°, 30 fs
- probe pulses in 10–100 eV range
- pump pulses in 86 meV – 5 eV range
- liquid He cooling, presented measurements obtained on 50 K
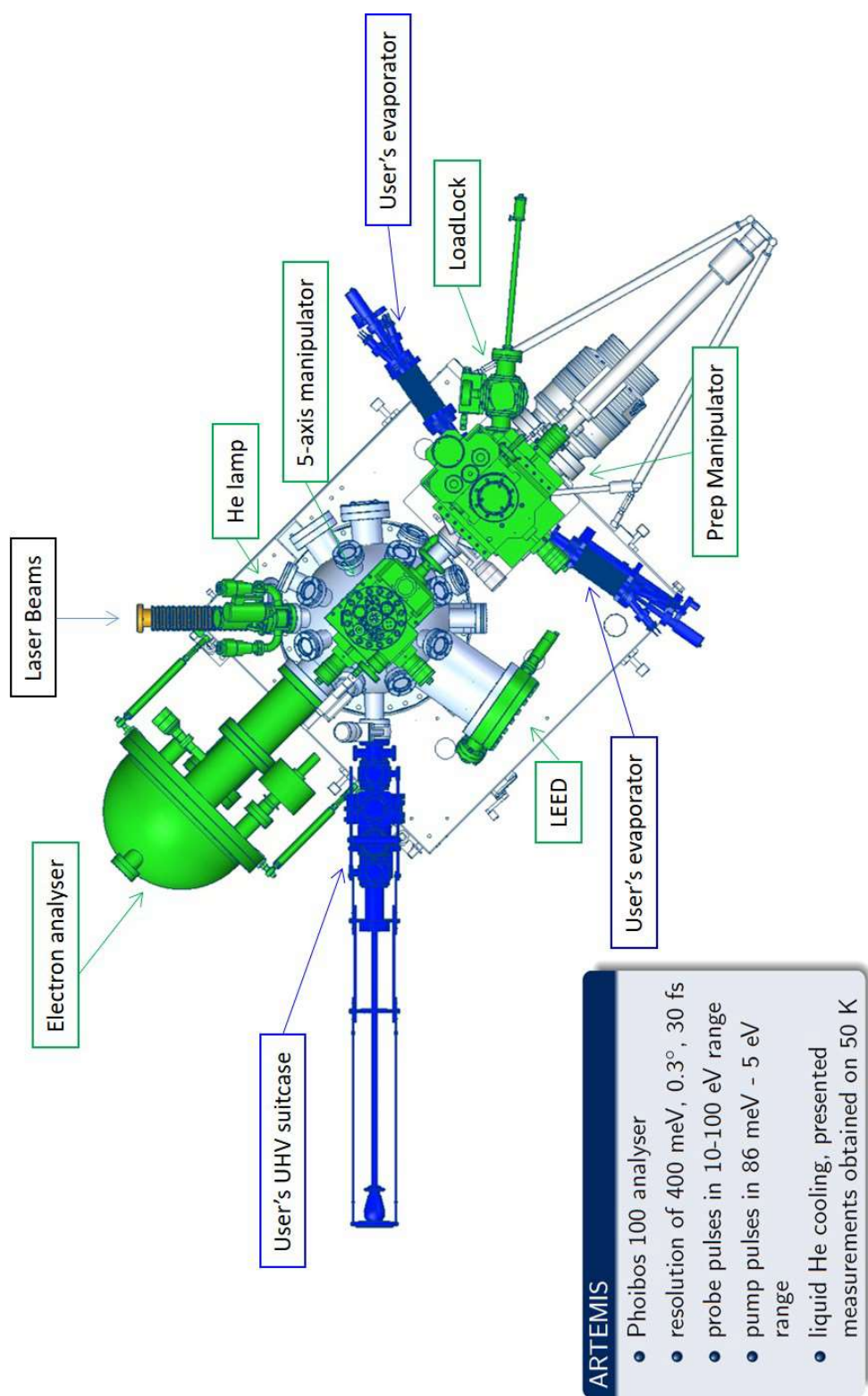
FIGURE 3.9: Drawing of the TRARPES station in Artemis Beamline, Central Laser Facility, Rutherford Appleton Laboratory.
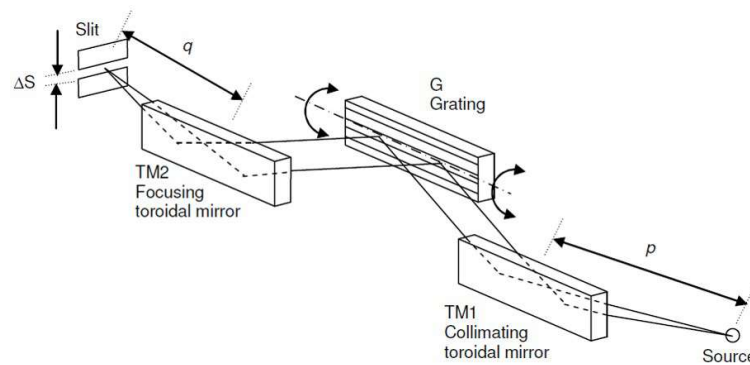
FIGURE 3.10: Drawing of the grating and toroidal mirrors and the optical path of EUV beam [55].
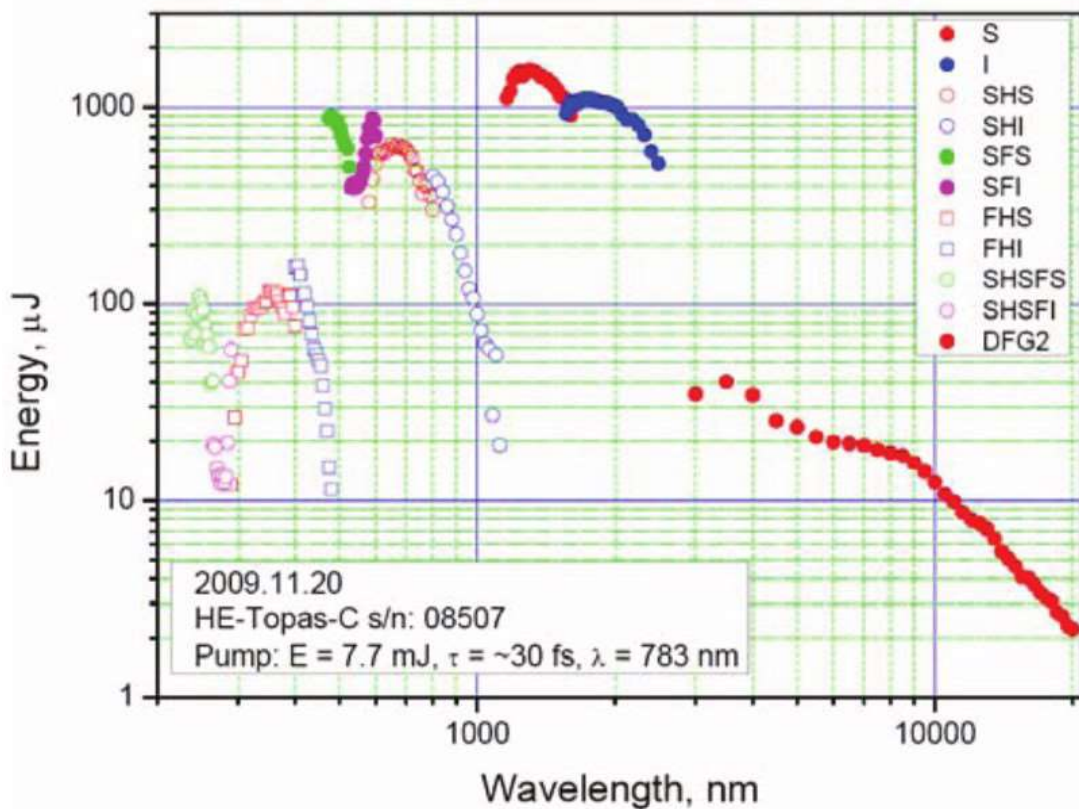
FIGURE 3.11: Tuning range and the energy of the HE-Topas pumped with 7.7 W [56]. S: Signal (1160-1550 nm), I:Idler(1550-2600 nm), SHS: Second harmonics of signal (580-800 nm), SHI: Second harmonics of Idler (1550-2600 nm), SFS: Sum frequency of signal and pump (475-533 nm), SFI: Sum frequency of Idler and pump (533-600 nm), FHS: Second harmonics of SHS (290-400 nm), FHI: Second harmonics of Idler (800-1160 nm), SHSFS: Second harmonics of SFS (237-261 nm), SHSFI: Second harmonics of SFI (261-300 nm), DFG: Differential signal generation of signal and idler (3-20 μm).

The SR pulses are generated in many different operation modes. In H-mode, there are 12 bunches and a bunch train in a period. Each bunch deliver a SR pulse with a duration of 50 ps, and the interval between them is 342 ns. All the bunches are useful if the scientific target covers the physics or chemistry happens in hundreds of ns to μs. In BL07LSU, a wide range of photon energies can be easily chosen

In 2016, a new fs pulse laser has been installed at BL07LSU, such that the pump-probe TRXPS can be carried out with high repetition rate about 208 kHz. This advantage improves the data statistic and save the data acquisition time. In a test, the SPV relaxation of Si $2p$ on a clean Si(111)-(7 × 7) was measured by two different repetition rate in Fig. 3.14. All the pump-on Si $2p$ curves in Fig. 3.14(a) measured with 208 kHz repetition rate took only 10 minutes while those in Fig. 3.14(b) with 1 kHz repetition rate took 30 minutes to get such scattered results. However the laser source with high repetition rate has less power density than the previous one. Table 3.2 shows the basic data of all the pump laser sources.

Figure 3.12 shows the timing control circuit and Fig. 3.13 shows the instrument setting from synchrotron ring, beamline, to the end station. The timing control was originated from a sinusoidal wave of 508.58 MHz signal delivered from a master oscillator, which regulates the RF cavity of the SPring-8 storage ring. After receiving the sin wave signal, the delay generators will generate different time delays by in-phase quadrature (IQ) modulators, transform the sine waves into square waves, and then send the square signals to the pump laser system and TOF analyzer trigger circuit separately (see Fig. 3.12).

Time-of-flight analyzer caters to the Spring-8 bunch mode. TOF analyzer has a different trajectory and different transformation function between kinetic energy and angle.

The kinetic energy is determined by:

$$E_{\text{kin}} = \frac{1}{2}m\left(\frac{d}{t}\right)^2, \tag{3.21}$$

where m is the electron mass, d is the distance from the sample to detector, and t is the flight time. TOF analyzer is a slitless analyzer, the energy resolution is determined by the time duration of the photon source, spatial resolution of the electron trajectory, and the time resolution of the delay line detector (DLD). The energy resolution can be
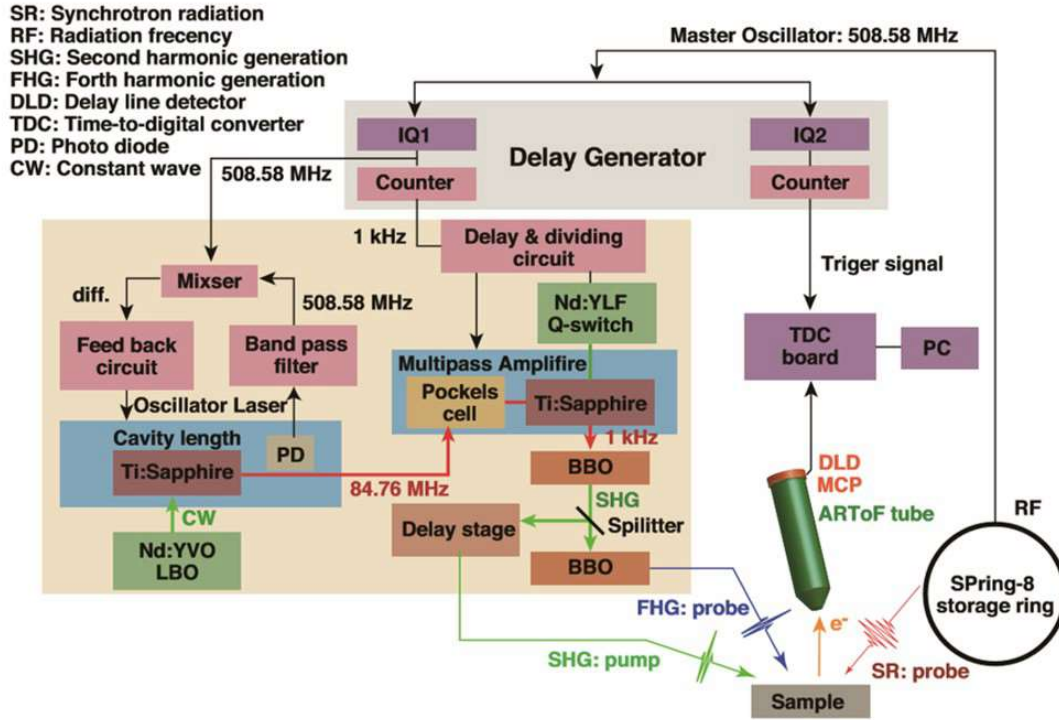
FIGURE 3.12: Electric circuit of TRXPS system [57].

expressed as:

$$\Delta E_{\text{kin}} = \sqrt{\frac{8E_{\text{kin}}^3}{m} \frac{\Delta t}{d}}, \qquad (3.22)$$

where Δt is the total time resolution. In ARTOF 10k analyzer, the lens system has been used to improve the electron trajectory, and a concept called as energy window is used like pass energy in fix mode of the conventional hemispherical analyzer. In this study, the energy window was set up at 5%, which gives an energy resolution of 30 to 100 meV when E_{kin} is about 100 to 300 eV [58].

The spatial overlap between pump and probe beam is checked by a phosphorus plate which is above the sample holder. The spot size of pump beam and probe beam is about 300 μm$\times$300 μm and 55 μm$\times$7 μm [59] respectively, thus almost all the measured area is covered by pump beam. For the temporal overlap between pump and probe, a photon diode near the sample holder is used to reach the temporal overlap below 0.1 ns. After that, a final fine tuning of the delay time will be considered by the SPV relaxation of a referenced surface, Si(111)-(7$\times$7).
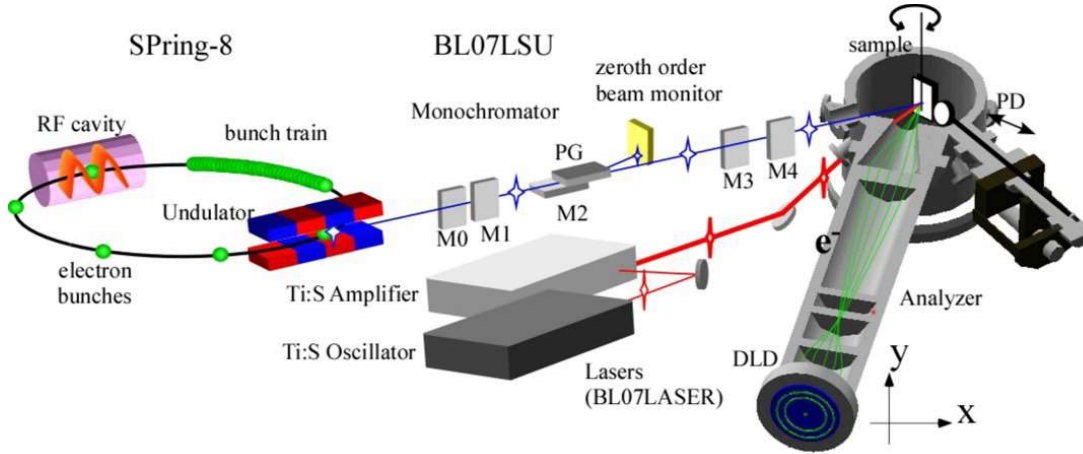
FIGURE 3.13: Schematic diagram of TRXPS system [57].
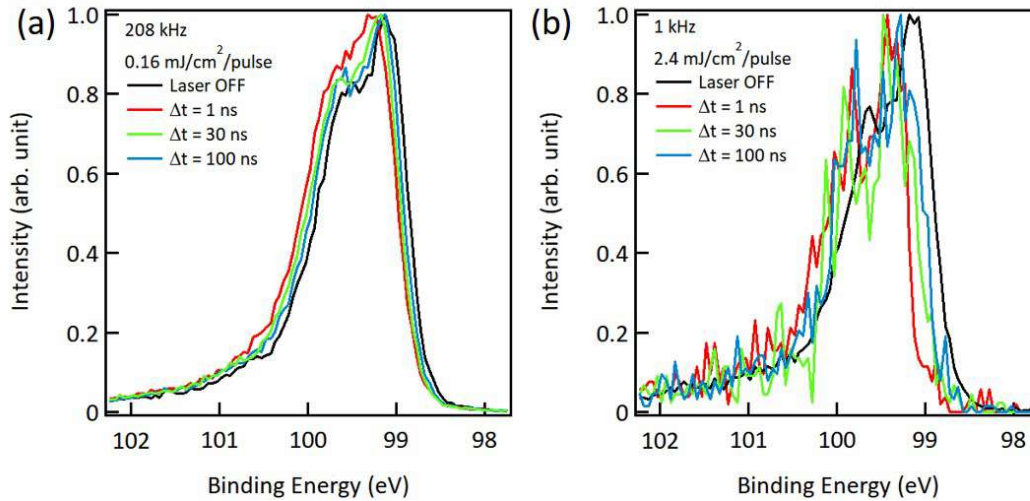
FIGURE 3.14: SPV relaxation at Si(111)-(7×7) surface measured with different repetition rate. (a) Si 2p core level spectrum measured by $h\nu = 253$ eV at the delay time $\Delta t = 1$, 30, and 300 ns. The wavelength, fluence of pump laser is 800 nm and 0.16 mJ/cm^2/pulse. The repetition rate of pump laser and the TOF analyzer is 208 kHz. The average data acquisition time for each data is about 10 min. (b)Si 2p core level spectrum measured by $h\nu = 253$ eV at the delay time $\Delta t = 1$, 30, and 300 ns. The wavelength and the fluence of pump laser are 800 nm and 2.4 mJ/cm^2/pulse, respectively. The repetition rate of pump laser and the TOF analyzer is 1 kHz. The average data acquisition time for each data is about 30 min. Static Si 2p spectrum (black curves labeled as Laser OFF in (a) and (b)) were measured with the repetition rate of 208 kHz for 10 min.

TABLE 3.2: Basic properties of all the pump laser sources at BL07LSU of SPring-8.

Repetition Rate	Pulse duration	Pump wavelength	Fluence (Max.)
1 kHz	35 fs	800 nm	10^3 mJ/cm^2/pulse
1 kHz	35 fs	400 nm	10^3 mJ/cm^2/pulse
208 kHz	60 fs	800 nm	2 mJ/cm^2/pulse
208 kHz	60 fs	400 nm	2 mJ/cm^2/pulse

Chapter 4

Femtosecond to picosecond transient effects in WSe$_2$ observed by pump-probe angle-resolved photoemission spectroscopy

Time-dependent responses of materials to an ultrashort optical pulse carry valuable information about the electronic and lattice dynamics; this research area has seen a rapid expansion centered on technologically promising materials such as graphene [60, 61], transition metal dichalcogenides [16] and topological insulators [31, 62]. We report herein a time-resolved angle-resolved photoemission spectroscopy (TRARPES) study of WSe$_2$, a layered semiconductor of interest for valley electronics. The results for below-gap optical pumping reveal energy-gain and -loss Floquet replica valence bands that appear instantaneously in concert with the pump pulse. Energy shift, broadening, complex intensity variation, and oscillation at twice the phonon frequency for the valence bands are observed at time scales ranging from the femtosecond to the picosecond and beyond. The underlying physics is rich, including ponderomotive interaction, dressing of the electronic states, creation of coherent phonon pairs, and diffusion of charge carriers: effects operating at vastly different time domains. Optical signal processing holds the key to developing ultrafast electronics. A fundamental question is how a material responds and relaxes as a function of time after a delta

excitation by an optical pulse. TRARPES is the most direct method of tracking the evolution of the electronic band structure, which also encodes the response of the lattice through electron-lattice or electron-phonon coupling. Our study focuses on the short-time behavior of optical excitation of WSe$_2$, which is a member of a vast family of transition metal dichalcogenides (TMDCs), many of which exhibit novel properties [10] that have galvanized the attention and interest of the condensed matter physics community [10, 20, 63].

4.1   Overview

Due to the rapid development of high power pulsed laser and ultrafast time duration in femtosecond regime, many exotic non-equilibrium phenomena that occurred in the condensed matter under strong light field are traceable recently. Floquet theory, a fundamental theorem for optics is applied to condensed matter and generalized as Floquet-Bloch theory. Floquet-Bloch state is actually an analog of photon dressed state in gas molecules, which has been intensively studied since 1970s [30]. Besides, Floquet-Bloch theory is also an important theory for High-harmonic generation (HHG) in periodic crystals. The study is helpful for utilizing semiconductors as a media to generate HH generation. Recently people pay attention on the symmetry breaking and phase transition induced by this external field on condensed matter. The introduction of photon field, breaks the time translation symmetry, make periodic bands in energy domain. Such a manipulation of band structure could generate many exotic phenomena, such as the chiral edge state in monolayer TMDC [15], Floquet topological insulator induced from a trivial insulator [62]. Many intriguing concepts are only mentioned in theoretical works, only few experimental works authenticated the existence of Floquet-Bloch states. One of the specific characters is that the intensity of Floquet-Bloch state may have a dramatic change on the dispersion shape or energy position by the coupling between orbitals and polarizations [64]. In brief, Floquet-Bloch state is dominated by the intrinsic optical properties of the materials. In this work, we measured the Floquet-Bloch state of bulk WSe$_2$ by TRARPES. A further study of $E + \hbar\omega$ and $E - \hbar\omega$ Floquet-Bloch state is carried. 2H-WSe$_2$ is one of the semiconductors in the class of TMDCs. Each unit cell contains two sandwich layers which only couples to each other by a weak Van der Waals force (see Fig. 4.1(a)). Tungsten atoms arrange in trigonal arrays with six nearest neighbors of Se from upper and lower layers. The electronic structure is shown in Fig. 4.1(c) for the core level electrons and in Fig. 4.1(d) for the valence band structure. WSe$_2$ has an indirect band gap about 1.3 eV

from Γ to T and a direct band gap about 1.63 eV at K (see Fig. 4.1(d))[65] . At K point, about 0.5 eV [11] energy splitting of VB1 and VB2 (marked in Fig. 4.1(d)) are explained by the Dresselhaus spin-orbit coupling term [19]. Though, bulk 2H-WSe$_2$ is an inversion-symmetric semiconductor which should be spin doubly degenerate, the strong spin polarization and the spin texture of the two valence bands at K point have been observed [11]. This spin splitting is similar to the one predicted to happen on the single layer TMDC [25]. The observation of spin splitting at bulk WSe$_2$ can be contributed by the symmetry breaking of the surface itself and the surface sensitivity of ARPES. By using an ultraviolet (UV) light source, the photoelectrons with the kinetic energy of several tens eV have a mean free path less than 1 nm, which means most of the obtained photoelectrons signal are from the 1st to 2nd sandwich layers of TMDC. This technique makes a substantial symmetry breaking on the whole system. Similarly, the circular polarized optical selection rules on valleys, which was predicted to occur at monolayer TMDCs [26], has been observed in TRARPES experiment by many groups recently [12, 66]. Above experiments indicate the identity between the surface of TMDCs and monolayer TMDCs.

TRARPES is the unique tool to show the straightforward evidence of Floquet-Bloch state which only appear within the pump and probe duration. In TRARPES, another effect, llaser-assisted photoemission effect (LAPE) [67, 68], also contributes the similar photon-dressed state simultaneously. The difference between LAPE and Floquet-Bloch state is that the LAPE is the photon-dressed final state while Floquet-Bloch state is the photon-dressed initial state. The intensity of photon-dressed final state is not related to materials electronic properties. It only depends on the angle between the momentum of the free photoelectrons and the direction of electric field of the pump pulses.

Consider a single electron time-dependent Schordinger equation with a laser field, the temporal evolution of the wave function can be written as [69]

$$\psi(t) = \psi(0) \sum_{n,l=-\infty}^{\infty} \exp\left[-\frac{i}{\hbar}\left(E + n\hbar\omega + 2l\hbar\omega + \frac{e^2 A^2}{4m} \right) t \right] \times J_n(\frac{e\mathbf{P}\cdot\mathbf{A}}{m\hbar\omega})) \times J_l(\frac{e^2 A^2}{2m\hbar\omega})$$

(4.1)

The time evolution of wave function ψ is expanded by using the Jacobi-Anger expansion. where $\hbar$, $\mathbf{P}$, m, $\mathbf{A}$, n, m are the plank constant, momentum operator, electron mass, vector potential, the index of replica band and the index of double frequency term. $J_n(e\mathbf{P}\cdot\mathbf{A}/m\hbar\omega)$ and $J_l(e^2\mathbf{A}^2/2m\hbar\omega)$ is the nth and lth of the first kind of Bessel function For the first analysis, the contribution from $2m\hbar\omega$ which has a rather small coefficient of $J_l(e^2\mathbf{A}^2/16m\hbar\omega)$ may be negligible because the order is $1/4(e|\mathbf{A}|/2|\mathbf{P}|)^4$
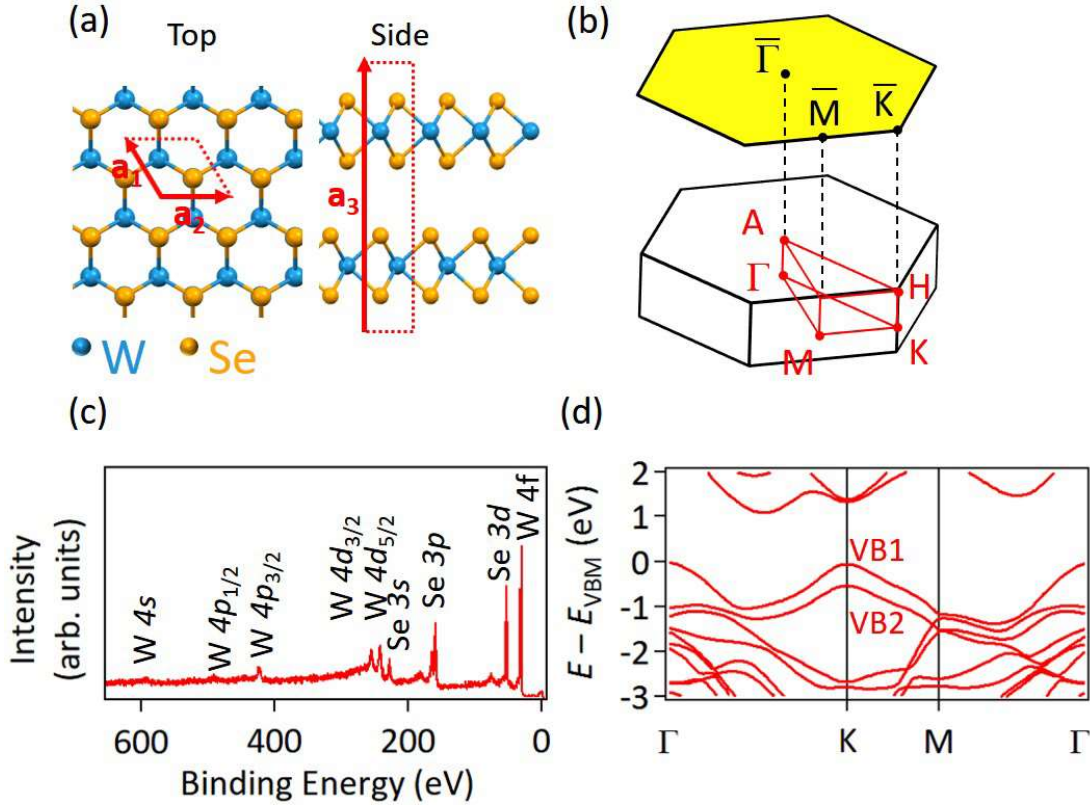
FIGURE 4.1: (a) Top and side views of the atomic structure of 2H-WSe$_2$.
(b) First Brillouin zone and its planar projection. (c) X-ray photoemission
spectroscopy data taken from a cleaved WSe$_2$ crystal using 1200-eV photons.
(d) Bulk band structure obtained by DFT calculations [11].

times smaller than $J_n(e\mathbf{P} \cdot \mathbf{A}/m\hbar\omega)$ in this work. Then the energy of nth replica band
is about $E + n\hbar\omega + (e^2\mathbf{A}^2)/4m$. The first term is the original energy of the bands, the
second term is the main energy change of Floquet-Bloch state from original band. The
third term is related to the ponderomotive energy shift.

In our experiment, the pump laser photon energy, 1.55 eV, is below the direct band
gap, and optical absorption by indirect excitation is weak.

4.2   Experimental Results

TRAPES measurements were performed using the system "4-Gouki" at the Institute
of Solid State Physics of the University of Tokyo [70]. Pump pulses were produced
using a 1-kHz Ti:Sapphire laser amplifier system with an output wavelength of 800
nm and a pulse width of 32 fs. The second-harmonic output of the same laser was

focused into an argon gas cell to yield the 9th HHG at 28 eV as the probe beam. The time resolution was about 84 fs as determined from the temporal response of a graphite reference sample. The size of the pump beam spot was 670 μm. A WSe$_2$ crystal purchased from HQ Graphene Co. was cleaved under ultrahigh vacuum to expose a fresh surface for the TRARPES measurements. All data were taken with the sample maintained at 40 K achieved by feedback-controlled liquid helium cooling. Initial sample characterization was performed at the X-ray Laboratory, the Institute for Solid State Physics, the University of Tokyo. X-ray photoelectron spectroscopy measurements (Fig. 4.1(c)) were carried out using synchrotron radiation at beamline 13B of the Photon Factory, High Energy Accelerator Research Organization (KEK).

Using a probe beam of 84-fs pulses of 28-eV photons at 1-kHz rate, a spectrum near the Fermi level obtained without application of the pump pulses (Fig. 4.2(a)) shows VB1 and VB2. Similar band structure is also detected with a He discharge lamp or a synchrotron beam as the light source. The Fermi level of the sample is very close to the conduction band minimum, implying a n-type band alignment at the sample surface. With the pump pulses turned on, the spectra at time delays of -500, 0, and 500 fs (Figs. 4.2(b)-(d)) reveal an approximately $+0.5$ eV shift of the bands toward the Fermi level. The pump fluence is 1.68 mJ/cm^2/pulse. Space charge effect has been ruled out by carefully reducing the probe beam intensity. Further investigation confirms that the shift is independent of the pump-probe delay times over a wide range. The shift can be attributed to a surface photovoltage effect [6]; charge carriers created by pumping diffuse to flatten out the band bending near the surface, giving rise to a built-in voltage that shifts the bands. The recombination or relaxation time for the carriers is much longer than 1 ms. With the pump running at 1 kHz, the surface photovoltage reaches a steady state value as observed in the experiment.

Additional spectral features are evident when the ARPES maps at delay times Δt = 0 and 500 fs are subtracted by the ARPES map at $\Delta t = -500$ fs. The difference maps should highlight the effects of pumping at the very short time scale. The results, with red and blue colors indicating positive and negative differences, show replicas of VB1 and VB2 (red bands) at 1.55 eV above the original bands for $\Delta t = 0$ (Fig. 4.2(e)) but not for $\Delta t = 500$ fs (Fig. 4.2(f)). The replica bands can also be seen in the original data (Fig. 4.2(c)). Additional time-resolved data (Fig. 4.3(c)) indicates that the replica bands are instantaneously present during the pump pulse duration only. The timezero is defined as the peak position extracted by fitting the temporal signal with a Gaussian function. The best FWHM is about 80 fs (as shown in Fig 4.3 (d)), which implies the total temporal resolution of the system. Similar replica bands

5年以内に雑誌等で刊行予定のため非公開

5年以内に雑誌等で刊行予定のため非公開

5年以内に雑誌等で刊行予定のため非公開

5年以内に雑誌等で刊行予定のため非公開

5年以内に雑誌等で刊行予定のため非公開

5年以内に雑誌等で刊行予定のため非公開

5年以内に雑誌等で刊行予定のため非公開

5年以内に雑誌等で刊行予定のため非公開

4.5　Conclusion

The results from our TRARPES study reveal a rich dynamic behavior of WSe$_2$. A number of fundamental processes are at play. At the shortest time scale, the system responds essentially instantaneously to the pump pulse via electronic state dressing by the Floquet process and via a ponderomotive interaction. Such dressing for bulk states (other than surface states), predicted to occur under optimal experimental conditions [76], is seen here for the first time. Within the first several ps after the pump, the system responds in a complex manner to coherent phonon-pair creation and decay. At times up to milliseconds and beyond, diffusing charge carriers give rise to a surface photovoltage. The comprehensive characterization from this study of the time-dependent behavior over multiple time scales in a prototypical TMDC provides a firm foundation for advancing optoelectronic technology and ultrafast electronics based on these and related materials.

5年以内に雑誌等で刊行予定のため非公開

Chapter 5

Ultrafast free carrier dynamics in bulk to monolayer WSe$_2$

Optical excitation of monolayer (ML) WSe$_2$ by above band gap pumping is experimentally studied for the first time by time-resolved and angle-resolved photoemission spectroscopy (TRARPES). In bulk sample, circular dichroism of conduction band at different K valleys has been observed. Electrons are excited directly from the valence band maximum to the conduction band at a K valley. Carriers at K valley decay very fast within 50 fs and scattered to T point, which is the global conduction band minimum. The change in the valence band represents the hole lifetime, which is longer than 1 ps. In ML sample, electron-hole pairs were generated at K valleys by using the 730-nm or 585-nm pump pulses respectively. Excited electrons at CBM show two lifetimes, which are about several tens fs and several ps respectively. The carrier lifetime at K valleys in ML WSe$_2$ is much longer than the one in bulk WSe$_2$ due to its direct band gap nature. We also observed an energy shift of the VBs in ML WSe$_2$ toward Fermi level happens but this shift does not pass through the sublayer, bilayer graphene (BLG). BLG has been also excited and generate free carriers at Dirac cones (DCs) like the usual BLG without any adlayers. The dynamical data is helpful for understanding the ultrafast phenomena on a typical van der Waals heterojunction device.

5.1   Overview

Two-dimensional (2D) TMDCs have been successfully produced and studied in the past decades. It has been predicted to possess remarkable mechanical, electronic and optical properties. Possessing the direct band gap in infrared to visible range, 2D TMDCs is more useful than the gapless graphene for the application to industry. Besides, the coupling between spin and valleys provides extra degree of freedom to the design of the spin- and valley-controlled devices in the future.

Coupled spin and Valleytronics in 2D TMDCs is a concept mentioned by Xiao *et al.* in 2012 [26]. Due to the inversion symmetry breaking, the VB and CB at K valleys are separated into 2 sets, each of them posses spin up/down valence bands. The decoupling of valleys makes the valley itself can be treated as an extra channel from the spin. Carriers at different valleys are far away from each other, which can largely decrease the sccatering and keep signal for a longer time. Thus valley-controlled devices are even more promising than spin devices. The band structure of 2D TMDCs have been extensively browsed by ARPES [77]. The basic optical properties of 2D TMDCs are widely studied by optical absorption spectroscopy (OAS), photoluminensence [78, 79].

The ultrafast response of ML TMDCs was intensively studied recently. In optical measurement, the optical absorption and photoluminenscence experiments specified the basic properties of ML to multi-layers of TMDCs, such as the size of optical band gap, peak positions of A(B) excitons, circular helicity, etc. In time-resolved optical measurement, Sie *et al.* [15] found the AC stark shift at time zero after strong circular polarized pumping. This shift implies the existence of Floquet-Bloch (Photon-dressed) states and the topological edge states. Jeong *et al.* [72] observed the coherent lattice vibration in ML and multilayers TMDCs, which implies the A$_{1g}$ mode vibration. However, the correspondence between the optical measurement to the direct evidence from electronic structure is still lacking. There is little published works that were done by supervising the temporal change of the electronic structure in optical pumping condition. Thus the detailed examination for the carrier dynamics of ML TMDCs is highly called for.

In the present study, we performed TRARPES experiment on the bulk WSe$_2$ and ML WSe$_2$/BLG/SiC(0001) surface with different pumping energies which are respectively 1.7 eV and 2.1 eV. Both of them are above band gap.

5.2   Experimental setup and Sample treatment

The growth of WSe$_2$ thin film and *in situ* ARPES measurements were performed at Advanced Light Source, Lawrence Berkeley National Laboratory. The WSe$_2$/BLG heterostructure was synthesized on a 6H-SiC(0001) wafer in an ultra-high vacuum (UHV) environment (with base pressure about 1×10^{-10} torr). BLG is an ideal platform for epitaxial growth of layered materials with honeycomb lattices, such as Bi$_2$Se$_3$, TMDCs, due to its honeycomb structure and the inert van der Waals surface. Because the lattice ratio between BLG and WSe$_2$ is about 3:4, it is easier to form a single-crystalline thin film with a large superstructure. To form an uniform BLG substrate, a 6H-SiC(0001) wafer was firstly degassed at 680°C in the ultrahigh vacuum (UHV) chamber for several hours, and then followed by 80 cycles of flash-annealing to 1300°C [80]. The Si dangling bonds at the SiC surface were saturated by a carbon buffer layer with a $(6\sqrt{3} \times 6\sqrt{3})$R30° periodicity under the graphene layer. WSe$_2$ was then grown on top of the BLG by MBE growth with an electron-beam evaporator and a standard Knudsen cell. High purity W and Se were prepared in the e-beam evaporator separately, and the flux ratio was controlled to be 1:30. The extra mount of Se is necessary to decrease the Se vacancy and the W cluster nucleation. The BLG substrate was kept at about 400°C. The film thickness was monitored by the *in situ* RHEED pattern. Figure 5.1 (a) is the photon of ML WSe$_2$/BLG/SiC(0001) sample with sample holder. During the evaporation, the sharp 1×1 spot showed in RHEED screen (see Fig. 5.1(c)). Figures 5.1(b) and (d) show the ARPES map along the $\overline{\Gamma} - \overline{\text{K}}$ and the UPS spectrum, respectively. In Fig 5.1(b), the valence band splitting at $\overline{\text{K}}$ valley is easily to be seen. A linear dispersion showed up from 1.2 Å^{-1} to larger k space is one part of the Dirac cone contributed from BLG below the ML WSe$_2$. Figure 5.1(d) shows the sharp W $4f$ and Se $3d$ peaks, indicating the good growth condition of film.

During the transportation, the sample surface was protected by Se capping layer. After the sample mounting into the TRARPES chamber, the sample was further annealed to 400°C to remove the Se capping layer, exposed the pristine WSe$_2$. For the bulk WSe$_2$, the treatment is exactly the same as described in Chapter 4.

In TRARPES experiment, the pump and probe pulses were generated by a 1 kHz Ti:sapphire amplified laser system with a wavelength of 785 nm. The pulse duration and the energy per pulse are 30 fs and 12 mJ, respectively. The band structure of ML WSe$_2$ and graphene along the $\overline{\Gamma} - \overline{\text{K}}$ direction was measured using the 15th high harmonic probe pulses ($h\nu$ = 25 eV). The HHG probe pulses were generated by focusing part of the laser energy to a gas cell filled with Ar gas. The rest laser energy
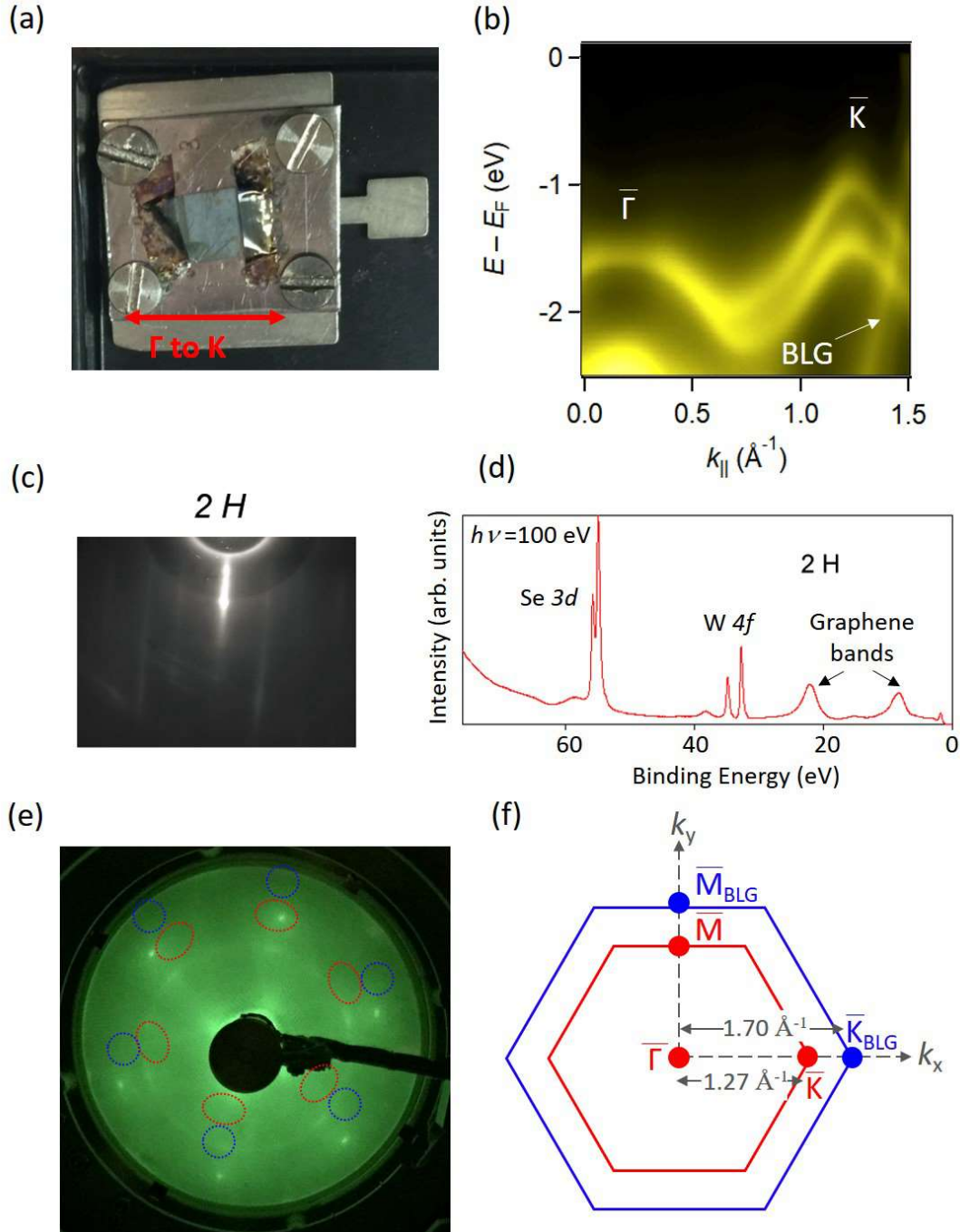
FIGURE 5.1: (a) ML WSe$_2$/BLG/SiC(0001) sample and the sample holder. (b) ARPES map of 2H phase ML WSe$_2$/BLG/SiC(0001). (c) RHEED pattern of 1×1 ML WSe$_2$. (d) UPS scan of ML WSe$_2$/BLG/SiC(0001) (e) LEED pattern of ML WSe$_2$/BLG/SiC(0001) after annealing of the Se capping layers. (f) Surface Brillouin Zone of ML WSe$_2$ and BLG.

was bypassed to an optical parametric amplifier (OPA, HE-Topas from coherent co.) followed by a frequency mixing stage. The OPA system provides a broad wavelength to be selected as pump pulses. In this experiment, the SHS (second harmonics of signal beam) range (580-800 nm) has been used. Further details are described in Chapter 3. The wavelength of pump was selected as 730 nm (1.7 eV) and 585 nm (2.1 eV). The fluence of the pump pulse was kept around 0.8~1 mJ/cm^2/pulse. Both of the probe and pump beams were polarized as P-polarization. To reduce the space-charge effect from probe beam, the photon flux and its beam size were tuned by adjusting the size of end slit and the bending strength of the focusing toroidal mirror. The energy, angular, and time resolution are 400 meV, 0.3°, and 50 fs, respectively.

For the data acquisition, few-delay-point mode or many-delay-point mode were used to cater different requirement. Few-delay-point mode accumulates ARPES data with only two delay points data and scan for several hours to get clear contrast in differential ARPES spectra with better signal-to-noise ratio. Many-delay-point mode accumulates ARPES data with much more delay points over 40-50 points to get detailed temporal response of the sample.

5.3   Analysis

In this section, we present the model and fitting functions for characterizing the rise time and decay time of the carrier dynamics at a specific electronic state. The total temporal response is a convolution between the original response from the material and the instrumental transfer function. The instrumental function is a Gaussian function with a limited width, which is determined by the time resolution of the system. In this system, the time resolution is about 50 fs [55]. For the original response from a material, there are many phenomenological models and fitting functions. In this study, we consider the multi-exponential functions that had been used in the dynamics of TMDC recently [14, 66]:

$$I(t) = \begin{cases} I_0 & , t < t_0 \\ I_1 - A \times e^{-\frac{t-t_0}{\tau_{rise}}} + \sum_{i=1}^{N} A_i \times e^{-\frac{t-t_0}{\tau_i}} & , t \geq t_0. \end{cases} \tag{5.1}$$

I_0 corresponds to the overall background in the photoemission data and I_1 represents the residual electron population which may possess a longer decay time beyond the measured range. τ_{rise} and τ_i are the time constants for the generation and attenuation
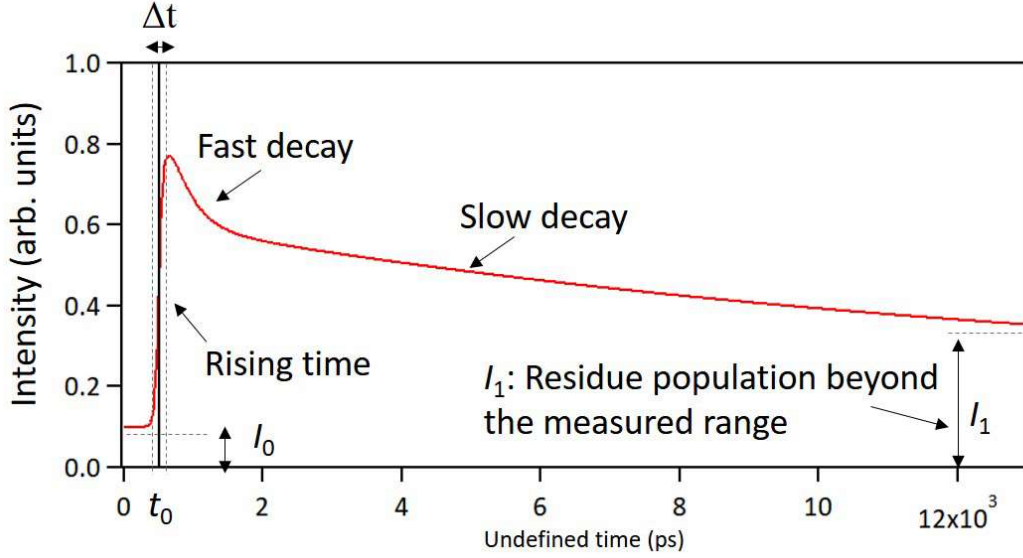
FIGURE 5.2: Example curve with information. I_0 represents the averaged
background in the whole measurement. The excitation takes a finite rising time
to reach to the maximum from I_0. After the carrier generation, many different
scattering processes set in. From the slope change, the time component of fast
or slow decay can be roughly observed. I_1 accounts for the rest population
that still exist in this time domain.

of excited carriers. In our experiment, $N = 1$, or 2 to capture the short and long
lifetimes. The scale factors, A and all the A_i, are positive.

The instrumental function is a Gaussian function

$$G(t) = \frac{1}{\sqrt{2\pi}\sigma} \exp(-\frac{t^2}{2\sigma^2}), \tag{5.2}$$

where σ is the standard deviation, and the FWHM is $2\sqrt{\ln 2}\sigma$. The convolution of $I(t)$
and $G(t)$ is:

$$\begin{aligned}
\int_{-\infty}^{\infty} I(t') \times G(t-t')dt' = &\int_{-\infty}^{t_0} I_0 \times \frac{1}{\sqrt{2\pi}\sigma} \exp\left(-\frac{(t-t')^2}{2\sigma^2}\right) dt' \\
&+ \int_{t_0}^{\infty} I_1 \times \frac{1}{\sqrt{2\pi}\sigma} \exp\left(-\frac{(t-t')^2}{2\sigma^2}\right) dt' \\
&- \int_{t_0}^{\infty} A \exp\left(-\frac{t'-t_0}{\tau_{rise}}\right) \times \frac{1}{\sqrt{2\pi}\sigma} \exp\left(-\frac{(t-t')^2}{2\sigma^2}\right) dt' \\
&+ \sum_{i=1}^{N} \int_{t_0}^{\infty} A_i \exp\left(-\frac{t'-t_0}{\tau_i}\right) \times \frac{1}{\sqrt{2\pi}\sigma} \exp\left(-\frac{(t-t')^2}{2\sigma^2}\right) dt'.
\end{aligned}$$

$$\tag{5.3}$$

In above equation, all the improper integrals can be replaced by complementary error function as below:

$$\int_{-\infty}^{\infty} I(t') \times G(t - t')dt' = \frac{I_0}{2}erfc(\frac{t - t_0}{\sqrt{2}\sigma}) + \frac{I_1}{2}erfc(\frac{t_0 - t}{\sqrt{2}\sigma})$$
$$- \frac{A}{2} \times \exp\left(-\frac{t - (t_0 + \frac{\sigma^2}{\tau_{rise}})}{\tau_{rise}}\right) erfc(\frac{-(t - (t_0 + \frac{\sigma^2}{\tau_{rise}}))}{\sqrt{2}\sigma})$$
$$+ \sum_{i=1}^{N} \frac{A_i}{2}\exp\left(-\frac{t - (t_0 + \frac{\sigma^2}{\tau_i})}{\tau_i}\right) erfc(\frac{-(t - t_0 - \frac{\sigma^2}{\tau_i})}{\sqrt{2}\sigma}),$$

$$(5.4)$$

where $erfc(x)$ is the scaled complementary error function. $erfc(x)$ is defined by an integral: $\frac{2}{\sqrt{\pi}} \int_x^{\infty} e^{-t^2} dt$.

Figure 5.2 shows an example of the temporal trace of an excited state. The rising of the signal is not a step function as the model in Eq. (5.1) but smear in time domain due to the limit time resolution and its intrinsic response time. After the excitation, a fast decay may occur within few seconds. The fast decay usually comes from e-e scattering, many-body effect, etc. For example the supercollision in Graphene [81] is a defect-assisted three-body scattering mechanism. After the fast decay, the slow decay is usually related to electron-phonon scattering, which makes excited electronic state slowly migrate to lower energy level. After several tens of ps, the rest carriers will be governed by the SPV shift, thermionic emission, or drift and diffusion process.

5.4   Results and discussion

5年以内に雑誌等で刊行予定のため非公開

5年以内に雑誌等で刊行予定のため非公開

5年以内に雑誌等で刊行予定のため非公開

5年以内に雑誌等で刊行予定のため非公開

5年以内に雑誌等で刊行予定のため非公開

5年以内に雑誌等で刊行予定のため非公開

5年以内に雑誌等で刊行予定のため非公開

5.5　Conclusion

In summary, the time-resolved and angle-resolved PES experiment was carried out at the bulk and ML WSe$_2$ surface to capture the carrier dynamics from fs to ps range. At resonant pumping for bulk WSe$_2$, the direct optical transition at VBM demonstrated the circular dichroism at different K valleys by right-/left-handed circular polarized light. The signal at conduction band of K valley quickly decayed within 40 fs, which can be explained by the intervalley scattering from K to the global CBM, T point. In ML WSe$_2$ sample, excited carriers at K valley indicate a fast decay (about 40 fs) and a slow decay (more than 3 ps) which is far from our measured range. In a very short time,

5年以内に雑誌等で刊行予定のため非公開

5年以内に雑誌等で刊行予定のため非公開

an energy shift toward Fermi level is observed in the VBs of ML WSe$_2$ but this shift does not pass through the sublayer, bilayer graphene. According to many evidences, space charge effect and surface photovoltage effect can be ruled out, this shift is likely caused by the gap renormalization.

Chapter 6

Controlling the surface photovoltage relaxation on WSe$_2$, K/WSe$_2$, and C$_{60}$/WSe$_2$

The surface photovoltage effect has been one of the most fundamental optical responses of a matter that leads to development of various opto-electronic devices such as solar-cells or photo-detectors. On surfaces of the transition metal dichalcogenides crystal, we extensively studied variation of electronic states after the surface modification by photoemission band mapping, followed by examination of the generation and the relaxation of SPV by time-resolved photoemission spectroscopy. Amount of SPV at a surface of the p-type WSe$_2$ crystal was similar to the surface covered with a layer of the donor-type (K) but reduced with the acceptor-type (C$_{60}$). The SPV relaxation time becomes short by formation of the heterojunctions, K/WSe$_2$ and C$_{60}$/WSe$_2$. It is likely that the electronic states of the overlayer become the new recombination centers of photo-excited carriers.

6.1 Overview

Crystals of the transition metal dichalcogenides (TMDCs), such as WSe$_2$ and MoSe$_2$, are composed of two-dimensional layers that are bound with neighbors by the van der Waals interaction. Such a two-dimensional (2D) layered material has now classified as one of the van der Waals crystals that have recently attracted attentions in the device

applications. Concerning opto-electronic devices, such as solar cells, the most fundamental optical response is generation of photovoltage by the spatial separation of the photo-excited electrons and holes that are achieved at the surface or the interface region (surface photovoltage effect, SPV). The technical developments have highly required understandings and controls of electronic states and carrier dynamics at the TMDC surface or an interface in the TMDC heterojunction.

Tungsten diselenides, WSe$_2$, has been regarded as a promising material as a component in a solar cell due to its high optical coefficient from infrared rays to visible light. The material is composed of a periodic stack of the Se-W-Se trilayers in a 2H motif. Figure 6.1(a) shows a schematic drawing of the atomic structure along the stacking axis (001). The topmost atoms in the layer are Se atoms that are fully saturated with W atoms in the threefold coordinates. A crystal of WSe$_2$ has been found to make the SPV effect, however, it has not been examined in detail to find the critical factors in the opto-electronic performance. Moreover, a surface of WSe$_2$ has left the possible optimization by atom/molecule adsorptions. Thus, it has been highly called for to extensively study surface/interface electronic states, carrier dynamics and their relationships.

Photoelectron spectroscopy has been the powerful experimental analysis to directly probe electronic states in a matter. The time-resolved measurement further allows us to trace the temporal variation that reveals a whole picture in carrier dynamics. Since energy shifts of the valence electronic states by SPV can precisely be evaluated by those of the core-level states, the time-evolution have been studied by measurements of time-resolved x-ray photoemission spectroscopy (TRXPS). The technique has found to be sensitive to track differences on a surface by deposition of hetero-adsorbates down to monolayer coverage. In the present research, we made TRXPS experiments on a surface of WSe$_2$ to investigate carrier dynamics in the SPV effect. We also carried out the measurements after depositions of potassium (K) atoms and fullerene (C$_{60}$) molecules on a surface. With the photoemission band diagrams of the WSe$_2$, K/WSe$_2$, and C$_{60}$/WSe$_2$ surfaces, we systematically investigated variations of the 2D electronic states and the carrier dynamics at the regulated surfaces that become the fundamental references in developing the TMDC photovoltaics.

6.2   Experimental Setup

A single crystal of WSe_2 with the (001) orientation was purchased from HQ Graphene Co.. The crystallinity and the crystal axis were confirmed by the Laue method of X-ray diffraction. After the installation into an ultrahigh vacuum chamber, the surface is cleaned by exfoliation. The surface crystallinity was confirmed by a clear 1×1 pattern of low-energy electron diffraction (LEED). Deposition of potassium was made with a SAES dispenser, while the deposition of fullerene was performed with a K-cell evaporator. The adsorbates was deposited onto a surface of WSe_2 until the saturation coverage, 1 ML for K. For fullerene, the average coverage is about 0.8 ML for C_{60}, which guarantees most fullerene connected to the WSe_2 surface without piling up to two layers. The coverage was evaluated from the core-level spectra (see appendix A).

Photoemission band mappings were performed by angle-resolved photoemission spectroscopy using synchrotron radiation (SR) at beamline 21B of Taiwan Light Source (TLS), National Synchrotron Radiation Research Center (NSRRC). The spectra were recorded by a hemispherical electron energy analyzer (Scienta R4000) with energy resolution of 50 meV at $h\nu = 28$ and 42 eV. The Fermi energy in a spectrum was determined by the Fermi-level cutoff of a gold foil. TRXPS measurements were carried out at BL07LSU at SPring-8 by the pump-probe method [57]. The pump was a laser pulse of $h\nu = 1.55$ eV, generated by the amplified Ti:sapphire laser with the pulse duration of 60 fs and the pulse interval of 4.81 μs. The probe was a SR pulses of $h\nu = 253$ eV that were generated during the F-mode operations in the electron storage ring with the duration of 50 ps and the interval of 342 ns. TRXPS were obtained by a time-of-flight electron energy analyzer (VG Scienta ARTOF 10 k). The binding energy of the spectra was defined by energy position of the Au $4f_{7/2}$ peak of a gold foil. All the photoemission measurements were performed at room temperature. Space charge effect induced by synchrotron pulses was reduced by adjusting the photon flux and beam size until W4f peak position of WSe_2 sample will not shift with the photon flux.

6.3   Surface Electronic Structure

To trace variation of amount of the band-bending effect, core-level spectra of the WSe_2 surfaces were measured before and after deposition of K or C_{60}. Since energy positions of core-levels are energetically fixed relative to those of the valence bands, core-level spectra have been probed to examine the band-bending effect. Figure 6.2(a)
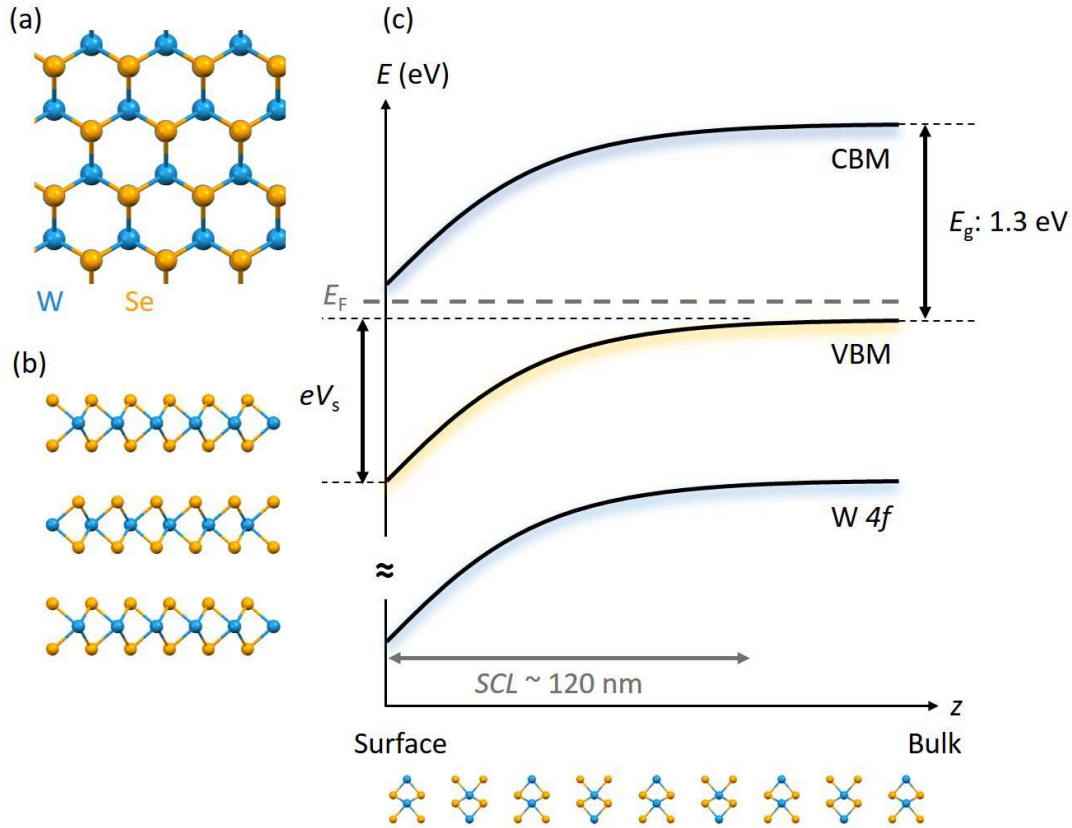
FIGURE 6.1: Atomic structure of WSe$_2$ viewed from (a) (001), and (b) (100).
(c) Band diagram at surface.

and (b) present the W $4f$ and Se $3d$ spectra that indicate apparent energy shift of 0.18
eV toward higher binding energy. As shown in Fig. 6.2(c), appearance of the K $3p$
peak confirms the K overlayer. Figures 6.2(d)-(f) are the results of the C$_{60}$ deposition.
The W and Se core-levels also indicate energy shift of 0.08 eV to the lower binding
energy, while the C $1s$ core-levels confirm the C$_{60}$ adsorbates. Since the samples were
prepared from the same wafer and photoemission spectroscopy probes bulk state near
the surface under the current experimental condition ($h\nu = 253$ eV), the energy shift
of the observed bulk band corresponds to variation of the band-bending effected by
adsorbates [46, 90, 91]. The results indicate the opposite roles of the two overlayers in
modifying bulk state near the surface region or the SCL. The overlayer of K enhances
the band-bending effect at a WSe$_2$ surface, while that of C$_{60}$ suppresses the effect.

To understand electronic structure at the surface region, Figs. 6.3(a)-(f) show pho-
toemission band diagrams of (a) the pristine WSe$_2$ surface, (b) the K-covered WSe$_2$
surface (K/WSe$_2$), and (c) the C$_{60}$-covered WSe$_2$ surface (C$_{60}$/WSe$_2$). In Fig. 6.3(a),
dispersion curves of the two bulk valence bands, labeled as VB1 and VB2, can be found
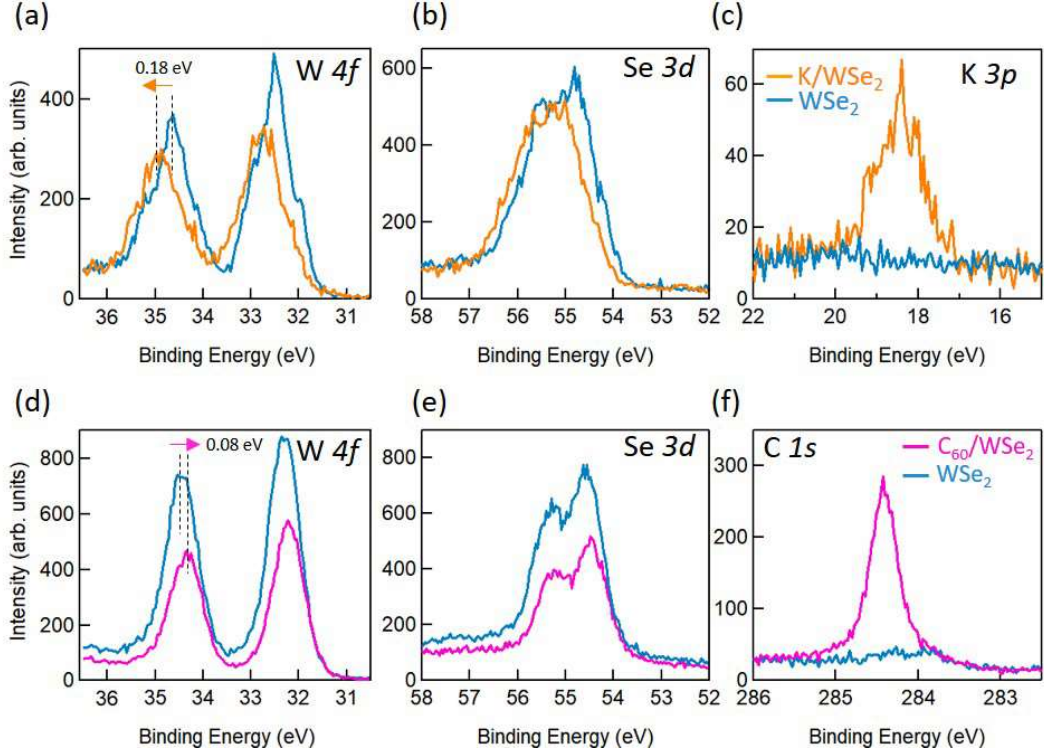
FIGURE 6.2: (a)(d)W $4f$, (b)(e) Se $3d$, (c) K $3p$, (f) C $1s$ core-level spectra of the pristine WSe$_2$ surface (blue) and the surfaces covered with K (orange) or C$_{60}$ (pink). The spectra were taken at room temperature at the photon energy of $h\nu = 253$ eV.

at K point at $E - E_F$, of -1.26 eV and -1.75 eV, respectively. In Fig. 6.3(a), VBM of the clean WSe$_2$ surface locates at $E - E_F = -1.26$ eV. Since the bulk band gap of WSe$_2$ is 1.3 eV, the Fermi level locates close to the conduction minimum and it can be regarded as n-type. On the other hand, VBM of the internal bulk, VBM$_{\text{bulk}}$, is evaluated to be 0.22 eV (p-type) for the current sample and, thus, amount of the band bending effect is V_s =1.04 eV that indicates the formation of the inversion-type space-charge layer or the natural p-n junction. By the K deposition, on the WSe$_2$ surface, the VB1 and VB2 band shift to higher binding energy of 0.18 eV, as evaluated from the results in Figs. 6.3(a), (b). This change can be confirmed in Fig. 6.2(a), (b) , showing the VBM position shifts toward the higher binding energy. On the other hand, by deposition of C$_{60}$, VBM moves toward the lower binding energy, as measured in Figs. 6.2(d)-(e). Such spectral features of VB1 and VB2 are also found in Fig. 6.3 though the overall spectral features appeared faintly for the C$_{60}$ overlayer.

These apparent observation of the band bending effect is in contrast to our expectation that a pure crystal of WSe$_2$ should keep the flat bulk-band condition or no

band-bending effect due to absence of the intrinsic surface state on the prefect van der Waals crystal surface [4, 43]. However, the previous ARPES researches have also revealed that a surface of the p-type WSe$_2$ wafer does not keep the bulk-band configuration of p-type near the surface. It has been discussed that the actual surface has various types of defects, such as atomic steps or dislocations, and also it can possibly be contaminated by residual gas in the UHV chamber [92]. Buck *et al.* [6] reported that these factors induce unexpectedly the large band-bending effect and the SCL width of WSe$_2$ extends to ∼120 nm. The WSe$_2$ SCL has now attracted interests to be functionalized as a carrier reservoir for photovoltaics.

Focusing on the photoemission band diagram of K/WSe$_2$ at the Fermi level (Fig. 6.3), one can find apparent spot at $k_{||} = 0.65$ Å^{-1} and a broad feature over the $k_{||}$ line. The former can be assigned to the CBM, located at $\overline{\text{T}}$, of the bulk WSe$_2$ crystal, while the latter is likely attributed to the K-derived metallic band. The electronic state can be regarded as a QWS in the overlayer and makes a parabolic dispersion near Brillouin zone center (Fig. 6.3 (e)). This is supported by the fact that a potassium atom has been known to make no intercalation between the WSe$_2$ layers [90], which was also confirmed by our measurement of linear increase of the K $3p$ spectral intensity (Fig. 6.2(c)) with respect to amount of the K deposition. The K overlayer behaves as electron donor to the WSe$_2$ layer.

In the case of the C$_{60}$/WSe$_2$ surface, one can find the highest occupied molecular orbital (HOMO) and the next highest occupied molecular orbital (NHOMO) of the fullerene at $E - E_{\text{F}} = -2.62$ eV and -4.06 eV, respectively, in the spectra (Fig. 6.3(f)). The LUMO position of the C$_{60}$ molecule is estimated to be around -1.34 eV from the reported gap between NHOMO and LUMO [93]. The spectral feature of LUMO can be confirmed, as shown in the inset of Fig. 6.3(f). While spectral overlaps of these molecular orbitals hinders photoemission signals from the WSe$_2$ valence bands, comparisons of the individual levels indicates that, at a surface, the LUMO level locates within the band-gap of WSe$_2$ and binding energy of HOMO is lower than VBM of WSe$_2$. It is likely the LUMO orbital that is responsible for the acceptor-type [91] character of the C$_{60}$ overlayer on WSe$_2$.

6.4   Carrier dynamics

Variation of the band-bending effect at the WSe$_2$ surfaces indicates possible generations of various types of the SPV effect that also allows us to examine carrier dynamics
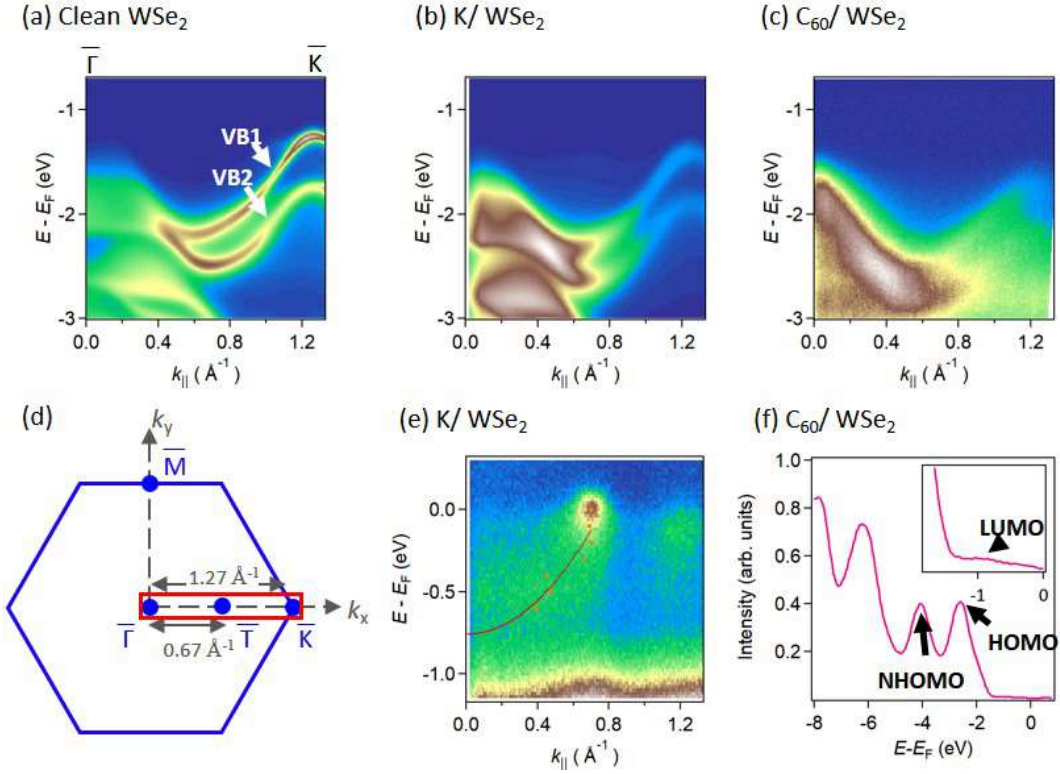
FIGURE 6.3: Photoemission band diagrams of surfaces of (a) WSe_2, (b) K/WSe_2, and (c) C_{60}/WSe_2 taken along the $\overline{\Gamma}$ - $\overline{K}$ axis at (a) $h\nu = 42$ eV, (b) $h\nu = 42$ eV, and (c) $h\nu = 28$ eV. (d) Measured $k_{\|}$ range in SBZ. (e) Selected region for K/WSe_2. (f) Angle-integrated spectra of C_{60}/WSe_2 taken at $h\nu = 28$ eV. In the figure, peaks assigned to the molecular orbitals are labeled.

from the relaxation. To trace the dynamical behavior on the WSe_2, K/WSe_2, and C_{60}/WSe_2 surfaces, we carried out the TRXPS measurements of the W $4f$ core-level by the pump-probe method. In the experiment, electron carriers are photo-excited by the ultrafast laser pulses of $h\nu = 1.55$ eV that is larger than the indirect band gap (1.3 eV) [22] and close to the exciton absorption peak (1.62 eV) [2]. Figure 6.4(a) shows energy shift of the core-level peaks by the SPV effect with respect to the pump energy. By the pump energy of 1 mJ/cm^2/pulse, photovoltage is evaluated to be about 0.15 V for K/WSe_2 and for WSe_2, while about 0.05 V for C_{60}/WSe_2 surfaces. The photovoltage has a tendency to be large for the large band-bending effect or the large surface potential (Fig. 6.1(c)). Concerning the relaxation of the SPV effect, the relaxation time was different between the three surfaces, indicating the different dynamical behaviors.
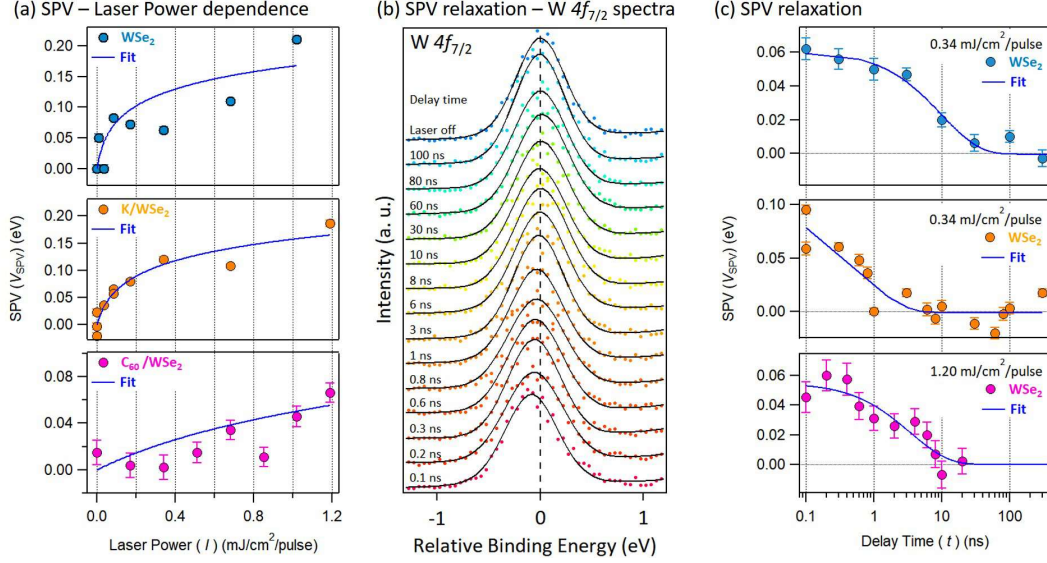
FIGURE 6.4: (a) Energy shifts in the W $4f$ core-level in spectra of WSe$_2$ (blue), K/WSe$_2$ (orange), and C$_{60}$/ WSe$_2$ (pink), as functions of the pumping laser power. The data were recorded at the delay time of 0.1 ns. The power-dependence of the individual surfaces is curve-fitted as blue curves by Eq. (6.1a). (b) A collection of time-resolved W $4f_{7/2}$ core-level spectra of the K/WSe$_2$ surface taken by pump ($h\nu = 1.55$ eV) and probe ($h\nu = 253$ eV) method. Pulse energy of the pump was 0.34 mJ/cm^2 per pulse. The spectra (circles) are fitted by Voigt functions (solid lines). (c) Temporal variations of the surface photovoltage (SPV) for WSe$_2$ (blue), K/WSe$_2$ (orange), and C$_{60}$/ WSe$_2$ (pink). Blue curves are the fitting results of the Eq. (6.1).

Conventionally, illumination power dependence and the temporal relaxation are phenomenologically described in terms of the following formula [42, 94]

$$V_{\text{SPV}}(I) = -\eta k_{\text{B}} T \ln\left(1 + \gamma \times I\right), \tag{6.1a}$$

$$V_{\text{SPV}}(t) = -\eta k_{\text{B}} T \ln\left[1 - \left\{1 - \exp\left(-\frac{V_{\text{SPV}}(0)}{\eta k_{\text{B}} T}\right)\right\} e^{-t/\tau_\infty}\right], \tag{6.1b}$$

where k_B, T, and $V_{\text{SPV}}(0)$ are the Boltzmann constant, sample temperature (300 K), and the SPV shift at $t \sim 0$ ns, respectively. I and t are the fluence of pump laser and the delay time between pump and probe pulses. Parameters, η, γ, and τ_∞, are the ideality factor, the efficiency of the optical excitation, and the relaxation time of SPV. Equations (6.1a) and (6.1b) are the so-called thermionic emission model that derived from the temporal change of potential barriers by transportation of the minority carriers. It is of note that Eqs. (6.1a) and (6.1b) contain the same parameter η. As shown in Fig. 6.4, the data points are fitted by Eqs. (6.1a) and (6.1b) fairly well.

The photo-induced energy shift is described in terms of SPV and the relaxation likely follows the thermionic emission model.

Table 6.1 shows a summary of the fitted parameters for the pristine WSe$_2$, K/WSe$_2$, and C$_{60}$/WSe$_2$ surfaces. The pre-factor of η was around 2 for the three surfaces. The quantity η is related to a ratio of thermal cross-section for electrons and holes, and it typically ranges between 0.5 and 2, indicating appropriateness of the models [95]. The relaxation time, τ_∞, of WSe$_2$ was longer than those of K/WSe$_2$ and C$_{60}$/WSe$_2$, meaning suppression of the relaxation time by the overlayers.

Electronic states at surfaces have various roles in controlling performance of photo-voltaic materials. One is to change the amount of the band-bending effect that directly link to spatial separation of the photo-excited carriers or generation of photovoltage. The other is to regulate the recombination process of the photo-excited electron-hole pairs. A heterojunction of WSe$_2$ with the donor-type (K) overlayer enhances the surface potential but the amount of SPV is kept at that of the pristine WSe$_2$ surface. This may be related to the fact that part of the space charge layer near the surface has the electron occupation in the conduction band. Therefore, the electrostatic potential becomes constant and the drift force cannot be expected in this region for the photo-exited carriers. Concerning the relaxation time, τ_∞ was suppressed after the K deposition. When a WSe$_2$ surface makes a contact with the acceptor-type (C$_{60}$) over-layer, it reduces the surface potential and suppresses SPV, as shown in Figs 6.4 and 6.3. Furthermore, the relaxation time becomes also short, compared to the pristine WSe$_2$ surface.

In order to describe the different relaxation times by the surface modification, we recall the surface recombination model that approximates the SPV relaxation time as [96, 97]:

$$\tau_\infty = \tau_s \sim \frac{W}{S}. \tag{6.2}$$

where τ_s, W, and S are surface recombination time, width, and surface recombination velocity, respectively. The SCL widths at the present surfaces of WSe$_2$, K/WSe$_2$, and C$_{60}$/WSe$_2$, are evaluated to be about 120 nm from amount of the band-bending. Thus, the W values cannot be an origin of the significant change of relaxation time. On the other hand, when one considers that trapped states at a surface have the 2D density $N_{\rm t}$, S can then be written as [98][99]:

$$S = N_{\rm t} v_{\rm th} \sigma_{\rm p} e^{-eV_{\rm s}/\eta k_B T}, \tag{6.3}$$

where v_{th}, σ_{p}, and V_{s} are the thermal carrier velocity in a WSe$_2$ crystal, the carrier capture cross-section, and the surface potential. The equation contains parameters, N_{t}, σ_{p}, and V_{s} that vary with the present surface modifications, while the v_{th} value should be independent of the surface modification. According to Eqs. (6.2) and (6.3), the relaxation time becomes short with decrease of V_{s}. This behavior cannot explain the temporal change after the K deposition that showed the opposite behavior. It is inferred that QWS at the K/WSe$_2$ surface, as observed in Fig. 6.3 (e), may become the recombination center that increases N_{t} and/or σ_{p}. In the K/WSe$_2$ case, one may conclude that the increase of charges (states) at a surface enhances the band-bending effect but it may reinforce the recombination rate. Thus, such a system is suited for fast optical response such as photo-detectors. Concerning the case of C$_{60}$/WSe$_2$, the system has shorter τ than that of the pristine WSe$_2$ surface. Judging from Eq. (6.5), it can be explained by the decrease of V_{s} (Fig. 6.2) and increase of N_{t} and/or σ_{p} (Fig. 6.3). The LUMO states, located within the bulk band gap of WSe$_2$, likely dominate recombination of the photo-excited electron-hole pairs.

TABLE 6.1: SPV shift at t_0, ideality factor (η), efficiency of the optical excitation (γ), surface potential barrier heights (V_{s}), SPV relaxation times (τ_∞), widths of the space charge layer (W), density of surface trapped states (N_{t}).

	$V_{\text{SPV}}(0)$ (meV)	η	γ (cm^2/mJ)	τ_∞ (ns)	V_{s} (eV)	W (nm)	N_{t} (cm^{-2})
WSe$_2$	60±5	1.7±0.9	53±22	16±6	1.20	120	7.8×10^{13}
K/WSe$_2$	147±57	1.81±0.43	31.0±20.5	1.15±0.31	1.04	128	4.0×10^{12}
C$_{60}$/WSe$_2$	55±6	2.0±4.3	1.71±5.71	5.5±1.5	0.97	114	

6.5 Conclusion

Photoemission band mapping and time-resolved photoemission experiment were systematically performed on surfaces of the p-type WSe$_2$ crystal with two-types of adsorbates. On the K/WSe$_2$ surface, the potassium layer acts as a donor and it enhances the band-bending effect, while the fullerene layer at C$_{60}$/WSe$_2$ behaves as an acceptor and it reduces the effect. The surface photovoltage effect was observed for the WSe$_2$, K/WSe$_2$ and C$_{60}$/WSe$_2$ surfaces. The observed photovoltage had a tendency to be large for the large band-bending effect. The SPV relaxation time becomes short after the formation of the overlayers, indicating that the electronic states likely become the recombination centers of photo-excited carriers. These behaviors provide insights in designing TMDC-based optoelectronic devices in the future.

Chapter 7

Summary and future prospects

7.1 Conclusions

In preceding chapters, we attempted to understand the electronic structure and carrier dynamics of bulk WSe_2, modified WSe_2 surfaces, and ML WSe_2 by both conventional photoemission spectroscopy and state-of-the-art pump-probe time-resolved photoemission spectroscopy. From the material side, we expanded the scope of this thesis from bulk WSe_2 (Chapter 4), modified WSe_2 surfaces (Chapter 6) to ML WSe_2 (Chapter 5).

In Chapter 4, we observed Floquet-Bloch states at WSe_2 surface by below band gap pumping. These states are the replica of VBs with the energy shift of $\hbar\omega$, the photon energy of pump laser. The signal from LAPE may also contribute some signal to the ARPES spectra. By checking the polarization dependence of the replica bands, we concluded there are some contributions certainly due to the Floquet-Bloch state. At $\Delta t = 0$ to 2 ps, the intensity, width, and energy shift of VBs varies as functions of time. By a line-up process and Gaussian convolution fitting, the change in intensity, width and energy shift show a sudden change and last within 2 ps. By a detailed scan in time scale, the intensity of VBs oscillate and decay within 2 ps. Transforming the temporal trace of the intensity into frequency domain by fast Fourier transform (FFT), a single peak locates 6.7 THz are obtained. The frequency is very close to the double frequency of the acoustic phonon at zone boundary, which implies the two phonon excitation is occurred by the optical excitation. Not only two phonon excitation, but the single phonon excitation of A_{1g} mode is another possible interpretation.

In Chapter 5, the carrier dynamics of WSe_2 and ML WSe_2/BLG/SiC were studied by TRARPES with above band gap pumping. In the first part, we confirmed the circular dichroism at different K valleys of bulk WSe_2 by using circular polarized pump. This result can be attributed to the hidden spin-orbit coupling in each layer of bulk WSe_2 crystal and the surface sensitivity of ARPES technology. The ultrafast response can be explained by the intervalley scattering from K to T point, where T is the global CBM in bulk crystal. In the valence band, a depletion of the bands lasts more than 1 ps and beyond our measured range. The carrier lifetime in ps range, which has been reported elsewhere, is considered to be related to the scattering with defect states. In the second part, TRARPES measurement on ML WSe_2/BLG/SiC was carried out by above band gap pumping. The excited electrons is observed at K valleys. The sublayer, bilayer graphene, has also been spontaneously excited. The temporal traces at conduction band minimum, valence bands of ML WSe_2, and Dirac cone of BLG, have been analyzed by a Gaussian-convoluted multi-exponential function, respectively. In the investigation of the conduction band, a fast decay shows within 100 fs and a residue population last longer than 3 ps, which is beyond the measured range. The decay of the hole distribution in valence band shows the similar decay process. The short and long lifetimes are related to electron-electron interaction and the defect or surface state assisted scattering process, respectively. In the investigation of the Dirac cone in BLG, the temporal evolution is similar to those previous works. This result implies there is only a little influence caused by the adlayer in a van der Waals heterojunction and each layer generally preserve their own nature. An energy shift about 30-40 meV toward Fermi level is observed in VBs of ML WSe_2 in very short delay times. This energy shift does not pass through the sublayer, thus the surface photovoltage effect is ruled out. This shift is explained by gap renormalization that has been proposed in other recent studies.

In chapter 6, the SPV relaxation of three different surfaces were measured by TRXPS. By using ARPES and XPS, we observed the doping of K can produce the deepest band bending at the surface while the deposition of C_{60} may slightly flatten the surface band bending. At VB region, CBM at $\overline{T}$ was moved into occupied region by K deposition. K film forms a QWS while C_{60} forms a LUMO level in the band gap of WSe_2. The above electronic states are likely the new surface recombination centers such that the SPV relaxation time decrease an order than the pristine surface.

7.2   Future Prospect

(1) To distinguish the Floquet-Bloch state from LAPE state, the further experiment with higher repetition rate and tuneable pump wavelength will be helpful.

(2) To search for the Floquet-Bloch state that supposed by TROAS experiment, TRARPES below band gap pumping with circular polarized light is desired.

(3) To get better film quality, *in situ* growth of ML TMDCs may be necessary.

(4) To enhance the photovoltaic properties of WSe_2, the search for better organic molecules which can passivate the surface of WSe_2 is looking forward.

Appendix A

Coverage Estimation of C$_{60}$ and K at WSe$_2$ surface

In this section, the coverage estimation of C$_{60}$ overlayer and K overlayer will be demonstrated. The overlayer thickness is estimated by the intensity change in XPS spectra and inelastic mean free path (IMFP) equation described in Chapter 3. Figure A.1 shows the atomic structure and the side view of of WSe$_2$(001) surface. Along the (001) surface normal (see Fig. A.1(b), each sandwich layer is marked by numbers. The vertical spacing between each sandwich layers is d_W, and the spacing of W atoms and Se atoms within a sandwich layer is d. The PES intensity of W $4f$, I_{W4f} can be described by

$$
\begin{aligned}
I_{W4f} &= \sum_{i=0}^{\infty} I_i = I_0 + I_1 + I_2 + ... \\
&= kn_W\sigma_{W4f}(e^{-(\frac{d}{\lambda\cos\theta_d})} + e^{-(\frac{d+d_W}{\lambda\cos\theta_d})} + e^{-(\frac{d+2d_W}{\lambda\cos\theta_d})} + ...) \\
&= \frac{kn_W\sigma_{W4f}e^{-(\frac{d}{\lambda\cos\theta_d})}}{1 - e^{-(\frac{d_W}{\lambda\cos\theta_d})}},
\end{aligned}
$$

where I_i is the PES intensity contributed from the ith layer. k is a constant which is related to the photon flux, instrument transfer function, ...etc. n_W is the surface density of W atoms along (001) direction. σ_W is the cross section for W $4f$ by using a specific photon energy. The cross-section of W $4f$, Se $3d$, K $3p$, and C $1s$ as functions of excitation energy are drawn in Figs A.2(a) and A.2(b), respectively. λ is the IMFP of electron, which is dependent on its kinetic energy. The IMFP of electrons in WSe$_2$ can be estimated by Eqs. (3.15a) - (3.15f) in Chapter 3. The estimated IMFP in WSe$_2$,
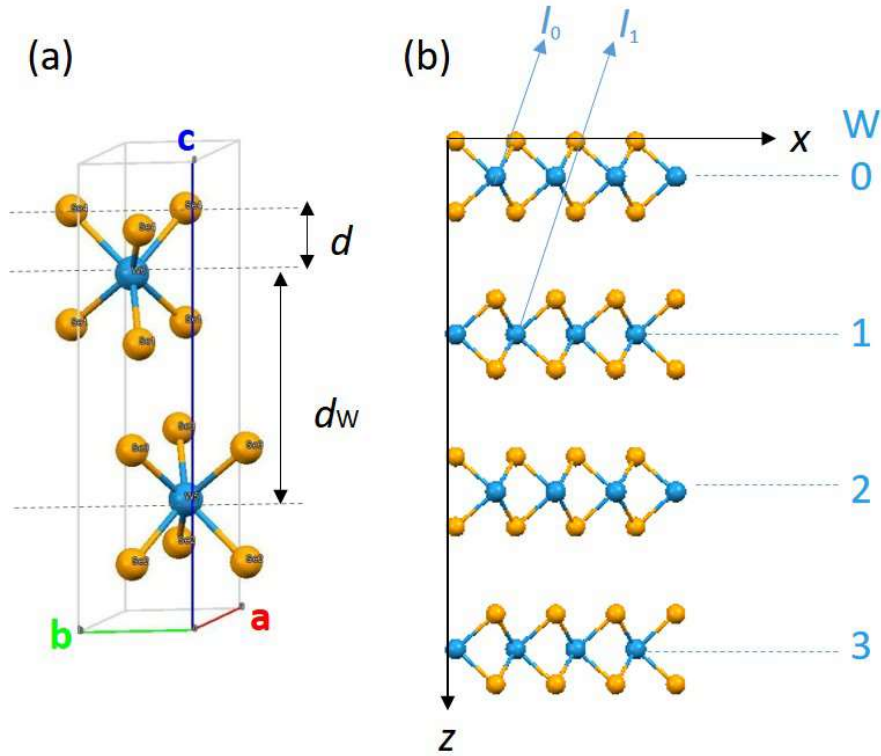
FIGURE A.1: (a) Crystal structure of WSe$_2$. a, b, and c are primitive lattice vectors, d and d$_W$ are the vertical distance between W and Se atom and the vertical spacing between W atoms (b) side view of sandwich layers. Blue rays marked by I_0 and I_1 represent the XPS intensity contributed from the 0th layer and first layer of W atoms.

C$_{60}$, and K as functions of kinetic energy are plotted in figure A.2(c). $\cos\theta_d$ is a scaling factor and θ_d is the emission angle. This scaling factor is around 1 for normal emission data, where θ_d is around 0.

After the K(C$_{60}$) deposition, the PES intensity of W $4f$ becomes

$$I'_{W4f} = \left(\sum_{i=0}^{\infty} I'_i\right)$$
$$= \sum_{i=0}^{\infty} I_i \times e^{\left(\frac{d_K}{\lambda_K\cos\theta_d}\right)}$$
$$= I_{W4f} \times e^{\left(\frac{d_K}{\lambda_K\cos\theta_d}\right)},$$

where λ_K is the IMFP in K, the adsorbate layer. d_K is the thickness of adsorbate layer. For Potassium layer, it is difficult to give a precise value of the thickness, thus
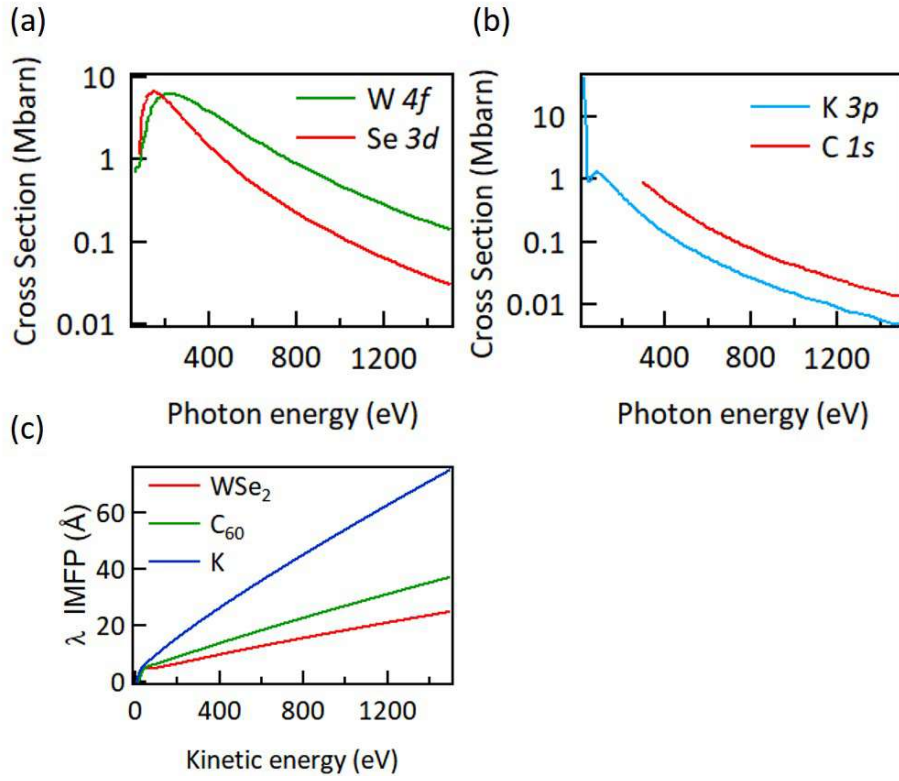
FIGURE A.2: Cross-section of (a) W $4f$, Se $3d$, and (b) K $3p$, C $1s$, as functions of excitation energy. (c) IMFP in WSe$_2$, C$_{60}$, and K as functions of kinetic energy [A1][A2].

we estimated the thickness of 1 atomic layer is roughly equal to the atomic diameter of K, which is 4.61 Åevaluated by its body-centered-cubic crystal structure. For C$_{60}$ layer, the thickness can be approximated as the diameter of fullerene [100], which is about 8 Å.

Table A.1 list all the necessary parameters for the coverage estimation. For 1 ML K/WSe$_2$, the intensity of W $4f$ taken by 253-eV photon energy will attenuate by $\exp(-d_K/\lambda_K)$, which is about 0.75. For 1 ML C$_{60}$, the intensity of W $4f$ taken by 385-eV photon energy will be reduced by a factor of $\exp(d_{C_{60}}/\lambda_{C_{60}})$, 0.52. Figure A.3 shows the W $4f$ XPS spectra of different surfaces. The W $4f$ XPS spectra are fitted by Shirley background and two Voigt functions. In Fig. A.3(a), the fitted peak area of W $4f_{7/2}$ and W $4f_{5/2}$ are decreased by a factor of 0.84±0.07 and 0.95±0.05 from the clean surface. Thus the average coverage of K can be estimated as 0.90±0.1 ML. In figure A.3(b), the fitted peak area of W $4f_{7/2}$ and W $4f_{5/2}$ are decreased by a factor of 0.75±0.04 and 0.61±0.01 from the clean surface, which indicate the coverage of C$_{60}$ is about 0.76±0.1 ML.
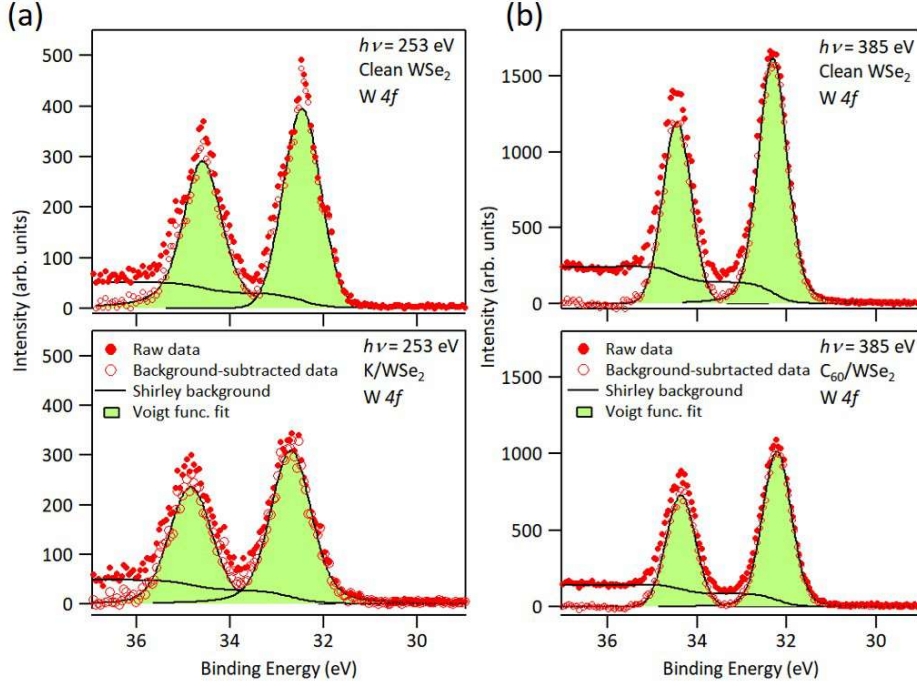
FIGURE A.3: W 4f XPS spectra of (a) Clean WSe$_2$ and K/WSe$_2$. (b) Clean WSe$_2$ and C$_{60}$/WSe$_2$. Red solid circles are raw data. Red opened circles are the background-subtracted data. Black solid lines are Shirley backgrounds. Black solid lines with green shadow are the Voigt function fitting curves.

TABLE A.1: Parameters for coverage estimation. n_W is the surface density of W atoms at (001) orientation. d_W is the spacing of W atoms in each layer. d is the interlayer spacing between W and Se atom along vertical direction. $d_{C_{60}}$ and d_K are the estimated thickness of 1 ML $d_{C_{60}}$ and d_K. $\lambda_{C_{60}}$, λ_K, λ_{WSe_2} are IMFPs of the photoemitted W 4f electrons in three different materials. Here the IMFPs are taken at $E_{kin} = 213$ eV and 349 eV to match the energy positions of W 4f by using respectively 253-eV and 385-eV photon energies.

n_W	3×10^{14} cm^{-2}	$\lambda_{C_{60}}$	12.37 Å(at $E_{kin} = 349$ eV)
d_W	6.94 Å	λ_{WSe_2}	8.78 Å(at $E_{kin} = 349$ eV)
d	1.66 Å	λ_K	16.35 Å(at $E_{kin} = 213$ eV)
$d_{C_{60}}$	8 Å	λ_{WSe_2}	6.66 Å(at $E_{kin} = 213$ eV)
d_K	4.61 Å		

References

1. Yeh, J.J., *Atomic Calculation of Photoionization Cross-Sections and Asymmetry Parameters*, Gordon and Breach Science Publishers, Langhorne, PE (USA), 1993.

2. Yeh, J.J. and Lindau, I., *Atomic Data and Nuclear Data Tables*, **32**, 1-155 (1985).

Publications

Publications included in this thesis

1. **Femtosecond to picosecond transient effects in WSe$_2$ observed by pump-probe angle-resolved photoemission spectroscopy**
   R. -Y. Liu, Yu Ogawa, Peng Chen, Kenichi Ozawa, Takeshi Suzuki, Masaru Okada, Takashi Someya, Yukiaki Ishida, Kozo Okazaki, Shik Shin, Tai-Chang Chiang, and Iwao Matsuda
   submitted to Scientific Reports.

2. **Controlling the Surface Photovoltage Relaxation Time by Modifying the Surface Property of WSe$_2$**
   R. -Y. Liu, Kenichi Ozawa, Naoya Terashima, Yuto Natsui, Baojie Feng, Suguru Ito, Wei-Chuan Cheng, Cheng-Maw Cheng, Susumu Yamamoto, Hiroo Kato, Tai-Chang Chiang, Iwao Matsuda
   to be submitted.

3. **Ultrafast carrier dynamics in monolayer WSe$_2$**
   R. -Y. Liu, Meng-Kai Lin, Peng Chen, Takeshi Suzuki, Philippa Clark, Nathan Lewis, Alfred Jones, Adam Wyatt, Richard Chapman, Cephise Cacho, Kozo Okazaki, Wendy Flavell, Shik Shin, Emma Springate, Tai-Chang Chiang, and Iwao Matsuda
   to be submitted.

Bibliography

1. Bromley, R. A., Murray, R. B. & Yoffe, A. D. *J. Phys. C: Solid State* **5,** 759–778 (1972).

2. Frindt, R. F. *J. Phys. Chem. Solids* **24,** 1107–1112 (1963).

3. Schlaf, R, Klein, A, Pettenkofer, C & Jaegermann, W. *Phys. Rev. B* **48,** 14242 (1993).

4. Klein, A, Pettenkofer, C, Jaegermann, W, Lux-Steiner, M & Bucher, E. *Surf. Sci.* **321,** 19–31 (1994).

5. Kipp, L, Adelung, R, Trares-Wrobel, N, Skibowski, M & Adelung, R. *Appl. Phys. Lett.* **74,** 1836 (1999).

6. Buck, J., Iwicki, J., Rossnagel, K. & Kipp, L. *Phys. Rev. B* **83,** 075312 (2011).

7. Geim, A. K. & Grigorieva, I. V. *Nature* **499,** 419 –425 (2017).

8. Li, Z. & Wong, S. L. *Mater. Sci. Eng.: C* **70,** 1095 –1106 (2017).

9. Xiao, D., Yao, W. & Niu, Q. *Phys. Rev. Lett.* **99,** 236809 (2007).

10. Yao, W., Xiao, D. & Niu, Q. *Phys. Rev. B* **77,** 235406 (2008).

11. Riley, J. M., Mazzola, F, Dendzik, M, Michiardi, M, Takayama, T, Bawden, L, Granerod, C, Leandersson, M, Balasubramanian, T, Hoesch, M, Kim, T. K., Takagi, H, Meevasana, W, Hofmann, P., Bahramy, M. S., Wells, J. W. & King, P. D. C. *Nat. Phys.* **10,** 835–839 (2014).

12. Bertoni, R, Nicholson, C. W., Waldecker, L, Hübener, H, Monney, C, De Giovannini, U, Puppin, M, Hoesch, M, Springate, E, Chapman, R. T., Cacho, C, Wolf, M, Rubio, A & Ernstorfer, R. *Phys. Rev. Lett.* **117,** 277201 (2016).

13. Grubišić Čabo, A., Miwa, J. A., Grønborg, S. S., Riley, J. M., Johannsen, J. C., Cacho, C., Alexander, O., Chapman, R. T., Springate, E., Grioni, M., Lauritsen, J. V., King, P. D. C., Hofmann, P. & Ulstrup, S. *Nano Lett.* **15,** 5883–5887 (2015).

14. Ulstrup, S., Čabo, A. G., Miwa, J. A., Riley, J. M., Grønborg, S. S., Johannsen, J. C., Cacho, C., Alexander, O., Chapman, R. T., Springate, E., Bianchi, M., Dendzik, M., Lauritsen, J. V., King, P. D. C. & Hofmann, P. *ACS Nano* **10,** 6315–6322 (2016).

15. Sie, E. J., McIver, J. W., Lee, Y.-H., Fu, L., Kong, J. & Gedik, N. *Nat. Mater.* **14,** 290 (2014).

16. Claassen, M., Jia, C., Moritz, B. & Devereaux, T. P. *Nat. Commun.* **7,** 13074 (2016).

17. Schäfer, H. *Chemical Transport Reactions* (Academic Press, New York, 1963).

18. Upadhyayula, L. C., Loferski, J. J., Wold, A, Giriat, W & Kershaw, R. *J. Appl. Phys.* **39,** 4736 (1968).

19. Dresselhaus, G. *Phys. Rev.* **100,** 580–586 (1955).

20. Zhang, X., Liu, Q., Luo, J.-W., Freeman, A. J. & Zunger, A. *Nat. Phys.* **10,** 387–393 (2014).

21. Hu, S. Y., Cheng, M. C., Tiong, K. K. & Huang, Y. S. *J. Phys. Condens. Matter* **17,** 3575–3583 (2005).

22. Finteis, T., Hengsberger, M., Straub, T., Fauth, K., Claessen, R., Auer, P., Steiner, P., Hüfner, S., Blaha, P., Vögt, M., Lux-Steiner, M. & Bucher, E. *Phys. Rev. B* **55,** 10400–10411 (1997).

23. Davey, B. & Evans, B. L. *Phys. Status Solidi A* **13,** 483–491 (1972).

24. Liu, G. B., Shan, W. Y., Yao, Y., Yao, W. & Xiao, D. *Phys. Rev. B* **88,** 085433 (2013).

25. Fang, S., Kuate Defo, R., Shirodkar, S. N., Lieu, S., Tritsaris, G. A. & Kaxiras, E. *Phys. Rev. B* **92,** 205108 (2015).

26. Xiao, D., Liu, G.-B., Feng, W., Xu, X. & Yao, W. *Phys. Rev. Lett.* **108,** 196802 (2012).

27. Zhu, Z. Y., Cheng, Y. C. & Schwingenschlögl, U. *Phys. Rev. B* **84,** 153402 (2011).

28. Shirley, J. H. *Phys. Rev.* **138,** B979–B987 (1965).

29. Floquet, G. fre. *Annales scientifiques de l'cole Normale Suprieure* **12,** 47–88 (1883).

30. Weingartshofer, A., Holmes, J. K., Caudle, G., Clarke, E. M. & Krüger, H. *Phys. Rev. Lett.* **39,** 269–270 (1977).

31. Wang, Y. H., Steinberg, H., Jarillo-Herrero, P. & Gedik, N. *Science* **342,** 453–457 (2013).

32. Fregoso, B. M., Wang, Y. H., Gedik, N. & Galitski, V. *Phys. Rev. B* **88,** 155129 (2013).

33. Saathoff, G., Miaja-Avila, L., Aeschlimann, M., Murnane, M. M. & Kapteyn, H. C. *Phys. Rev. A* **77,** 022903 (2008).

34. Mönch, W. *Semiconductor Surfaces and Interfaces* 3rd ed. doi:`10.1007/978-3-662-04459-9` (Springer-Verlag Berlin Heidelberg New York, Heidelberg, 2001).

35. Garrett, C. & Brattain, W. H. *Phys. Rev.* **99,** 376 (1955).

36. Johnson, E. O. *Phys. Rev.* **111,** 153 (1957).

37. Frankl, D. R. & Ulmer, E. A. *Surf. Sci.* **6,** 115–123 (1966).

38. Ogawa, M., Yamamoto, S., Yukawa, R., Hobara, R., Lin, C.-H., Liu, R.-Y., Tang, S.-J. & Matsuda, I. *Phys. Rev. B* **87,** 235308 (2013).

39. Ogawa, M., Yamamoto, S., Fujikawa, K., Hobara, R., Yukawa, R., Yamamoto, S., Kitagawa, S., Pierucci, D., Silly, M. G., Lin, C.-H., Liu, R.-Y., Daimon, H., Sirotti, F., Tang, S.-J. & Matsuda, I. *Phys. Rev. B* **88,** 165313 (2013).

40. Hecht, M. H. *Phys. Rev. B* **41,** 7918 (1990).

41. Hamers, R. J. & Cahill, D. G. *J. Vac. Sci. Technol. B* **9,** 514 (1991).

42. Bröcker, D., Gießel, T. & Widdra, W. *Chem. Phys.* **299,** 247 (2004).

43. Jaegermann, W., Pettenkofer, C. & Parkinson, B. A. *Phys. Rev. B* **42,** 7487–7496 (1990).

44. Schellenberger, A., Schlaf, R., Pettenkofer, C. & Jaegermann, W. *Phys. Rev. B* **45,** 3538–3545 (1992).

45. Franceschetti, A. *MRS Bull.* **36,** 192197 (2011).

46. Gan, L. Y., Zhang, Q., Cheng, Y. & Schwingenschlögl, U. *J. Phys. Chem. Lett.* **5,** 1445–1449 (2014).

47. Ozawa, K., Yamamoto, S., Yukawa, R., Akikubo, K., Emori, M., Sakama, H. & Matsuda, I. *Organic Electronics* **31,** 98 –103 (2016).

48. Damascelli, A., Hussain, Z. & Shen, Z.-X. *Rev. Mod. Phys.* **75,** 473–541 (2003).

49. Seah, M. P. & A., D. W. *Surf. Interface Anal.* **1,** 2–11 (1979).

50. Tanuma, S., Powell, C. J. & Penn, D. R. *Surf. Interface Anal.* **35,** 268–275 (2003).

51. Bauer, M. *J. Phys. D: Appl. Phys.* **38,** R253–R267 (2005).

52.   Ishizaka, K., Kiss, T., Shimojima, T., Yokoya, T., Togashi, T., Watanabe, S., Zhang, C. Q., Chen, C. T., Onose, Y., Tokura, Y. & Shin, S. *Phys. Rev. B* **72,** 233202 (2005).

53.   Mathias, S, Miaja-Avila, L, Murnane, M. M., Kapteyn, H, Aeschlimann, M & Bauer, M. *Rev. Sci. Instrum.* **78,** 083105 (2007).

54.   Yamamoto, T. PhD thesis (Tokyo University of Science, 2016).

55.   Frassetto, F., Cacho, C., A. Froud, C., Turcu, I. E., Villoresi, P., Bryan, W. A., Springate, E. & Poletto, L. *Opt. Express* **19,** 19169 (2011).

56.   Turcu, I. C. E., Springate, E., Froud, C. A., Cacho, C. M., Collier, J. L., Bryan, W. A., Nemeth, G. R.A. J., Marangos, J. P., Tisch, J. W. G., Torres, R., Siegel, T., Brugnera, L., Underwood, J. G., Procino, I., Newell, W. R., Altucci, C., Velotta, R., King, R. B., Alexander, J. D., Calvert, C. R., Kelly, O., Greenwood, J. B., Williams, I. D., Cavalleri, A., Petersen, J. C., Dean, N., Dhesi, S. S., Poletto, L., Villoresi, P., Frassetto, F., Bonora, S. & Roper, M. D. *Proc. SPIE* **7469,** 746902 (2010).

57.   Ogawa, M., Yamamoto, S., Kousa, Y., Nakamura, F., Yukawa, R., Fukushima, A., Harasawa, A., Kondoh, H., Tanaka, Y., Kakizaki, A. & Matsuda, I. *Rev. Sci. Instrum.* **83,** 023109 (2012).

58.   Ovsyannikov, R., Karlsson, P., Lundqvist, M., Lupulescu, C., Eberhardt, W., Fhlisch, A., Svensson, S. & Mrtensson, N. *J. Electron Spectrosc. Relat. Phenom.* **191,** 92 −103 (2013).

59.   Yamamoto, S., Senba, Y., Tanaka, T., Ohashi, H., Hirono, T., Kimura, H., Fujisawa, M., Miyawaki, J., Harasawa, A., Seike, T., Takahashi, S., Nariyama, N., Matsushita, T., Takeuchi, M., Ohata, T., Furukawa, Y., Takeshita, K., Goto, S., Harada, Y., Shin, S., Kitamura, H., Kakizaki, A., Oshima, M. & Matsuda, I. *J. Synchrotron Radiat.* **21,** 352–365 (2014).

60.   Sentef, M., Claassen, M., Kemper, A., Moritz, B., Oka, T., Freericks, J. & Devereaux, T. *Nat. Commun.* **6,** 7047 (2015).

61.   Zhou, Y & Wu, M. W. *Phys. Rev. B* **83,** 245436 (2011).

62.   Lindner, N. H., Refael, G. & Galitski, V. *Nat. Phys.* **7,** 490–495 (2011).

63.   Liu, G.-B., Xiao, D., Yao, Y., Xu, X. & Yao, W. *Chem. Soc. Rev.* **44,** 2643–2663 (2015).

64.   Mahmood, F., Chan, C.-K., Alpichshev, Z., Gardner, D., Lee, Y., Lee, P. A. & Gedik, N. *Nat. Phys.* **12,** 306–311 (2015).

65. Yousefi, G. *Mater. Lett.* **9,** 38–40 (1989).

66. Hein, P., Stange, A., Hanff, K., Yang, L. X., Rohde, G., Rossnagel, K. & Bauer, M. *Phys. Rev. B* **94,** 205406 (2016).

67. Saathoff, G., Miaja-Avila, L., Aeschlimann, M., Murnane, M. M. & Kapteyn, H. C. *Phys. Rev. A* **77,** 022903 (2008).

68. Madsen, L. B. *Am. J. Phys.* **73,** 57 (2005).

69. Park, S. T. *Phys. Rev. A* **90,** 013420 (2014).

70. Ishizaka, K., Kiss, T., Yamamoto, T., Ishida, Y., Saitoh, T., Matsunami, M., Eguchi, R., Ohtsuki, T., Kosuge, A., Kanai, T., Nohara, M., Takagi, H., Watanabe, S. & Shin, S. *Phys. Rev. B* **83,** 081104 (2011).

71. Johnson, S. L., Beaud, P, Vorobeva, E, Milne, C. J., Murray, É. D., Fahy, S & Ingold, G. *Phys. Rev. Lett.* **102,** 175503 (2009).

72. Jeong, T. Y., Jin, B. M., Rhim, S. H., Debbichi, L., Park, J., Jang, Y. D., Lee, H. R., Chae, D. H., Lee, D., Kim, Y. H., Jung, S. & Yee, K. J. *ACS Nano* **10,** 5560–5566 (2016).

73. Trigo, M., Sheu, Y. M., Arms, D. A., Chen, J., Ghimire, S., Goldman, R. S., Landahl, E., Merlin, R., Peterson, E., Reason, M. & Reis, D. A. *Phys. Rev. Lett.* **101,** 025505 (2008).

74. Nam, D., Lee, J.-U. & Cheong, H. *Sci. Rep.* **5,** 17113 (2015).

75. Huang, W., Luo, X., Gan, C. K., Quek, S. Y. & Liang, G. *Phys. Chem. Chem. Phys.* **16,** 10866–10874 (2014).

76. De Giovannini, U., Hu, H. & Rubio, A. *Nano Lett.* **16,** 7993–7998 (2016).

77. Alidoust, N., Bian, G., Xu, S.-Y., Sankar, R., Neupane, M., Liu, C., Belopolski, I., Qu, D.-X., Denlinger, J. D., Chou, F.-C. & Hasan, M. Z. *Nat. Commun.* **5,** 4673 (2014).

78. Mak, K. F., He, K., Shan, J. & Heinz, T. F. *Nat. Nanotech.* **7,** 494–498 (2012).

79. Yan, T., Qiao, X., Liu, X., Tan, P. & Zhang, X. *Appl. Phys. Lett.* **105,** 101901 (2014).

80. Wang, Q., Zhang, W., Wang, L., He, K., Ma, X. & Xue, Q. *J. Phys. Condens. Mat.* **25,** 095002 (2013).

81. Someya, T., Fukidome, H., Watanabe, H., Yamamoto, T., Okada, M., Suzuki, H., Ogawa, Y., Iimori, T., Ishii, N., Kanai, T., Tashima, K., Feng, B., Yamamoto, S., Itatani, J., Komori, F., Okazaki, K., Shin, S. & Matsuda, I. *Phys. Rev. B* **95,** 165303 (2017).

82. Zhang, Y., Ugeda, M. M., Jin, C., Shi, S.-F., Bradley, A. J., Martín-Recio, A., Ryu, H., Kim, J., Tang, S., Kim, Y., Zhou, B., Hwang, C., Chen, Y., Wang, F., Crommie, M. F., Hussain, Z., Shen, Z.-X. & Mo, S.-K. *Nano Lett.* **16,** 2485–2491 (2016).

83. Ulstrup, S., Johannsen, J. C., Cilento, F., Miwa, J. A., Crepaldi, A., Zacchigna, M., Cacho, C., Chapman, R., Springate, E., Mammadov, S., Fromm, F., Raidel, C., Seyller, T., Parmigiani, F., Grioni, M., King, P. D. C. & Hofmann, P. *Phys. Rev. Lett.* **112,** 257401 (2014).

84. Gierz, I., Petersen, J. C., Mitrano, M., Cacho, C., Turcu, I. C. E., Springate, E., Stöhr, A., Köhler, A., Starke, U. & Cavalleri, A. *Nat. Mater.* **12,** 1119–1124 (2013).

85. Johannsen, J. C., Ulstrup, S., Cilento, F., Crepaldi, A., Zacchigna, M., Cacho, C., Turcu, I. C. E., Springate, E., Fromm, F., Raidel, C., Seyller, T., Parmigiani, F., Grioni, M. & Hofmann, P. *Phys. Rev. Lett.* **111,** 027403 (2013).

86. Johannsen, J. C., Ulstrup, S., Crepaldi, A., Cilento, F., Zacchigna, M., Miwa, J. A., Cacho, C., Chapman, R. T., Springate, E., Fromm, F., Raidel, C., Seyller, T., King, P. D. C., Parmigiani, F., Grioni, M. & Hofmann, P. *Nano Lett.* **15,** 326–331 (2015).

87. Someya, T., Fukidome, H., Ishida, Y., Yoshida, R., Iimori, T., Yukawa, R., Akikubo, K., Yamamoto, S., Yamamoto, S., Yamamoto, T., Kanai, T., Funakubo, K., Suemitsu, M., Itatani, J., Komori, F., Shin, S. & Matsuda, I. *Appl. Phys. Lett.* **104,** 161103 (2014).

88. Wang, H., Zhang, C. & Rana, F. *Nano Lett.* **15,** 339–345 (2015).

89. Ulstrup, S., Johannsen, J. C., Cilento, F., Crepaldi, A., Miwa, J. A., Zacchigna, M., Cacho, C., Chapman, R. T., Springate, E., Fromm, F., Raidel, C., Seyller, T., King, P. D., Parmigiani, F., Grioni, M. & Hofmann, P. *J. Electron Spec. Rel. Phenom.* **200,** 340–346 (2015).

90. Riley, J. M., Meevasana, W, Bawden, L, Asakawa, M, Takayama, T, Eknapakul, T, Kim, T. K., Hoesch, M, Mo, S.-K., Takagi, H, Sasagawa, T, Bahramy, M. S. & King, P. D. C. *Nat. Nanotech.* **10,** 1043–1047 (2015).

91. Osada, K., Tanaka, M., Ohno, S. & Suzuki, T. *Jpn. J. Appl. Phys.* **065201** (2016).

92. Jakubowicz, A, Mahalu, D, Wolf, M, Wold, A & Tenne, R. *Phys. Rev. B* **40,** 2992 (1989).

93. Wang, Y., Holden, J. M., Rao, A. M., Eklundt, P. C., Venkateswaran, U. D., Eastwood, D., Lidberg, R. L., Dresselhaus, G & Dresselhaus, M. S. *Phys. Rev. B* **51,** 4547–4556 (1995).

94. Sze, S. M. & Ng, K. K. *Physics of Semiconductor Devices* 3rd ed. (John Wiley Sons, Inc., Hoboken, New Jersey, 2007).

95. Kronik, L. & Shapira, Y. *Surf. Sci. Rep.* **37,** 1–206 (1999).

96. Sproul, A. B. *J. Appl. Phys.* **76,** 2851–2854 (1994).

97. Luke, K. L. & Cheng, L. *J. Appl. Phys.* **61,** 2282–2293 (1987).

98. Ozawa, K., Yamamoto, S., Yukawa, R., Liu, R., Emori, M., Inoue, K., Higuchi, T., Sakama, H., Mase, K. & Matsuda, I. *J. Phys. Chem. C* **120,** 29283–29289 (2016).

99. Shockley, W & Read Jr, W. T. *Phys. Rev.* **87,** 835 (1952).

100. Sanchez-Sanchez, C., Lanzilotto, V., Gonzalez, C., Verdini, A., deAndres, P. L., Floreano, L., Lopez, M. F. & Martin-Gago, J. A. *Chem. Eur. J.* **18,** 7382–7387 (2012).